

Numerical Simulation of Slider Air Bearings

by

Sha Lu

B.Sc. (Shanghai Jiao Tong University) 1989

B.Eng. (Shanghai Jiao Tong University) 1989

A dissertation submitted in partial satisfaction of the

requirements for the degree of

Doctor of Philosophy

in

Engineering-Mechanical Engineering

in the

GRADUATE DIVISION

of the

UNIVERSITY of CALIFORNIA at BERKELEY

Committee in charge:

Professor David B. Bogy, Chair

Professor Ömer Savas

Professor Ole H. Hald

1997

Numerical Simulation of Slider Air Bearings

© 1997

by

Sha Lu

ABSTRACT

Numerical Simulation of Slider Air Bearings

by

Sha Lu

Doctor of Philosophy in Engineering-Mechanical Engineering

University of California at Berkeley

Professor David B. Bogy, Chair

This dissertation focuses on the development of a general purpose slider air bearing simulation program to be used as a tool for designing air bearings in modern hard disk drives. The computer code, called the CML Air Bearing Design Program, implements a multi grid control volume method to solve the generalized Reynolds equation. It can simulate all the main air bearing surface features such as multiple etch depth, shaped rails, and arbitrary wall profile. A mass flow rate averaging method is incorporated to deal with clearance discontinuities.

It is found that aligning the grid lines with rail boundaries and the taper location can improve the accuracy and consistency of the solution. A adaptive grid method based on the pressure gradient field is also implemented which greatly facilitates grid generation. The implementation of a full approximation storage and full multi grid method dramatically improves the solver efficiency.

Under high speed, low spacing conditions, the numerical solution may become unstable if the central difference method is used for the convective term in the Reynolds equation. Several alternatives are compared and it is found that the hybrid scheme is superior to all other schemes for slider air bearing applications.

Several sub-25 nm, “negative pressure” slider designs are presented. The designs all have flat fly height profiles across the disk radius and low take-off speeds. It is found that the wall angle resulting from the etching process can alter the air bearing fly height significantly. It is important to include the wall angle effect in the simulation.

Prof. David B. Bogy, Chair

To my parents and Ming

TABLE OF CONTENTS

Abstract	1
Dedication	iii
Table of Contents	iv
List of Figures	vii
List of Tables	x
Acknowledgements	xi
Chapter 1 Introduction	1
Chapter 2 Numerical Method	5
2.1 Introduction	5
2.2 Generalized Reynolds Equation	6
2.2.1 Reynolds Equation	6
2.2.2 Rarefaction Models	7
2.3 Control Volume Formulation	9
2.3.1 Integration of the Generalized Reynolds Equation	9
2.3.2 Central Difference Scheme	10
2.3.3 Stable Convective Schemes	12
2.4 Mass Flow Averaging for Clearance Discontinuities	13
2.4.1 Formulation	13
2.4.2 Implementation	14
2.5 Mass Flow Patterns	15
2.5.1 Stream Function	15

2.5.2	Integration of the Stream Function	15
2.6	Pressure Solution for Given Slider Attitude	17
2.6.1	The Line Sweeping Method	17
2.6.2	Convergence Criterion	18
2.6.3	Multi Grid Method	19
2.7	Solution for Steady State Fly Height	19
2.7.1	Inverse Solution	19
2.7.2	Shear Force Effect	20
2.8	Summary	22
Chapter 3	Computational Grid	31
3.1	Introduction	31
3.2	Grid Generated by Geometric Progression	32
3.3	Grid Snapping	32
3.3.1	Grid Snapping at the Taper End	33
3.3.2	Grid Snapping on the Rail Boundary	33
3.4	Adaptive Grid	35
3.5	Summary	37
Chapter 4	A Multi Grid Solver for the Generalized Reynolds Equation	49
4.1	Introduction	49
4.2	Numerical Method	50
4.2.1	Full Approximation Storage (FAS) Scheme	50
4.2.2	Full Multi Grid Algorithm	53
4.3	Results and Discussions	54

4.4	Summary	54
Chapter 5	Comparison of Convection Schemes	60
5.1	Introduction	60
5.2	Numerical Method	60
5.3	Results and Discussions	62
	5.3.1 Results for the TPC Slider	62
	5.3.2 Results for the Nutcracker Slider	63
5.4	Summary	64
Chapter 6	Some Sub-25 NM Negative Pressure Slider Designs	71
6.1	Introduction	71
6.2	Numerical Models	72
6.3	Results and Discussions	72
	6.3.1 A 50% Slider Design for 25 nm Spacing	72
	6.3.2 Three Sub-25 nm Spacing Slider Designs	74
6.4	Summary	75
Chapter 7	Conclusion	90
References	92
Appendix A	CML Air Bearing Design Program	
	User's Manual (Matlab Version)	96
Appendix B	CML Air Bearing Design Program	
	User's Manual (Windows Version)	123

List of Figures

Chapter 2

- Fig. 2.1 Illustration of the control volume (after Patankar, 1980)
Fig. 2.2 Mass flow averaging scheme for clearance discontinuity
Fig. 2.3 Mass flow pattern on the staggered grid for the Nutcracker slider
Fig. 2.4 Rail shape of the Tripad slider
Fig. 2.5 Rail shape of the Nutcracker slider
Fig. 2.6 3-D pressure profile for the Tripad slider
Fig. 2.7 3-D pressure profile for the Nutcracker slider
Fig. 2.8 Fly height profile for the Tripad with (x) and without (o) shear effect
Fig. 2.9 Fly height profile for the Nutcracker slider with (x) and without (o) shear effect
Fig. 2.10 Pitch angle of the Tripad slider with (x) and without (o) shear effect
Fig. 2.11 Pitch angle of the Nutcracker slider with (x) and without (o) shear effect
Fig. 2.12 Roll of the Tripad slider with (x) and without (o) shear effect
Fig. 2.13 Roll of the Nutcracker slider with (x) and without (o) shear effect

Chapter 3

- Fig. 3.1 Rail shapes of the IBM Tri-rail slider
Fig. 3.2 3-D pressure profile of the Tri-rail slider. Radius = 20 mm, skew = 0°
Fig. 3.3 Sample grid distribution for the IBM Tri-rail slider
Fig. 3.4 Grid used for studying grid snapping effect at the taper end. Grid size: 65 x 65. The taper end varies between the two thick lines.
Fig. 3.5 Effect of grid snapping at the taper end. (o): with grid snapping; (x): without grid snapping
Fig. 3.6 Convergence of Tri-rail fly height with grid size. (o): with grid snapping; (x): without grid snapping
Fig. 3.7 Convergence of Tri-rail pitch with grid size. (o): with grid snapping; (x): without grid snapping
Fig. 3.8 Convergence of Tri-rail roll with grid size. (o): with grid snapping; (x): without grid snapping
Fig. 3.9 Rail shape of the TPC slider.
Fig. 3.10 3-D pressure profile of the TPC slider
Fig. 3.11 Convergence of TPC fly height with grid size. (o): with grid snapping; (x): without grid snapping
Fig. 3.12 Convergence of TPC pitch with grid size. (o): with grid snapping; (x): without grid snapping
Fig. 3.13 Convergence of TPC roll with grid size. (o): with grid snapping; (x): without grid snapping
Fig. 3.14 3-D pressure profile for the Tripad slider. Radius = 31 mm, skew = 17.4°, ipmax = 0, difmax = 40, decayfactor = 40
Fig. 3.15 3-D pressure profile for the Tripad slider. Radius = 31 mm, skew = 17.4°, ipmax = 1, difmax = 40, decayfactor = 40

- Fig. 3.16 Rail shape of the Seagate AAB slider
 Fig. 3.17 Grid distribution for the AAB slider. $I_{pmax} = 0$, no smoothing and gradient limit
 Fig. 3.18 Grid distribution for the AAB slider. $I_{pmax} = 0$, decayfactor = 60, no gradient limit
 Fig. 3.19 Grid distribution for the AAB slider. $I_{pmax} = 0$, decayfactor = 60, difmax = 30
 Fig. 3.20 3-D pressure profile of the AAB slider

Chapter 4

- Fig. 4.1 The full multi grid procedure (after Shyy and Sun, 1992)
 Fig. 4.2 Multi grid for the Tri-rail slider, grid level 2: 25 x 25
 Fig. 4.3 Multi grid for the Tri-rail slider, grid level 3: 49 x 49
 Fig. 4.4 Multi grid for the Tri-rail slider, grid level 4: 97 x 97
 Fig. 4.5 Multi grid for the Tri-rail slider, grid level 5: 193 x 193
 Fig. 4.6 3-D pressure profile for the Tri-rail slider, grid level 2: 25 x 25
 Fig. 4.7 3-D pressure profile for the Tri-rail slider, grid level 3: 49 x 49
 Fig. 4.8 3-D pressure profile for the Tri-rail slider, grid level 4: 97 x 97
 Fig. 4.9 3-D pressure profile for the Tri-rail slider, grid level 5: 193 x 193

Chapter 5

- Fig. 5.1 Rail shape of the TPC slider
 Fig. 5.2 Rail shape of the Nutcracker slider
 Fig. 5.3 3-D pressure profile of the TPC slider using central difference scheme on a 49 x 49 grid
 Fig. 5.4 Convergence of normalized peak pressure with grid size for TPC slider using different convective schemes. (o): central difference; (x): power-law; (*): QUICK; (+): hybrid; solid line: upwind
 Fig. 5.5 Convergence of bearing load with grid size for TPC slider using different convective schemes. (o): central difference; (x): power-law; (*): QUICK; (+): hybrid; solid line: upwind
 Fig. 5.6 3-D pressure profile of the Nutcracker slider using central difference scheme on a 97 x 97 grid
 Fig. 5.7 3-D pressure profile of the Nutcracker slider using the QUICK scheme on a 97 x 97 grid
 Fig. 5.8 Convergence of normalized peak pressure with grid size for the Nutcracker slider using different convective schemes. (o): central difference; (x): power-law; (*): QUICK; (+): hybrid; solid line: upwind
 Fig. 5.9 Convergence of bearing load with grid size for the Nutcracker slider using different convective schemes. (o): central difference; (x): power-law; (*): QUICK; (+): hybrid; solid line: upwind

Chapter 6

- Fig. 6.1 Rail outline of the 50%, 25 nm slider
- Fig. 6.2 3-D pressure profile for the 50%, 25 nm slider. Radius = 15, skew = -3.88°
- Fig. 6.3 Fly height profile of the 50%, 25 nm slider. Skew = -3.88° to 17.85°
- Fig. 6.4 Pitch profile of the 50%, 25 nm slider
- Fig. 6.5 Roll profile of the 50%, 25 nm slider
- Fig. 6.6 Take-off fly height profile of the 50%, 15 nm slider at ID
- Fig. 6.7 Fly height profile at measuring point. (x): original prediction; (o): measurement; (*): re-calculated
- Fig. 6.8 Slider roll (x): original prediction; (o): measurement; (*): recalculated
- Fig. 6.9 SEM image of the etch slope profile
- Fig. 6.10 Rail shape of the 50 %, 25 nm Nutcracker slider
- Fig. 6.11 3-D pressure profile of the Nutcracker slider. Radius = 15 mm, skew = -3.88°
- Fig. 6.12 Fly height profile of the Nutcracker slider. Skew = -3.88° to 17.85°
- Fig. 6.13 Pitch angle profile of the Nutcracker slider
- Fig. 6.14 Roll profile of the Nutcracker slider
- Fig. 6.15 Take off fly height profile of the Nutcracker slider at ID
- Fig. 6.16 Rail shape of the 50%, 15 nm slider
- Fig. 6.17 3-D pressure profile of the 50%, 15 nm slider. Radius = 15 mm, skew = -6.27°
- Fig. 6.18 Fly height profile of the 50%, 15 nm slider. Skew = -6.27° to 17°
- Fig. 6.19 Pitch profile of the 50%, 15 nm slider
- Fig. 6.20 Roll profile of the 50%, 15 nm slider
- Fig. 6.21 Take-off fly height profile of the 50%, 15 nm slider at ID
- Fig. 6.22 Rail outline of the 30%, 15 nm slider
- Fig. 6.23 3-D pressure profile for the 30%, 15 nm slider. Radius = 15 mm, skew = -1.22°
- Fig. 6.24 Fly height profile of the 30%, 15 nm slider. Skew = -1.22° to 17.39°
- Fig. 6.25 Pitch profile of the 30%, 15 nm slider
- Fig. 6.26 Roll profile of the 30%, 15 nm slider
- Fig. 6.27 Take-off fly height profile of the 30%, 15 nm slider at ID

List of Tables

Chapter 3

Table. 3.1 Example of piece-wise geometric progression grid specification

ACKNOWLEDGMENTS

I would like to extend my sincere gratitude to my advisor, Prof. David. B. Bogy for his continuous guidance and support throughout my graduate career at Berkeley. I would also like to thank Prof. Ömer Savas and Prof. Ole H. Hald for reviewing this manuscript.

I want to thank my fellow graduate students at the Computer Mechanics Laboratory, particularly Matthew O'Hara and Yong Hu, for making my graduate experience more enjoyable. I am also indebted to numerous people in the disk drive industry who gave me helpful suggestions and bug reports on the simulation program.

I am eternally grateful to my parents who taught me the value of education and hard work. My deepest appreciation belongs to my wife, Ming, for her love, comfort and patience. I particularly want to thank her for her tolerance of my frequent staying up all night during the course of writing this dissertation.

CHAPTER 1

INTRODUCTION

Today's highly graphical and rich multimedia computing environment demands more data storage capacity than ever before. Magnetic hard disk drives provide a reliable, inexpensive, high speed and high density storage media. In the early days of the industry a few decades ago, the hard disk drives were twice as big as a refrigerator, had a few megabytes of storage capacity and cost hundreds of thousands of dollars. Most modern drives are only slightly bigger than a pocket calculator, can hold up to a few gigabytes of data, and cost only about 12 cents per megabyte. The price / performance ratio is still dropping rapidly.

In magnetic hard disk drives, the read/write transducers are attached to sliders that are loaded onto the disk surface by a spring suspension. When the disks spin at high speed (currently from 5400 RPM to 10000 RPM), the air flow between the slider and the disk creates an air bearing which lifts the slider from the disk surface by a small distance, called the fly height. It is the fly height at the read/write transducer that has a direct impact on the recording density. Higher densities require lower fly heights.

The slider air bearing surface is designed with shapes that provide desired flying characteristics. The first IBM Winchester sliders had two simple straight rails acting as the air bearing surface. The rails had tapers at the leading edge to add stability and pressurize the air. Since then, the fly height of the sliders has decreased dramatically with the increase in recording density. Lower fly height requires better tribological

performance from the air bearing design. New recording technology also demands that the fly height be relatively constant across the entire disk radius. In the meantime, chemical etching and ion beam milling technologies have enabled the creation of arbitrarily shaped slider air bearings. Therefore, air bearings of significant complexity have appeared to meet the demanding design requirements. New features in air bearing designs include shaped rails, multiple etch depths and negative pressure pockets.

Numerical simulation has been an indispensable tool for air bearing design. An efficient numerical code enables us to evaluate many different designs without building and testing each one of them, thus shortening the cycle time and reducing the development cost. The primary goal of this dissertation is to develop an efficient, powerful air bearing design program that is capable of handling all the practical air bearing features. Using this code, we investigate some issues in air bearing design. Several low flying air bearing designs are also obtained and summarized in this dissertation.

The governing equation for the air bearing pressure between the slider and the disk is the generalized Reynolds equation. The next four chapters are devoted to the detailed account of the numerical techniques developed to solve this equation. In Chapter 2, the generalized Reynolds equation and an overview of numerical methods for solving this equation are presented. A control volume formulation is used to discretize the equation. It is very stable and well suited for air bearing problems for the high speed and low spacing in the current magnetic hard disk drives. A mass flow averaging technique is used to treat the clearance discontinuities in arbitrarily shaped, multiple recess level air bearings. A staggered grid is used to obtain the mass flow patterns accurately, which can

be helpful in tracking the contamination particles in the air bearing. The solution procedure for obtaining the steady state fly height is also discussed.

Grid generation is one of the most important issues in any numerical solution. Without an adequate grid, the numerical results obtained can be inaccurate, sometimes totally meaningless. Chapter 3 discusses the treatment of special grid issues in slider air bearing simulations. Results show that the grid should be aligned with the discontinuity boundary as much as possible to accelerate grid convergence - the asymptotic approach to the true solution as grid size increases. It is also demonstrated that it is very important to have enough grid resolution at the taper end. A heuristic method is implemented to achieve this automatically. Although the grid can be generated manually using piecewise geometric series, this method is inefficient and tedious to use. An adaptive grid method is implemented in order to make better use of the available grid size. This method does not change the total grid size, rather it redistributes the grid based on the pressure gradient so that the grid is more concentrated where the pressure changes rapidly.

Iterative solution of the discretized Reynolds equation on a single grid is not very efficient. The convergence rate slows down as the iteration progresses. The implementation of the multi grid method in Chapter 4 improves the solver efficiency dramatically and makes the air bearing simulator a powerful design tool. The stability and accuracy of the solution depends on the treatment of the convective term. Different convection-diffusion schemes are compared in Chapter 5.

In Chapter 6, several low flying air bearing designs are obtained using the air bearing simulator. After the first design was fabricated, it was found that the etched wall

actually had a very shallow slope. Good agreement was obtained after the simulation included the shallow wall. Different wall profiles are created when different processes are used.

The final chapter, Chapter 8, summarizes this study. Appendix A contains the User's Manual of the Matlab based graphical interface, and the Windows based graphical interface is described in Appendix B.

CHAPTER 2

NUMERICAL METHOD

2.1 Introduction

The governing equation of the traditional gas-lubricated slider bearing is the Reynolds equation. Analytical solution of the Reynolds equation is available for a few special cases. Numerical methods have to be applied for general configurations. Castelli and Pirvics (1963) provided a review of early methods.

During the past three decades, hard disk drives have undergone dramatic improvements. While the size of drives has decreased, the storage capacity has increased from a few megabytes to gigabytes. The higher data storage density is achieved partly through the reduction of slider fly height. The fly height has been lowered from a few microns to less than 50 nm in many drives today. Performance requirements led to the development of sophisticated air bearing designs. It has been shown that shaped rail negative (sub-ambient) pressure air bearings have very high air bearing stiffness and fast take-off characteristics, which improves head-disk interface reliability (Kogure, *et al.*, 1983; White, 1983; Yoneoka, *et al.*, 1987). Constant fly height profile across the entire radius of the disk can also be achieved with negative pressure slider designs. In addition, multiple etch depths are being used to further improve air bearing performance (Hardie, *et al.*, 1994; White, 1991). Simulation of these air bearings under high speed, low spacing conditions presents a considerable numerical challenge. The numerical method must be versatile, stable and efficient.

Research on the numerical solution of air bearing slider problems, including dynamic effects, has been ongoing in the Computer Mechanics Laboratory over the past decade. Garcia-Suarez *et al.* (1984) proposed a finite element method with an upwind scheme for air bearing simulations. Miu and Bogy (1986b) simulated taper-flat sliders using the factored implicit scheme of White and Nigam (1980). Ruiz and Bogy (1990a) implemented the second order slip correction and the Fukui and Kaneko (1988) model. A factored implicit scheme for irregular rail geometry has been developed by Cha and Bogy (1995). The method is based on a control volume formulation of the linearized Reynolds equation. It also implemented the power-law scheme in mass flow calculations to enhance the stability of the algorithm. The steady state solution is achieved using an alternating direction implicit method with time stepping.

In this chapter, a control volume formulation (Patankar, 1980) is adapted to analyze shaped-rail air bearing at ultra low spacing. The method applies to a general class of convection-diffusion equations. It uses the original non-linear generalized Reynolds equation without linearization as in the previous methods, resulting in a very simple form. Superior stability is achieved by implementing proper convection-diffusion schemes. The combination of the alternating direction line sweeping method with a multi grid solver improves computational efficiency dramatically.

2.2 Generalized Reynolds Equation

2.2.1 Reynolds Equation

The governing equation for the gas lubricated bearing is the Reynolds equation, which can be written as

$$12\mu \frac{\partial}{\partial t}(ph) = \frac{\partial}{\partial x} \left(ph^3 \frac{\partial p}{\partial x} - 6U\mu ph \right) + \frac{\partial}{\partial y} \left(ph^3 \frac{\partial p}{\partial y} - 6V\mu ph \right) \quad (2.1)$$

where p is pressure, h is the local clearance, μ is the viscosity of the air; U and V are the velocity components of the moving surface in the x and y directions. In deriving this equation, the z velocity component and the inertial and body forces are neglected. A no-slip boundary condition is applied on both surfaces. The film thickness is assumed to be much smaller than the lateral dimensions and the pressure is assumed constant across the film thickness.

In our study, only the steady state air bearing solution is of interest. As will be shown, the numerical method used is very stable so that the steady state solution can be obtained from the steady state Reynolds equation directly, without using time stepping. Therefore, the unsteady term in Eq.(2.1) can be dropped.

2.2.2 Rarefaction Models

Although the film thickness is assumed to be small in the Reynolds equation, it still has to be large compared to the mean free path of the air (about 64 nm under standard conditions) in order for the no-slip condition to be valid. However, the minimum slider-disk separation in current drives has become smaller than the mean free path. Therefore, the rarefaction effect has to be taken into account. Various slip correction models have been proposed by Burgdorfer(1959, first order slip), Hsia and Domoto(1983, second order slip) and Gans(1985, higher order). Fukui and Kaneko (1988) derived a molecular gas lubrication model (FK model) based on the linearized Boltzmann equation. It can also be cast in a form similar to the Reynolds equation. The Direct Simulation Monte Carlo results of Alexander *et al.*(1994) confirmed the validity of the FK model for slider-disk spacing as low as 10 nm.

All the above correction models can be put into the following non-dimensional steady state generalized Reynolds equation

$$\frac{\partial}{\partial X} \left(QPH^3 \frac{\partial P}{\partial X} - \Lambda_x PH \right) + \frac{\partial}{\partial Y} \left(QPH^3 \frac{\partial P}{\partial Y} - \Lambda_y PH \right) = 0 \quad (2.2)$$

where $P = p / p_a$, $H = h / h_m$, $X = x / L$, $Y = y / L$ are the non-dimensionalized pressure, bearing clearance, coordinate in slider length direction and coordinate in slider width direction, respectively; p_a is the ambient atmospheric pressure; h_m is the reference clearance at the trailing edge center; L is the length of the slider; $\Lambda_x = \frac{6\mu UL}{p_a h_m^2}$ and $\Lambda_y = \frac{6\mu VL}{p_a h_m^2}$ are the bearing numbers in the x and y directions, respectively; U and V are the x and y velocity components, respectively; Q is the flow factor, and assumes different forms depending on the type of correction model used,

$$Q = 1, \quad \text{Continuum Model}$$

$$Q = 1 + 6a \frac{K_n}{PH}, \quad \text{First Order Slip Model}$$

$$Q = 1 + 6 \frac{K_n}{PH} + 6 \left(\frac{K_n}{PH} \right)^2, \quad \text{Second Order Slip Model}$$

$$Q = f \left(\frac{K_n}{PH} \right), \quad \text{Fukui-Kaneko Model}$$

where $a = \frac{2-\alpha}{\alpha}$ and α is the accommodation factor; $K_n = \frac{\lambda}{h_m}$ is the Knudsen number

and λ is the mean free path of the air; $f \left(\frac{K_n}{PH} \right)$ is as given by Fukui and Kaneko (1988).

The current implementation of the FK model uses the database table look-up method of Fukui and Kaneko (1990) to increase the computational efficiency.

2.3 Control Volume Formulation

2.3.1 Integration of the Generalized Reynolds Equation

The control volume method of Patankar (1980) is employed to solve the generalized Reynolds equation. His control volume formulation applies to a general class of convection-diffusion equations having the following form:

$$\frac{\partial}{\partial t}(\rho\phi) + \text{div}(\rho\mathbf{u}\phi) = \text{div}(\Gamma\text{grad}\phi) + S \quad (2.3)$$

where ϕ is the dependent variable, ρ is the density, Γ is the diffusion coefficient, \mathbf{u} is the flow velocity and S is the source term.

In two dimensions, the steady state equation without the source term can be written as

$$\frac{\partial J_x}{\partial X} + \frac{\partial J_y}{\partial Y} = 0 \quad (2.4)$$

where J_x and J_y are the total (convection plus diffusion) fluxes defined by

$$J_x \equiv \rho u \phi - \Gamma \frac{\partial \phi}{\partial X} \quad (2.5a)$$

$$J_y \equiv \rho v \phi - \Gamma \frac{\partial \phi}{\partial Y} \quad (2.5b)$$

where u and v denote the X and Y components of \mathbf{u} .

It is clear that Eq.(2.2) is a special case of Eq.(2.4-2.5), with $\phi = P$, $\rho = H$, $u = \Lambda_x$, $v = \Lambda_y$, and $\Gamma = QPH^3$. Here, the diffusion coefficient Γ is a function of the

dependent variable. Therefore, the equation is non-linear. The non-linearity of the equation is dealt with iteratively. At each iteration, Γ is updated using the newest value of the dependent variable. After making the above substitutions, Eq.(2.5) becomes

$$J_x \equiv \Lambda_x PH - \Gamma \frac{\partial P}{\partial X} \quad (2.6a)$$

$$J_y \equiv \Lambda_y PH - \Gamma \frac{\partial P}{\partial Y} \quad (2.6b)$$

where $\Gamma = QPH^3$.

The integration of Eq.(2.4) over the control volume shown in Fig. 2.1 gives

$$J_e - J_w + J_n - J_s = 0 \quad (2.7)$$

where J_e and J_w are $J_x \Delta Y$ evaluated at control volume face e and face w respectively; J_n and J_s are $J_y \Delta X$ evaluated at control volume face n and face s respectively.

2.3.2 Central Difference Scheme

The evaluation of the integrated fluxes, which need to be approximated using the values of the dependent variable at neighboring points, can cause difficulty in the numerical solution, especially for high bearing numbers. It seems natural to use the central difference scheme to represent the integrated fluxes. For example,

$$\begin{aligned} J_e &\equiv (\Lambda_x PH)_e \Delta Y - \left(\Gamma \frac{\partial P}{\partial X} \right)_e \Delta Y \\ &= \frac{1}{2} (\Lambda_x H)_e (P_E + P_P) \Delta Y - \Gamma_e \frac{(P_E - P_P)}{(\delta x)_e} \Delta Y, \end{aligned} \quad (2.8)$$

where Γ_e is calculated using the most current values of the dependent variable P , as mentioned previously. Other flux values can be obtained similarly. Let us define the convection coefficients

$$\begin{aligned}
F_e &= (\Lambda_x H)_e \Delta Y \\
F_w &= (\Lambda_x H)_w \Delta Y \\
F_n &= (\Lambda_y H)_n \Delta X \\
F_s &= (\Lambda_y H)_s \Delta X
\end{aligned} \tag{2.9}$$

and the diffusion coefficients

$$\begin{aligned}
D_e &= \frac{\Gamma_e \Delta Y}{(\delta x)_e} \\
D_w &= \frac{\Gamma_w \Delta Y}{(\delta x)_w} \\
D_n &= \frac{\Gamma_n \Delta X}{(\delta y)_n} \\
D_s &= \frac{\Gamma_s \Delta X}{(\delta y)_s}
\end{aligned} \tag{2.10}$$

By using Eq.(2.8)-Eq.(2.10), we can regroup Eq.(2.7) into the following form:

$$a_P P_P = a_E P_E + a_W P_W + a_N P_N + a_S P_S + b \tag{2.11}$$

where

$$a_E = D_e - \frac{F_e}{2} \tag{2.12a}$$

$$a_W = D_w + \frac{F_w}{2} \tag{2.12b}$$

$$a_N = D_n - \frac{F_n}{2} \tag{2.12c}$$

$$a_S = D_s + \frac{F_s}{2} \tag{2.12d}$$

$$a_P = a_E + a_W + a_N + a_S + (F_e - F_w + F_n - F_s) \tag{2.12e}$$

$$b = 0 \tag{2.12f}$$

The Peclet number measures the relative strength between convection and diffusion and is defined as

$$P \equiv F / D \quad (2.13)$$

It is clear from Eq.(2.12a)-Eq.(2.12d) that the coefficients can have negative values for absolute values of Peclet number great than 2. For example, $a_E < 0$ for $P_e > 2$ and $a_w < 0$ for $P_w < -2$. Negative coefficients violate one of the basic rules of discretization stated by Patankar (1980) and lead to divergence of the solution. The outcome is disastrous.

Another potential stability problem comes from Eq.(2.12e), where the terms in the parenthesis do not have zero sum. This is different from the case of the Navier-Stokes equation, where the sum in the parenthesis is always zero due to the continuity equation. A negative sum in the parenthesis makes the coefficient of Eq.(2.12e) less than the sum of the coefficients in Eq.(2.12a)-Eq.(2.12d) and de-stabilizes the solution. There is an easy fix for this problem, however, by rearranging Eq.(2.12e) and Eq.(2.12f), so that they become

$$a_p = a_E + a_w + a_N + a_S + \max(0, F_e - F_w + F_n - F_s) \quad (2.12g)$$

$$b = \max(0, F_w - F_e + F_s - F_n)P_p, \quad (2.12h)$$

where the dependent variable in Eq.(2.12h) is assumed to be known, using the most current value.

2.3.3 Stable Convective Schemes

A variety of schemes have been devised to overcome the stability problem of the central difference scheme. The resulting coefficients for these schemes can be summarized in the following unified form, after Patankar (1980):

$$a_E = D_e A(|P_e|) + \max(-F_e, 0) \quad (2.13a)$$

$$a_W = D_w A(|P_w|) + \max(F_w, 0) \quad (2.13b)$$

$$a_N = D_n A(|P_n|) + \max(-F_n, 0) \quad (2.13c)$$

$$a_S = D_s A(|P_s|) + \max(F_s, 0) \quad (2.13d)$$

$$a_P = a_E + a_W + a_N + a_S + \max(0, F_e - F_w + F_n - F_s) \quad (2.13e)$$

$$b = \max(0, F_w - F_e + F_s - F_n) P_P \quad (2.13f)$$

where the function $A(|P|)$ depends on the convective scheme chosen,

$1 - 0.5 P $	central difference
1	upwind
$\max(0, 1 - 0.5 P)$	hybrid
$\max(0, (1 - 0.1 P)^5)$	power-law
$ P / (e^{ P } - 1)$	exponential

A detailed comparison between different schemes is given in Chapter 5. It is determined that the hybrid scheme is the most suitable for air bearing simulations.

2.4 Mass Flow Averaging for Clearance Discontinuities

2.4.1 Formulation

The slider air bearing has a geometrical peculiarity, namely, the clearance discontinuities. This poses numerical difficulty for finite difference methods based on the differential form of the Reynolds equation. An artificial smooth function has to be used in place of the discontinuity, thus reducing the accuracy of the solution. In the

present integrated control volume formulation, the clearance discontinuity does not cause any numerical difficulty. However, when a discontinuity crosses the boundary of a control volume, accuracy can be improved by using the mass flow averaging scheme of Kogure *et. al* (1983) and Cha *et. al* (1995). In this technique the mass flux on a control volume boundary with discontinuity is averaged by appropriately weighting the contribution from both sides of the discontinuity. When averaging is used, the mass fluxes become

$$J_x = \xi \bar{J}_x + (1 - \xi) \hat{J}_x \quad (2.14a)$$

$$J_y = \eta \bar{J}_y + (1 - \eta) \hat{J}_y \quad (2.14b)$$

where \bar{J}_x is obtained by applying Eq.(2.6) to one side of the discontinuity, \hat{J}_x is obtained by applying Eq.(2.6) to the other side of the discontinuity; \bar{J}_y and \hat{J}_y are calculated similarly; ξ and η are the weighting factors for the different heights across the discontinuities.

2.4.2 Implementation

As the performance requirement of air bearings becomes more stringent, designs become more and more complex. While shaped rails have become standard, multiple etch depths are also being used to exert more control over air bearing flying characteristics. There are numerous possibilities of intersections between different recess areas. Therefore, it is not practical to analytically determine the location of the clearance discontinuity in the general case, as in the previous implementation of the code (Cha, 1993).

An alternative method has been used in the current implementation to determine the weighting factors (Fig. 2.2). It is assumed that no more than one discontinuity is present on each side of the control volume boundary (the grid is fine enough), since it is not practical to resolve multiple discontinuities on one side of the control volume. First, the recess depths at a series of points are sampled on the control volume boundary. The maximum h_{\max} , the minimum h_{\min} and the average h_{avg} are obtained. Next, by assuming the recess at any point along the boundary is either h_{\max} or h_{\min} , and knowing h_{avg} , the weighting factor can be deduced. This simple method can be applied to the most general case of shaped rail designs with multiple recess depths.

2.5 Mass Flow Patterns

2.5.1 Stream Function

The Eq.(2.4) is essentially a mass conservation equation. By defining a stream function, the averaged mass flow pattern can be obtained by integration of the mass fluxes. It can be helpful for understanding particle movement inside the air bearing and facilitate the design of air bearings less prone to particle contamination.

By virtue of Eq.(2.4), there exists a stream function ψ such that

$$J_x = \frac{\partial \psi}{\partial Y} \quad (2.15a)$$

$$J_y = -\frac{\partial \psi}{\partial X} \quad (2.15b)$$

2.5.2 Integration of the Stream Function

After the pressure solution is obtained, the mass fluxes can be calculated using Eq.(2.4). Starting from one corner of the computational domain, for example, the lower

left corner, integrate Eq.(2.15b) to obtain ψ along the entire bottom boundary. Then starting from each point of the bottom boundary, integrate Eq.(2.15a) all the way to the top boundary. After ψ is obtained in the entire domain, the contour plot for ψ gives the mass flow pattern integrated in the clearance direction.

Although the procedure outlined above is quite simple, care should be taken to use proper grid nodes where ψ is calculated. Let the index pair (i, j) denote the current point P, and let $J_{ni,j}$ be the J_n at point P, etc. When the grid for ψ is chosen to be the same as the pressure grid (Fig. 2.1), the integration of Eq.(2.15) renders

$$\psi_{i+1,j} = \psi_{i,j} - (J_{ni+1,j} + J_{si+1,j} + J_{ni,j} + J_{si,j}) / 4 \quad (2.16a)$$

$$\psi_{i,j+1} = \psi_{i,j} + (J_{ei,j+1} + J_{wi,j+1} + J_{ei,j} + J_{wi,j}) / 4 \quad (2.16b)$$

where the mass fluxes have to be averaged to approximate the value at the middle of the integration interval. Note also $J_{ni,j} = J_{si,j+1}$, $J_{ei,j} = J_{wi+1,j}$, etc. The averaging of mass fluxes violates the conservation property of the original equation and may degrade the resulting streamlines.

A more accurate method is to position the stream function grid lines half way between the pressure grid lines. This is called a staggered grid arrangement, a term used in computational fluid dynamics where the pressure grid and velocity component grids are different. In this case, the stream function grid lines coincide with the control volume faces in Fig. 2.1. The nodes for the stream function are the corners of the pressure control volume. Now the mass flux values are available in between the stream function grid points and no averaging is necessary. The conservation property of the solution is maintained. The integration of Eq.(2.15) produces

$$\psi_{i+1,j} = \psi_{i,j} - J_{si+1,j+1} \quad (2.17a)$$

$$\psi_{i,j+1} = \psi_{i,j} + J_{wi+1,j+1} \quad (2.17b)$$

As an example, Fig. 2.3 is a mass flow pattern obtained using the above method for the “Nutcracker” slider. This is a negative pressure slider design, which is discussed in detail in Chapter 6. It can be seen that the streamlines are very dense in the recess areas. This is because the mass flow rate is much higher due to the large spacing in the recess areas. It is also shown that the streamlines in the recessed areas largely follow the contour of the rail shape, because only a small portion of the flow can squeeze into or out of the bearing area.

2.6 Pressure Solution for Given Slider Attitude

2.6.1 The Line Sweeping Method

The most basic solution needed in the air bearing simulation is the pressure distribution for a given slider flying attitude (fly height, pitch and roll). Two levels of iteration are needed to solve the discretized equation having the form of Eq.(2.11). The outer iteration updates the coefficients in Eq.(2.11) using the most current values of the pressure. The inner iteration solves the linear system of Eq.(2.11) iteratively.

An alternating direction line-by-line method is implemented as the solver for the inner iteration. In this method, a grid line is chosen and the pressure on the neighboring grid lines are assumed to be known from their latest values. The pressure along the chosen line can then be obtained using the tri-diagonal algorithm. The grid lines are chosen one by one successively in one direction, from upstream to downstream when there is a dominant flow direction. Then the same is applied to the other direction.

The convergence rate for the line sweeping method is much faster than that of the point-by-point iterative method, because the boundary information is transmitted immediately across the whole line from both ends of the line. Line sweeping in the flow direction also improves efficiency, because downstream points are more influenced by upstream points than the other way around. Alternating the sweeping direction allows information on all boundaries to propagate quickly to the interior.

2.6.2 Convergence Criterion

Choosing an appropriate convergence criterion is important for getting a meaningful solution. The relative change in the dependent variable is often used to measure convergence, particularly for solution methods using time stepping and under-relaxation. This is sometimes misleading and dangerous. If very small time steps or strong under-relaxation are used, the dependent variable changes very little. In some cases, the convergence rate is simply very slow or the solution is stalled. The above criterion may proclaim convergence when in fact the results are totally incorrect.

Convergence of the solution should be measured directly by the residual of Eq.(2.11),

$$R_p = a_p P_p - a_e P_e - a_w P_w - a_n P_n - a_s P_s - b \quad (2.18)$$

Zero residual implies complete convergence. Of course, with iterative methods and finite precision computation, it is unachievable. In reality, the solution is deemed converged when the absolute value of the residual is smaller than a preset value. There are mainly two alternatives to judge the convergence of the whole field. One is to use the maximum absolute residual at all grid points. The other is to compute some normalized average residual. In the current implementation, the global residual is defined as

$$R = \frac{\sum_p |R_p|}{\sum_p |a_p P_p|} \quad (2.19)$$

2.6.3 Multi Grid Method

Although the line sweeping method is much faster than the point-by-point method, it still has the generic disease of iterative methods on a single grid. The main symptom is that the solution converges fast initially, but it becomes progressively slower with each iteration. Brandt (1977) demonstrated that it is due to the inefficiency in smoothing the long wavelength error components that slows down the convergence process on a single grid. He developed the multi-grid method that overcomes this difficulty by moving the solution back and forth between a set of different grid levels to efficiently smooth the error components of all wave lengths. The multi-grid method suggested by Shyy and Sun (1992) has been implemented in the current simulator, which dramatically improves the solver efficiency. Speed improvements of 10 to 100 times have been observed. The details of the multi grid implementation is given in Chapter 4.

2.7 Solution for Steady State Fly Height

2.7.1 Inverse Solution

In most air bearing simulations, the air bearing attitude is the desired results for given suspension load. This is called the inverse problem.

The solution starts at a guessed slider attitude. The pressure distribution is solved for, and the resulting bearing force as well as pitch and roll moments are compared to the suspension load and the applied static pitch and roll torques respectively. When the difference is greater than the specified number, the Quasi-Newton iteration method (Cha,

1993) is employed to search for the new slider attitude. The advantage of this method is that it requires the calculation of the Jacobian matrix (compliance matrix) only once. The Jacobian matrix is updated in all subsequent iterations without full re-evaluation.

The non-dimensionalized bearing load and location can be expressed as

$$\begin{aligned}
 W &= \int_0^b \int_0^1 (P-1) dXdY \\
 \bar{X} &= \frac{1}{W} \int_0^b \int_0^1 X(P-1) dXdY \\
 \bar{Y} &= \frac{1}{W} \int_0^b \int_0^1 Y(P-1) dXdY
 \end{aligned} \tag{2.20}$$

where b is the slider's width non-dimensionalized by the slider's length. Let $W_0, (X_0, Y_0)$ be the suspension load and load point location non-dimensionalized by $p_a L^2$ and L respectively; let M_p and M_r be the static pitch and roll torque non-dimensionalized by $p_a L^3$. Then the normalized force imbalance is defined as

$$R_f = \left| \frac{W - W_0}{W_0} \right| + \left| \frac{W(\bar{X} - X_0) + S_p - M_p}{W_0} \right| + \left| \frac{W(\bar{Y} - Y_0) + S_r - M_r}{W_0} \right| \tag{2.21}$$

where S_p and S_r are the pitch and roll moment of the shear force. The effect of the shear moments is discussed in the next section. R_f is used as the convergence criterion for the Quasi-Newton search of the steady state slider flying attitude.

2.7.2 Shear Force Effect

The effect of shear force generated by the air flow under the air bearing has not been included in the previous simulations. This does not cause significant error when the fly height is relatively large. However, with the slider fly height reducing to near contact, the shear force may become significant. Also, the shear force increases with the rotation

speed of the disk. The omission of the shear force in the simulation may lead to over-prediction of slider pitch. Its effect on the fly height depends on the air bearing stiffness.

The shear stress can be calculated from the velocity gradient at the air bearing surface. In the simulation, the air bearing pressure is obtained using the Boltzmann equation (FK) model of Fukui and Kaneko (1988). However, it would be numerically quite involved to obtain the velocity gradient using the FK model. Instead, the velocity profile of the first-order slip model (Burgdorder, 1959) is assumed. This approximation should make little difference since the first-order slip model solution is quite close to that of the FK model and the total shear force is small compared to the air bearing force. Let Z be the slider thickness non-dimensionalized by L , the pitch and roll moments of the shear force, non-dimensionalized by $p_a L^3$, can be expressed as:

$$\begin{aligned} S_p &= Z \left(\frac{h_m}{L} \right) \int_0^b \int_0^1 \left(\frac{H}{2} \frac{\partial P}{\partial X} + \frac{\Lambda_x}{6(H + 2K_n)} \right) dXdY \\ S_r &= Z \left(\frac{h_m}{L} \right) \int_0^b \int_0^1 \left(\frac{H}{2} \frac{\partial P}{\partial Y} + \frac{\Lambda_y}{6(H + 2K_n)} \right) dXdY \end{aligned} \quad (2.22)$$

The shear force creates a pitching moment on the slider which tends to lower the pitch angle. This leads to increased trailing edge fly height in some cases. Here, the effects of shear force are compared on two air bearing designs: one Tri-pad slider (Fig. 2.4) and one sub-ambient pressure slider (Nutcracker, Fig. 2.5). Examples of the 3-D pressure profiles for these designs are given in Fig. 2.6 and Fig. 2.7, respectively. In the Tri-pad design, there is only a small rear bearing surface which leads to a very soft bearing with low trailing edge pitch stiffness. Therefore, it is expected that the shear force will have a more pronounced effect on the Tri-pad design than on the Nutcracker slider.

It can be seen from Fig. 2.8 that the fly height for the Tri-pad slider increases by about 12% when shear force is taken into account in the simulation, while the fly height for the Nutcracker slider (Fig. 2.9) decreases by a very small amount. The pitch change is similar for the two designs (Fig. 2.10 and Fig. 2.11). The skew angle changes from 1.2 deg. at the ID to -17.4 deg. at the OD for the Tripad slider, while it goes from 3.88 deg. at the ID to 1-17.85 deg. at the OD for the Nutcracker slider. The sign and magnitude of the roll torque is determined by the skew angle, as is reflected in the roll changes illustrated in Fig. 2.12 and Fig. 2.13.

The results shown imply that it is necessary to include the shear force in simulating soft, near contact sliders such as the Tri-pad slider.

2.8 Summary

A convection-diffusion control volume method is outlined for the solution of the generalized Reynolds equation. It is both mathematically simple and computationally efficient because the stability of the algorithm allows the direct solution of the steady state equation without time marching. A tri-diagonal solver coupled with the multi grid method provides superior speed. The mass flux averaging technique can apply to arbitrarily shaped rails with multiple recess depths. The mass flow patterns obtained on a staggered grid can help in anti-contamination slider designs. Inclusion of the shear force improves accuracy for sliders with low air bearing stiffness.

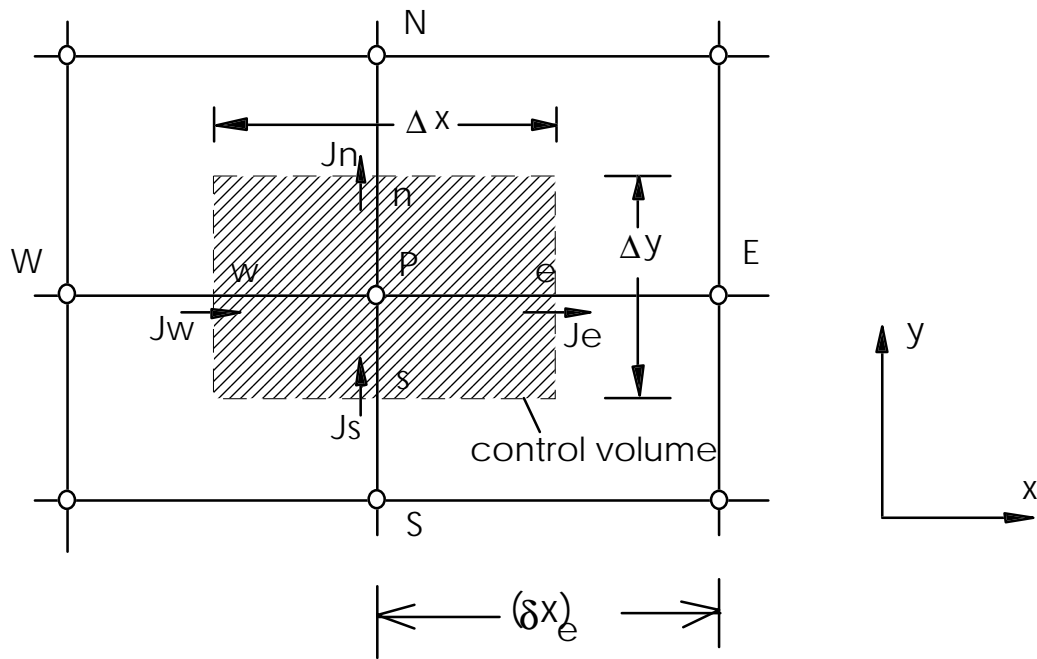


Fig. 2.1 Illustration of the control volume (after Patankar, 1980)

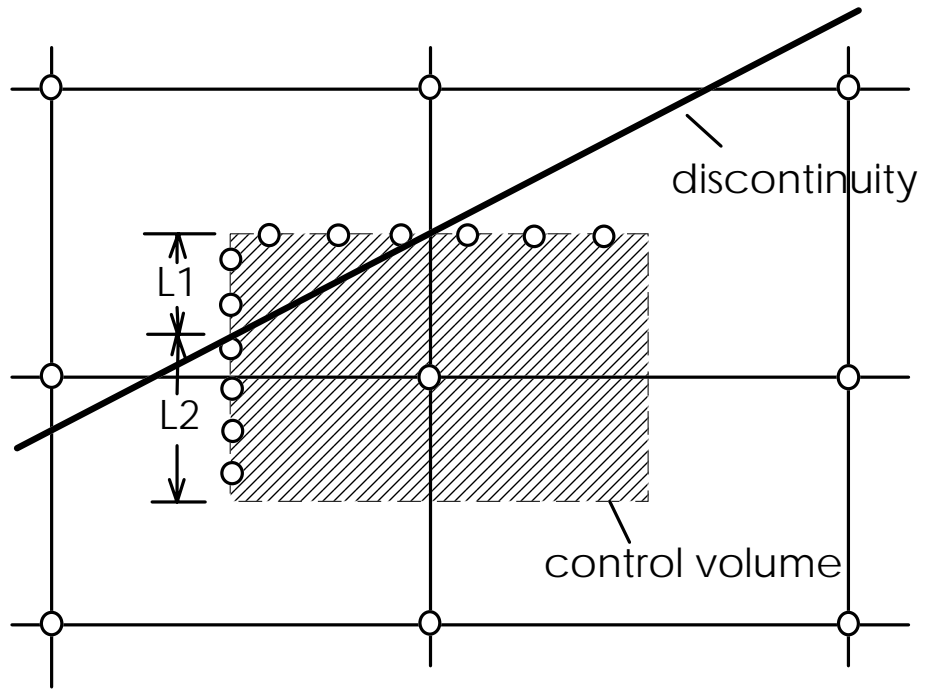


Fig. 2.2 Mass flow averaging scheme for clearance discontinuity

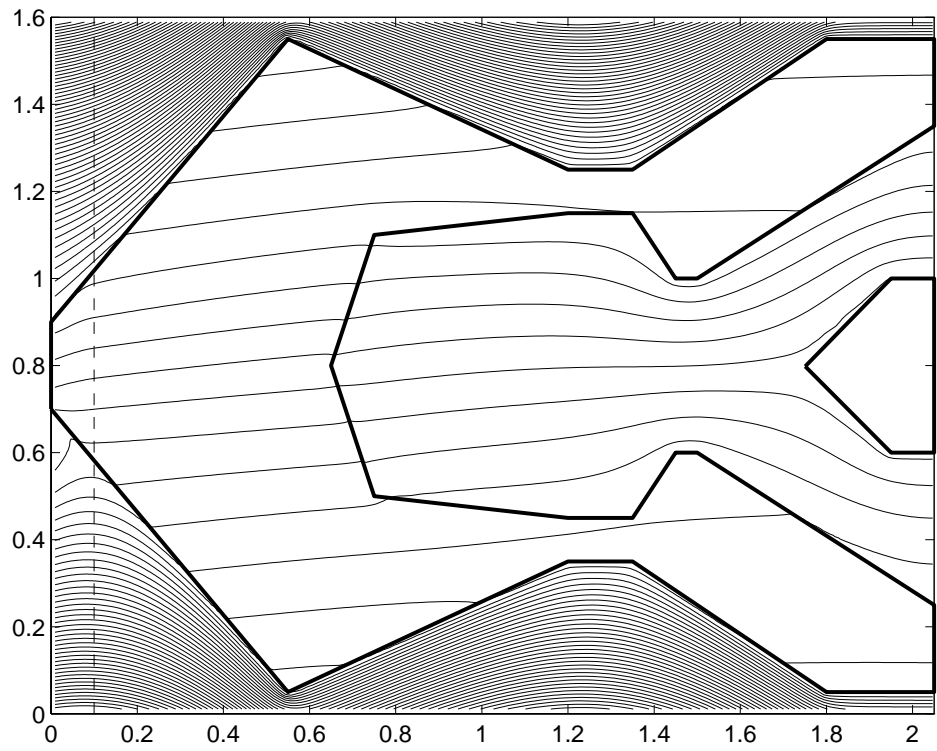


Fig. 2.3 Mass flow pattern on the staggered grid for the Nutcracker slider

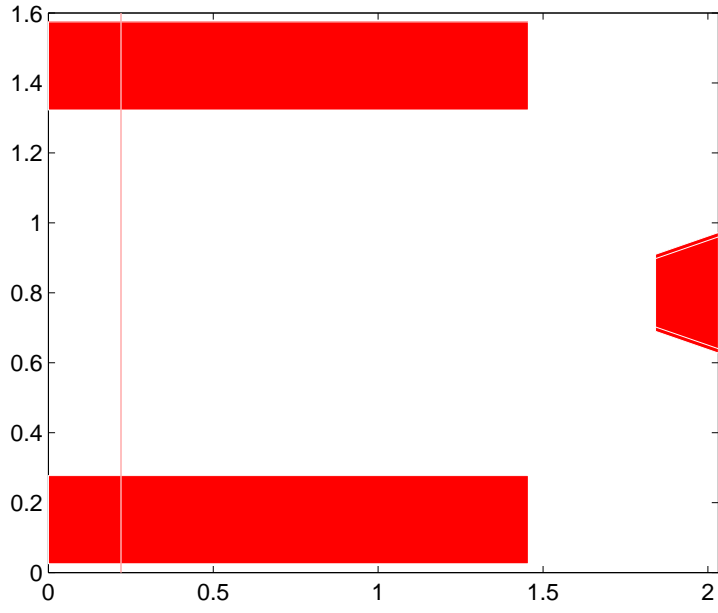


Fig. 2.4 Rail shape of the Tripad slider

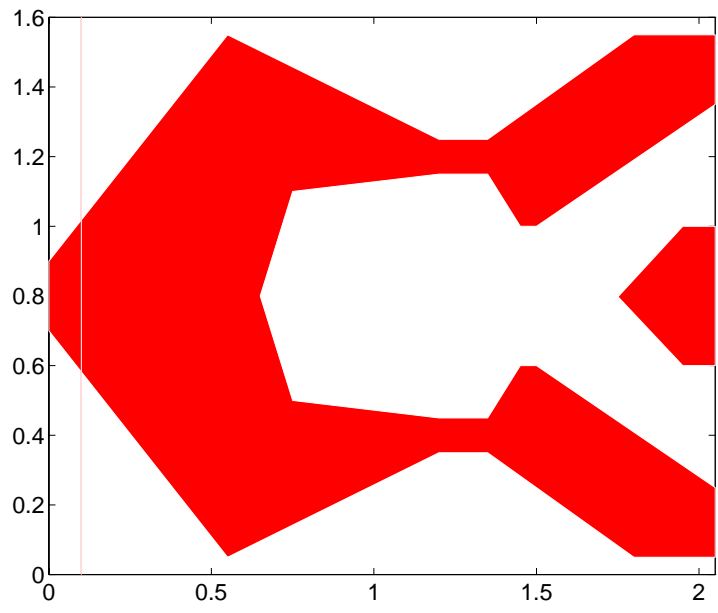


Fig. 2.5 Rail shape of the Nutcracker slider

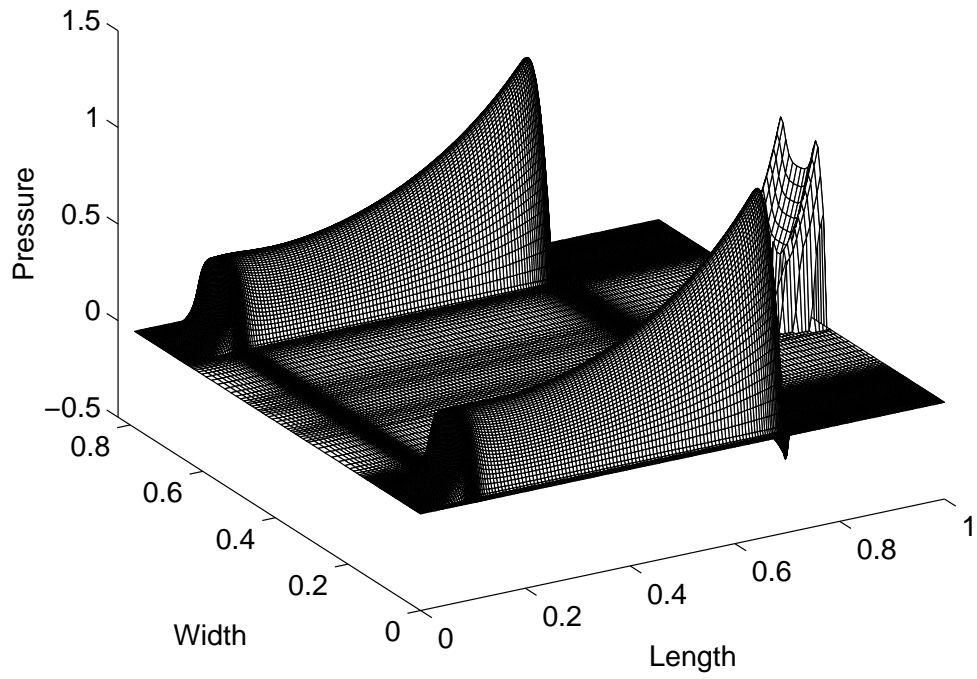


Fig. 2.6 3-D pressure profile for the Tripad slider

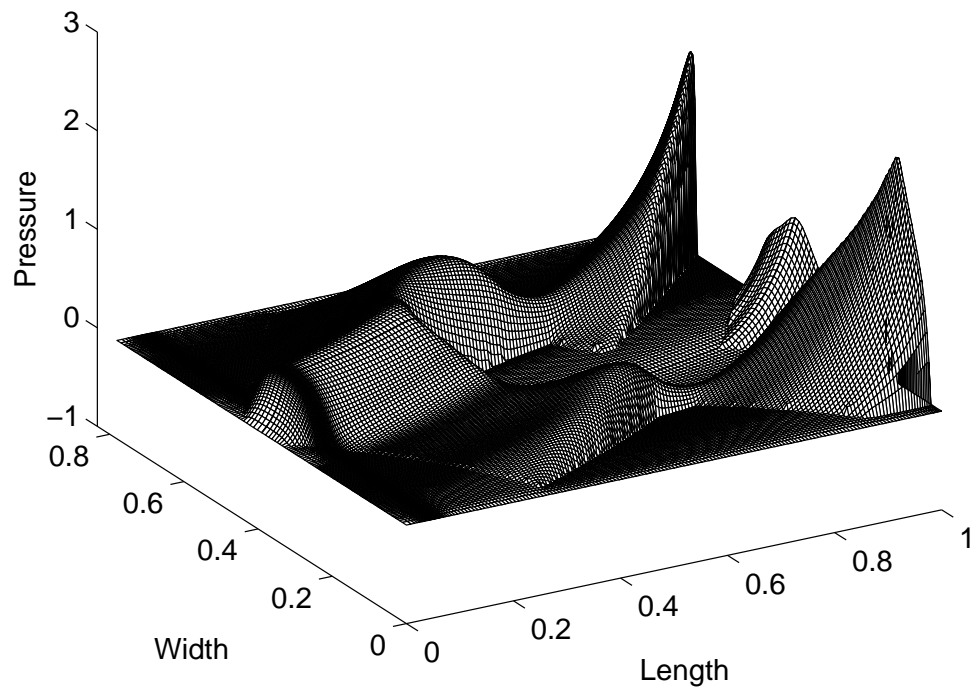


Fig. 2.7 3-D pressure profile for the Nutcracker slider

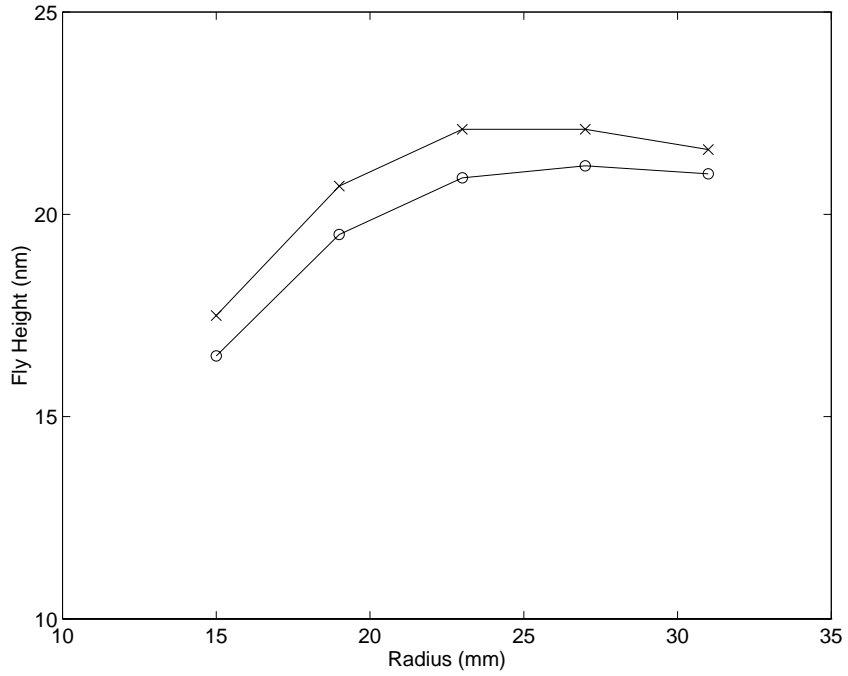


Fig. 2.8 Fly height profile for the Tripad with (x) and without (o) shear effect

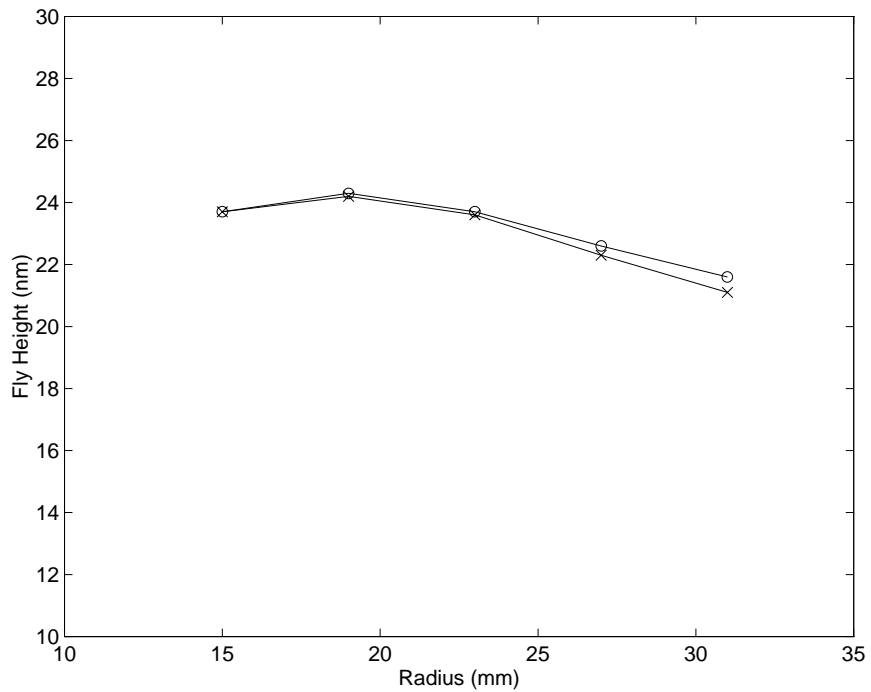


Fig. 2.9 Fly height profile for the Nutcracker slider with (x) and without (o) shear effect

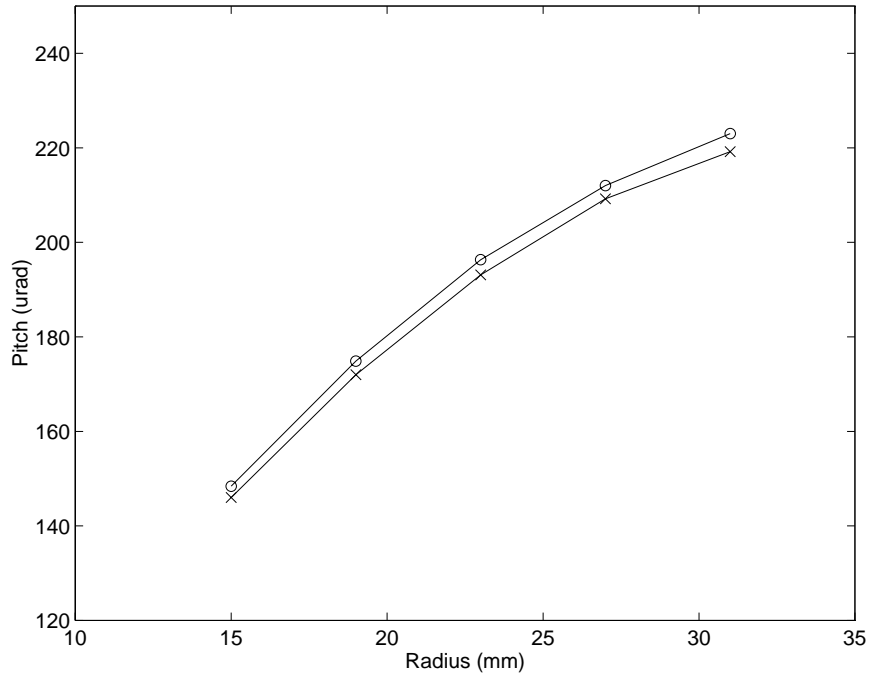


Fig. 2.10 Pitch angle of the Tripad slider with (x) and without (o) shear effect

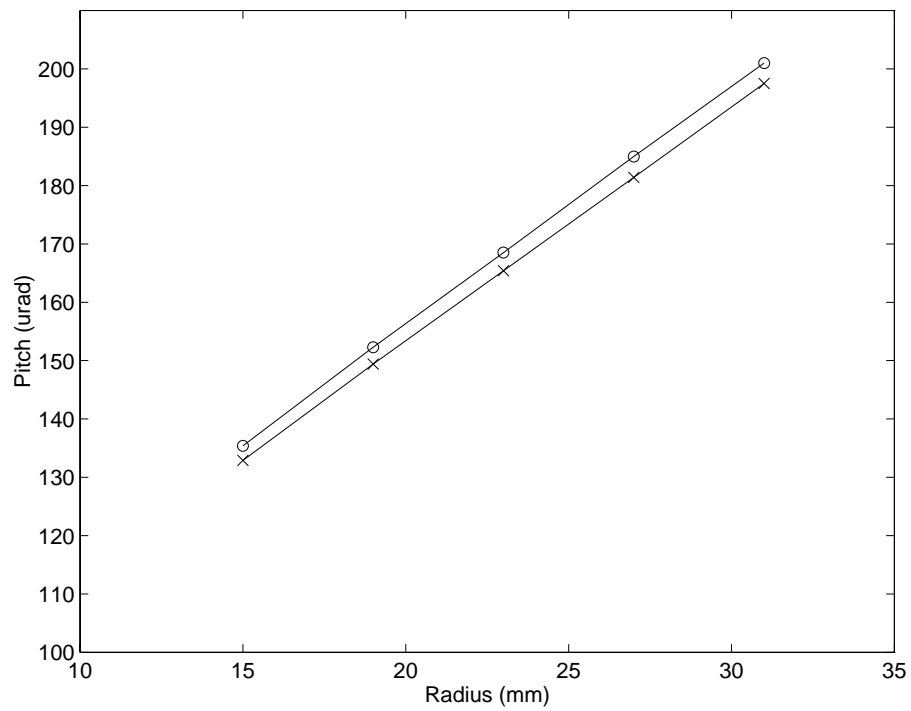


Fig. 2.11 Pitch angle of the Nutcracker slider with (x) and without (o) shear effect

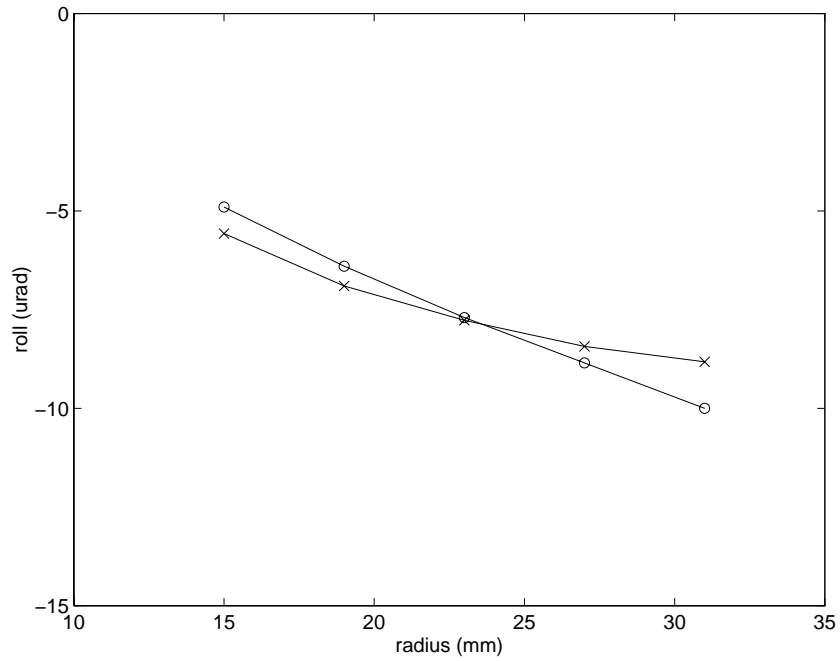


Fig. 2.12 Roll of the Tripad slider with (x) and without (o) shear effect

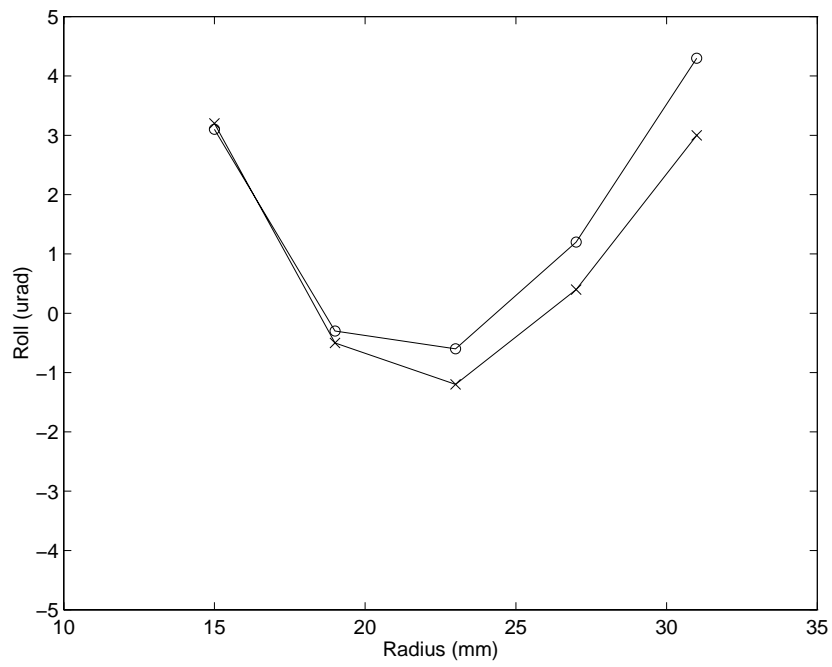


Fig. 2.13 Roll of the Nutcracker slider with (x) and without (o) shear effect

CHAPTER 3

COMPUTATIONAL GRID

3.1 Introduction

A successful numerical solution depends as much on an adequate grid as on the numerical algorithm used. The solution of the generalized Reynolds equation entails additional grid requirements due to the special geometry of the slider air bearing surface. In particular, the discontinuities along the rail edges and the front taper have to be treated carefully to ensure meaningful solutions.

In the current implementation, the Reynolds equation is discretized on a rectangular grid using a control volume formulation. The variable grid scheme based on geometric progression has been popular in finite difference solutions, because it gives the user the control to put more grid lines where needed and provides smooth transition from a coarse grid region to a fine grid region. The current code implements a piece-wise geometric progression grid. In this method, the computational domain is divided into several intervals in both directions, and a geometric progression is used in each interval. It is important that the grid sizes at the junction of two intervals be comparable in order to minimize numerical error.

The grid line location in some critical areas can significantly affect solution accuracy due to the special nature of the air bearing geometry (clearance discontinuity, change of slope at the taper end). The effect of “grid snapping” is examined.

Although the piece-wise geometric progression method is very flexible, it can be tedious to use. An adaptive grid method based on pressure gradient is implemented to

facilitate grid generation. After the pressure solution is obtained on an initial grid, the pressure gradient field is evaluated. The grid is then redistributed so that the grid is more concentrated in areas where the pressure gradient is high.

3.2 Grid Generated by Geometric Progression

In this method, the computational domain is first divided into intervals in both the X and Y directions. The end points of intervals are called the control points. The coordinates of these control points as well as their grid indices are given. Therefore, the number of grid lines in each interval is known. For each interval, an expansion ratio is given. It is the ratio of successive grid step sizes. Then a geometric progression is used to generate the grid distribution in each interval. The grid becomes progressively coarser with a ratio larger than unity. A symmetry flag can be set for the Y direction so that only half the slider width need be specified. The second half of the grid is generated by creating a mirror image of the first half.

The IBM Tri-rail slider (Fig. 3.1) is used as an example for the piece-wise geometric progression grid generation. A sample 3-D pressure distribution is illustrated in Fig. 3.2. The parameters in Table 3.1 are used to generate the grid plotted in Fig. 3.3. The grid size used is 193×193 . Note that the boundary points of the domain need not be specified as the grid control points, because they do not change. There is one more grid ratio than the number of control points, because n control points divides the domain into $(n + 1)$ intervals.

3.3 Grid Snapping

3.3.1 Grid Snapping at the Taper End

The geometry of the slider air bearings is very special. It contains clearance discontinuities or steep slopes. At the taper end, there is also an abrupt change of slope. It is very important to align grid lines at the discontinuities as well as the taper end.

The Tri-rail slider is also used to study the effect of the grid snapping at the taper end. An initial uniform mesh of 65 x 65 is generated. In Fig. 3.4, the normalized coordinates of grid lines 10 and 11 (the thick lines) are 0.140625 and 0.15625, respectively. The normalized taper length is varied between these two points at five equal intervals of 0.003125, while the recess depth at the taper front remains at 3.9 μm . The slider is set at an attitude where the fly height, pitch and roll are 75 nm, 100 μrad and -8 μrad , respectively. When grid snapping is used, the grid line closest to the taper end is snapped to the taper end location. In this case, grid line 10 is snapped to the taper end for the first three taper end locations, and grid line 11 is snapped for the other locations.

The change of the air bearing load with taper end location is plotted in Fig. 3.5. It can be seen that the computed air bearing load experiences large fluctuations when the original grid is kept unchanged, while grid snapping makes the bearing load variation much smoother.

3.3.2 Grid Snapping on the Rail Boundary

The steep clearance change along the rail boundaries may also cause significant numerical errors if care is not taken in grid generation. In the grid snapping implementation, the grid nodes closest to the rail boundary points are snapped to the rail boundary. The two grid lines associated with the node are also moved in order to maintain a rectangular grid.

The steady state fly height for the Tri-rail slider is solved for on grid sizes from 65 x 65 to 193 x 193 with an increment of 16 x 16. The grid is generated using the adaptive grid method discussed in the next section. The solution with grid snapping is compared to the one without grid snapping. The fly height, pitch and roll are compared in Fig. 3.6, Fig. 3.7 and Fig. 3.8, respectively. While the fly height variation is only a little smoother with grid snapping, grid snapping makes a big difference in the results for pitch and roll. The solution displays large fluctuations in both pitch and roll in the grid convergence process when grid snapping is not used.

Grid snapping is most effective when the rails all have straight boundaries, as in the case of the TPC slider (Fig. 3.9). The grid lines can then be aligned with all the rail boundaries, describing the rail geometry accurately. The difference between the TPC slider and the conventional taper flat slider is that there are partially recessed areas on both sides of the rails. The 3-D pressure distribution is plotted in Fig. 3.10. By compressing and expanding the incoming flow at a skew angle using the partially recessed steps, the TPC slider can be designed to provide constant fly height across the entire disk radius. However, this design is quite sensitive to the rail width and rail alignment.

To study the grid snapping effect, the grid size is varied from 49 x 49 to 97 x 97 with increments of 16 x 16. The adaptive grid method described in the next section is also used to generate the grid. Without using grid snapping, large fluctuations of the fly height and roll are evident in Fig. 3.11 and Fig. 3.13, respectively. A large pitch increase without grid snapping can also be observed from grid size 49 x 49 to 65 x 65 (Fig. 3.12).

In dramatic contrast, with grid snapping the fly height and roll almost remain constant for all grid sizes, while the pitch increases slightly with grid size.

3.4 Adaptive Grid

Although the piece-wise geometric progression method is flexible, it is not always convenient to use. It is sometimes difficult to arrive at a satisfactory grid distribution. Therefore, some kind of automatic mesh generation scheme is desirable. To this end, an adaptive grid method has been implemented. While it does not guarantee the 'best' grid for all rail designs, it does provide very reasonable grid distributions in most cases. In this method, the pressure gradient field is first obtained from the initial calculation, which usually starts from a uniform grid. Then, the grid is redistributed using the pressure gradient field as the grid density function and the pressure solution is obtained again. This is normally done twice in the program.

There are two alternatives for calculating the pressure gradient to be used as the grid density function. For any location in the x direction, there are many different y stations, and vice versa. Either the averaged pressure gradient ($ipmax = 0$) or the maximum pressure gradient ($ipmax = 1$) among these different stations can be used as the grid density at that location. The choice between the two depends on the slider design with experience as the best guidance. The rule of thumb for a sound grid is that all important features should be covered by enough grid lines. In some designs with isolated small features, the large pressure gradient on the feature may be lost after averaging, resulting in insufficient grid distribution on the feature. The Tri-pad slider is an example. The 3-D pressure distribution in Fig. 3.14 is on a grid obtained using averaged pressure

gradient ($ipmax = 0$). It can be seen that the pressure peak on the rear center pad is very high, and yet the grid distribution on the pad is too coarse. The rear pad received sufficient grid coverage after switching to maximum pressure gradient ($ipmax = 1$), as illustrated in Fig. 3.15.

The computed pressure gradient still cannot be used directly as the grid density function. Fig. 3.17 depicts the grid distribution for the Seagate AAB slider (Fig. 3.16), using the calculated grid density. There are a couple of problems with this grid. The first problem has to do with the smoothness of the grid. Abrupt change in grid size causes numerical errors. A smoothing technique is employed in the program such that the pressure gradient at one location affects not only the grid density at that location, but it also has an exponentially decaying effect on the neighboring locations. The parameter *decayfactor* controls how fast its influence on the neighboring locations decays. For large *decayfactor*, the decay is fast and there is less smoothing effect. The recalculated grid, as a result of setting *decayfactor* to 60, is shown in Fig. 3.18. It is much smoother than the one in Fig. 3.17, particularly near the trailing edge. Another problem remains with this grid distribution. There is virtually no horizontal grid line in the large middle area, because the vertical pressure gradient in this area is almost zero. It may introduce significant errors when the pressure is integrated to get the bearing load. A few grid lines are desired in this area. A parameter called *difmax*, which is the allowable ratio of maximum to minimum pressure gradient, is used in the program. For any pressure gradient below that level, it is assigned the minimum gradient allowable. The grid shown in Fig. 3.19 uses a *difmax* of 30. It now has a few horizontal lines in the middle of the slider. The 3-D pressure distribution for this grid is given in Fig. 3.20.

In most slider air bearing designs, there is a taper region at the leading edge. The importance of grid snapping at the taper end was illustrated in the last section. It is equally important to have enough grid resolution because there is a rapid rise in pressure near the taper end. When the grid is prescribed manually using the piecewise geometric progression method, it is of course possible to concentrate the grid sufficiently at the taper end. However, when the adaptive grid is used, sometimes the grid concentration there may not be enough if only the calculated grid density is used. Therefore, an automatic concentration algorithm is used at the taper end. The program checks the number of grid points covered in the pressure rise region near the taper end. The grid is artificially concentrated until it meets the preset density level.

3.5 Summary

The piece-wise geometric progression method is implemented for grid generation. It is shown to be critical to align the grid lines at clearance discontinuities as well as at the taper end whenever possible, in order to obtain consistent results. Otherwise, the solution has large fluctuations when the grid line location or the rail geometry is changed.

Although very flexible, the geometric progression method is not always convenient to use. Sometimes many adjustments are necessary to obtain a reasonable mesh. An adaptive grid method based on pressure gradient automates the grid generation process and improves the grid quality.

X controls coordinates(mm)	0.39, 1, 1.733, 2.1
X controls grid indices	40, 80, 120, 150
X Grid ratios	0.98, 1.04, 0.96, 1.04, .098
Y symmetry	Yes
Y controls coordinates(mm)	0.321, 0.45, 0.574
Y controls grid indices	40, 48, 56
Y grid ratios	1, 1.2, 0.85, 1

Table 3.1 Example of piece-wise geometric progression grid specification

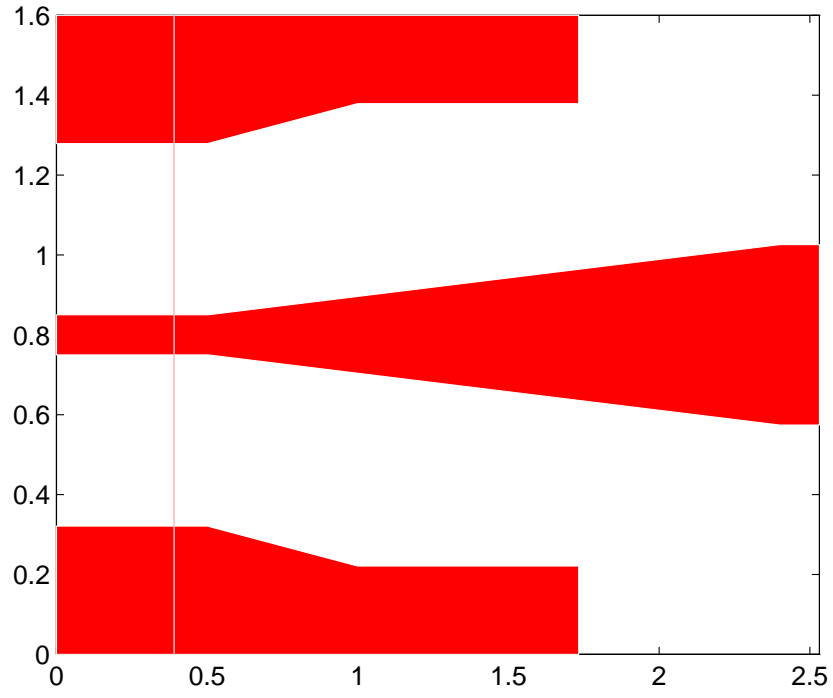


Fig. 3.1 Rail shapes of the IBM Tri-rail slider

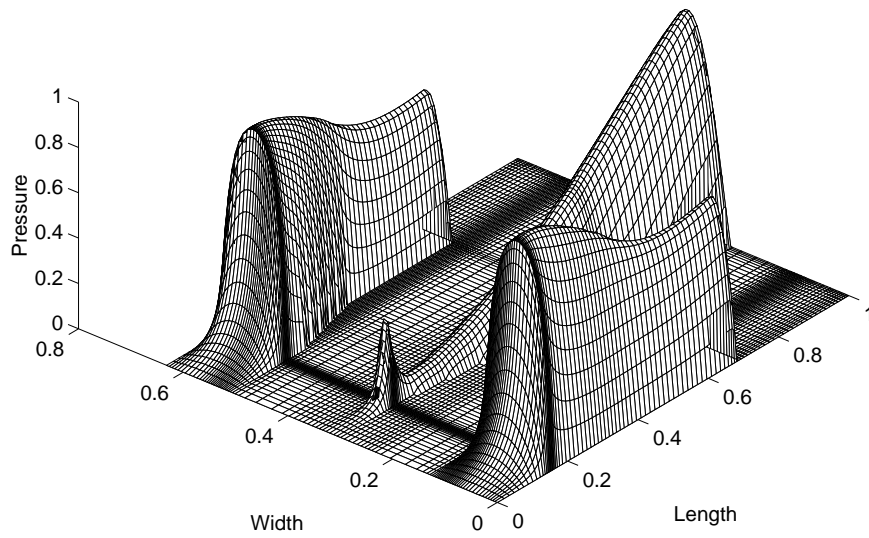


Fig. 3.2 3-D pressure profile of the Tri-rail slider. Radius = 20 mm, skew = 0°

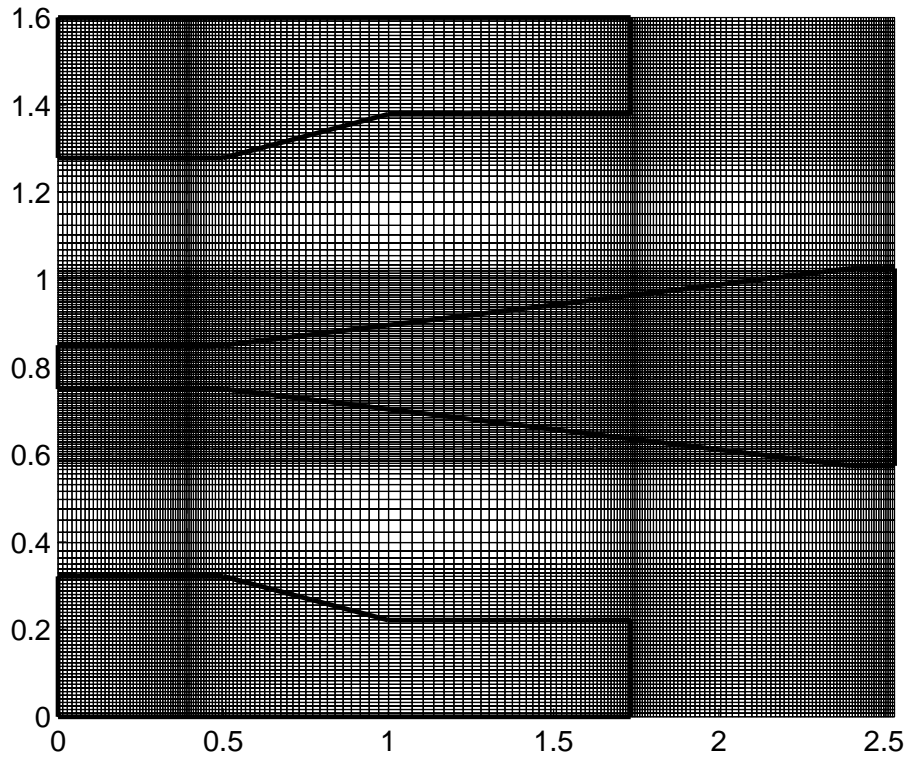


Fig. 3.3 Sample grid distribution for the IBM Tri-rail slider

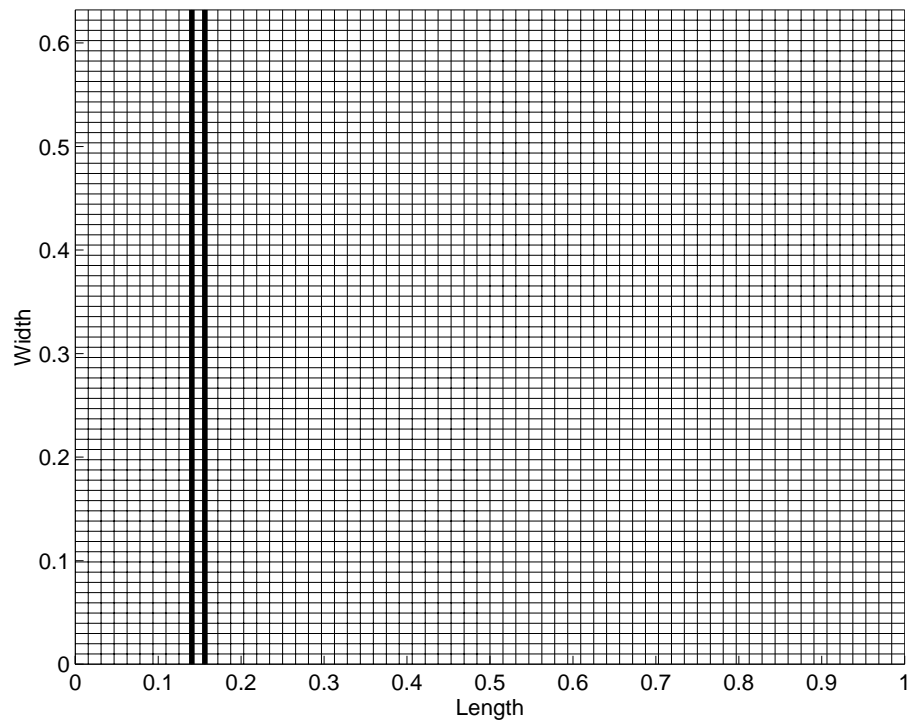


Fig. 3.4 Grid used for studying grid snapping effect at the taper end. Grid size: 65 x 65.

The taper end varies between the two thick lines.

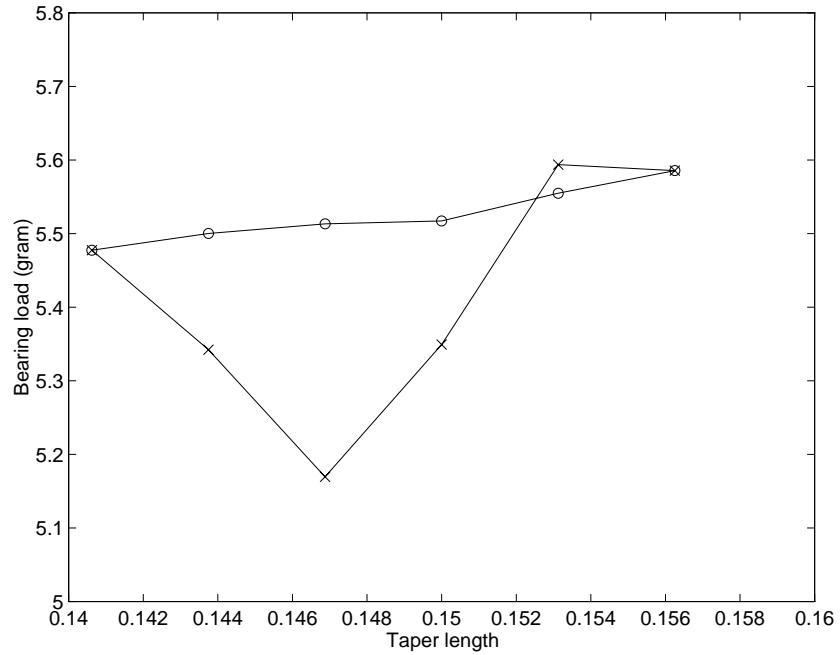


Fig. 3.5 Effect of grid snapping at the taper end. (o): with grid snapping; (x): without grid snapping

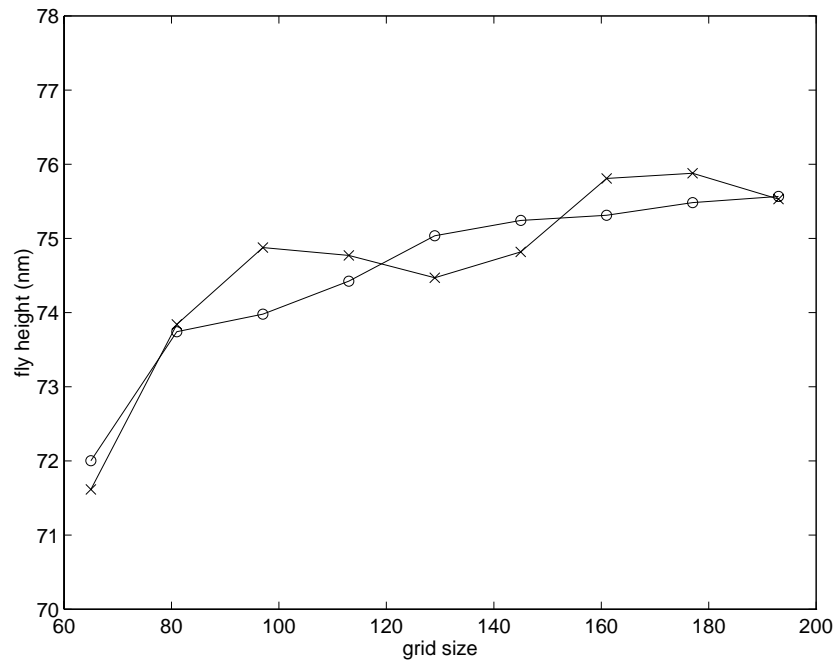


Fig. 3.6 Convergence of Tri-rail fly height with grid size. (o): with grid snapping; (x): without grid snapping

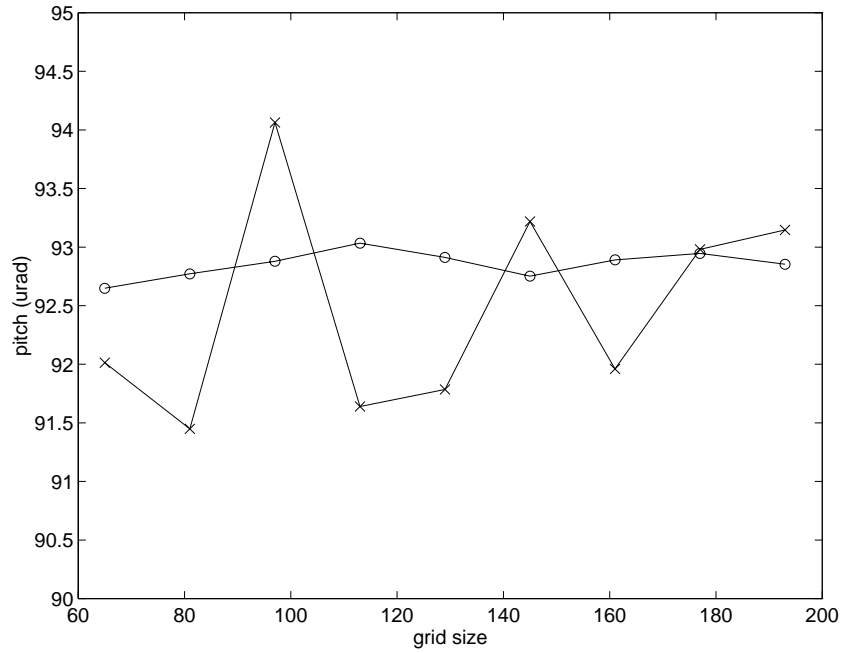


Fig. 3.7 Convergence of Tri-rail pitch with grid size. (o): with grid snapping; (x): without grid snapping

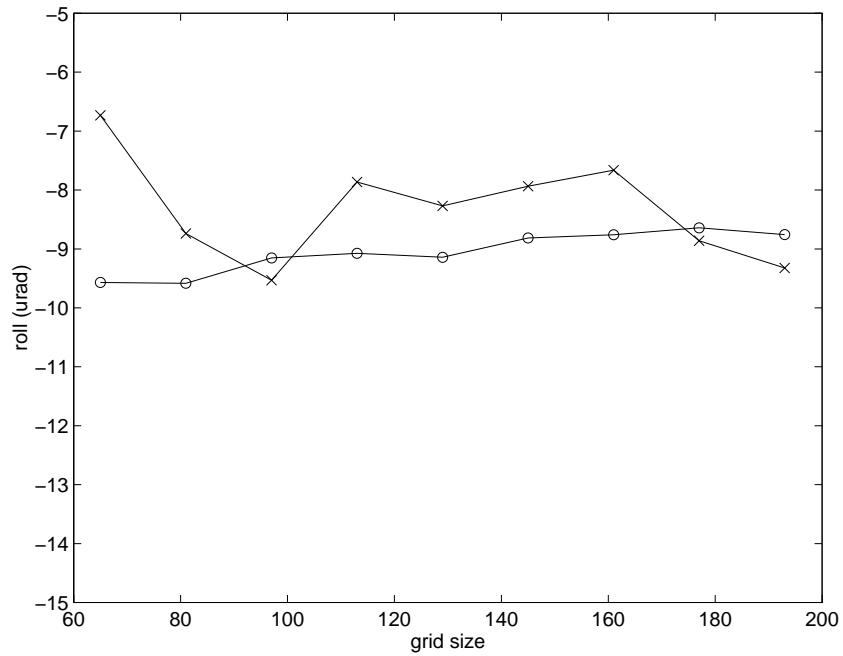


Fig. 3.8 Convergence of Tri-rail roll with grid size. (o): with grid snapping; (x): without grid snapping

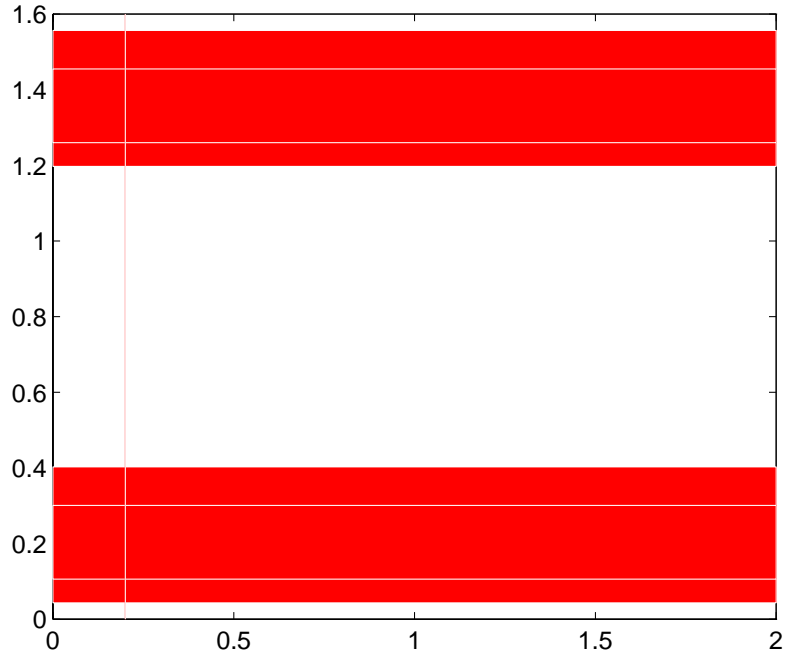


Fig. 3.9 Rail shape of the TPC slider.

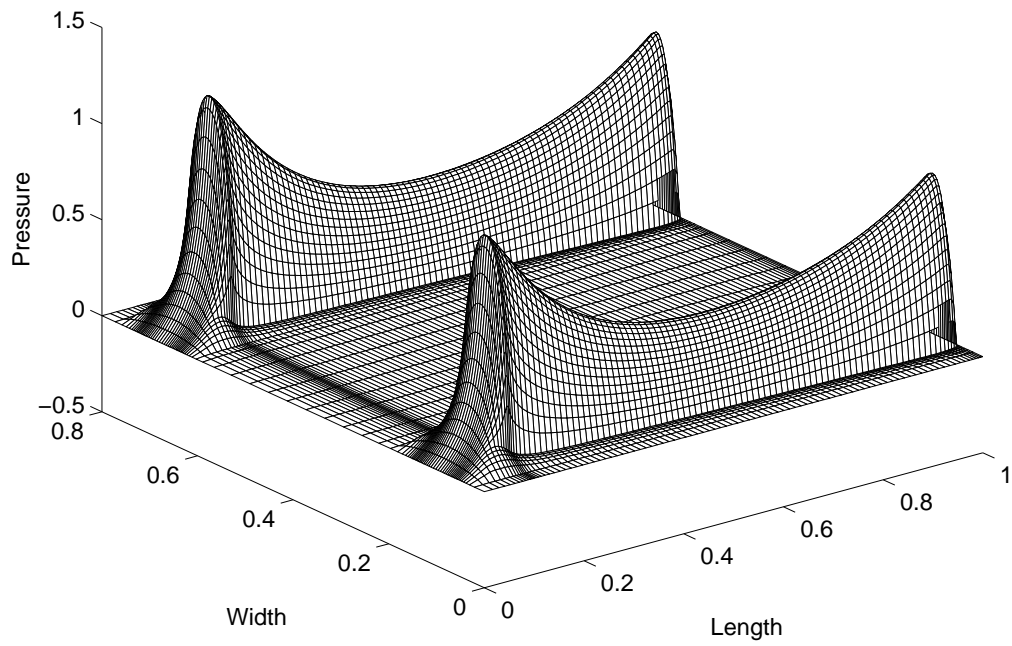


Fig. 3.10 3-D pressure profile of the TPC slider.

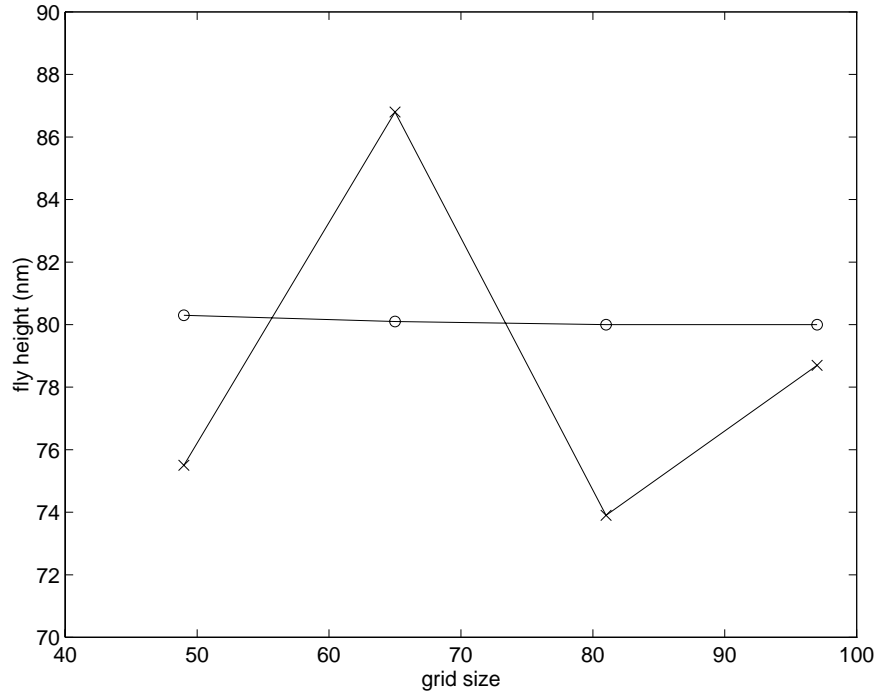


Fig. 3.11 Convergence of TPC fly height with grid size. (o): with grid snapping; (x): without grid snapping

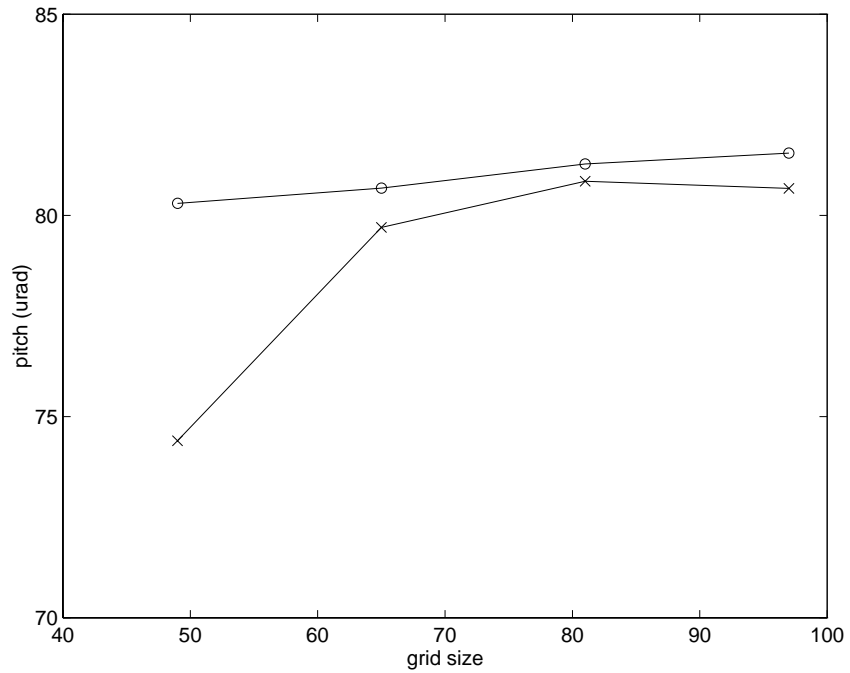


Fig. 3.12 Convergence of TPC pitch with grid size. (o): with grid snapping; (x): without grid snapping

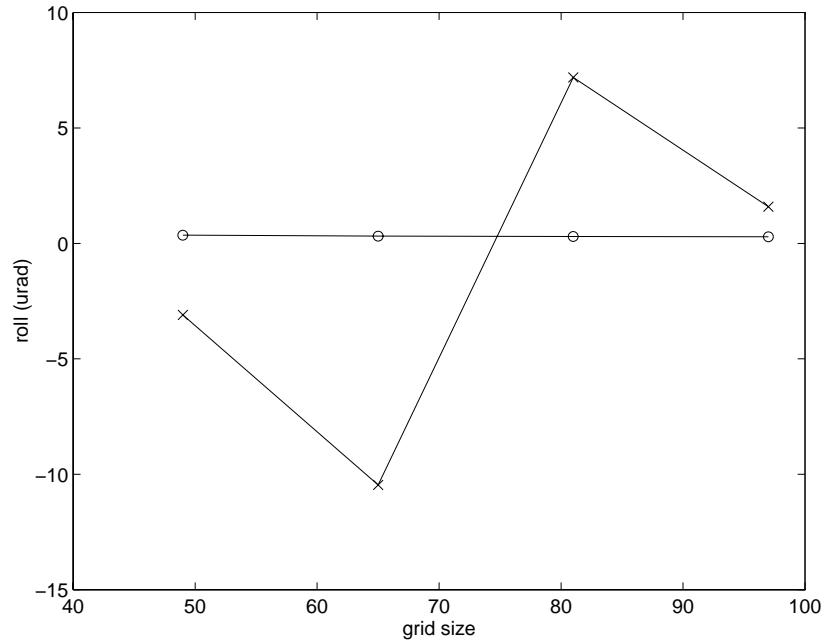


Fig. 3.13 Convergence of TPC roll with grid size. (o): with grid snapping; (x): without grid snapping

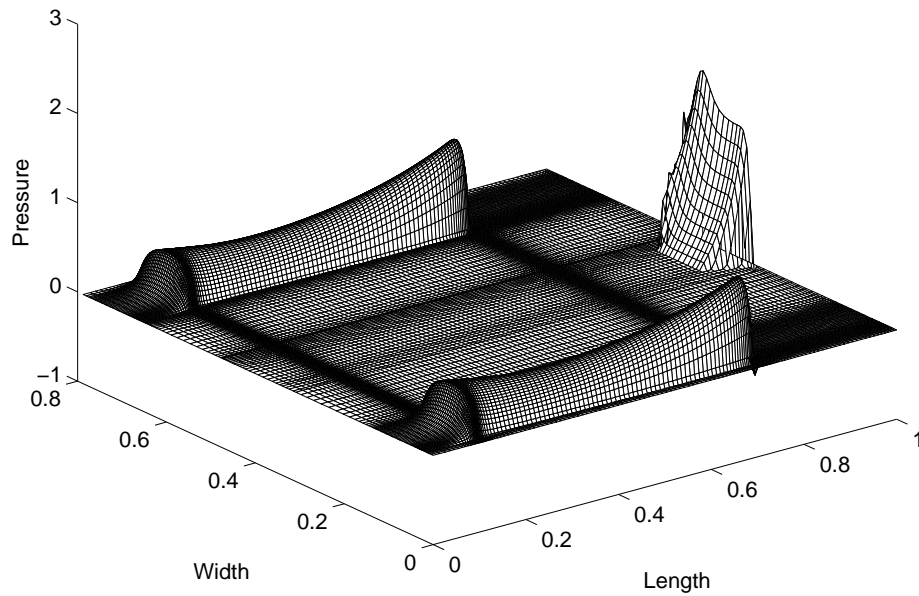


Fig. 3.14 3-D pressure profile for the Tripad slider. Radius = 31 mm, skew = 17.4°, ipmax = 0, difmax = 40, decayfactor = 40

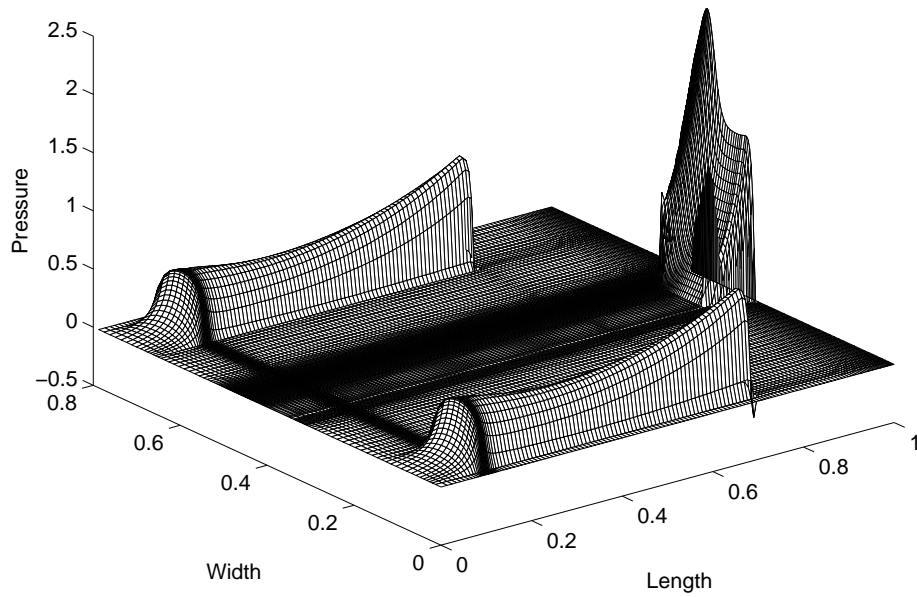


Fig. 3.15 3-D pressure profile for the Tripad slider. Radius = 31 mm, skew = 17.4° ,
 ipmax = 1, difmax = 40, decayfactor = 40

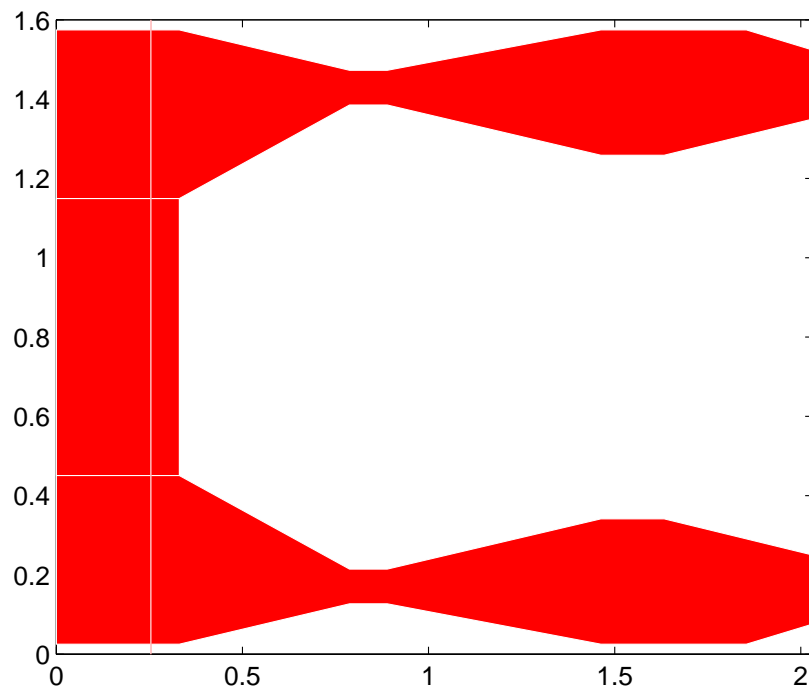


Fig. 3.16 Rail shape of the Seagate AAB slider

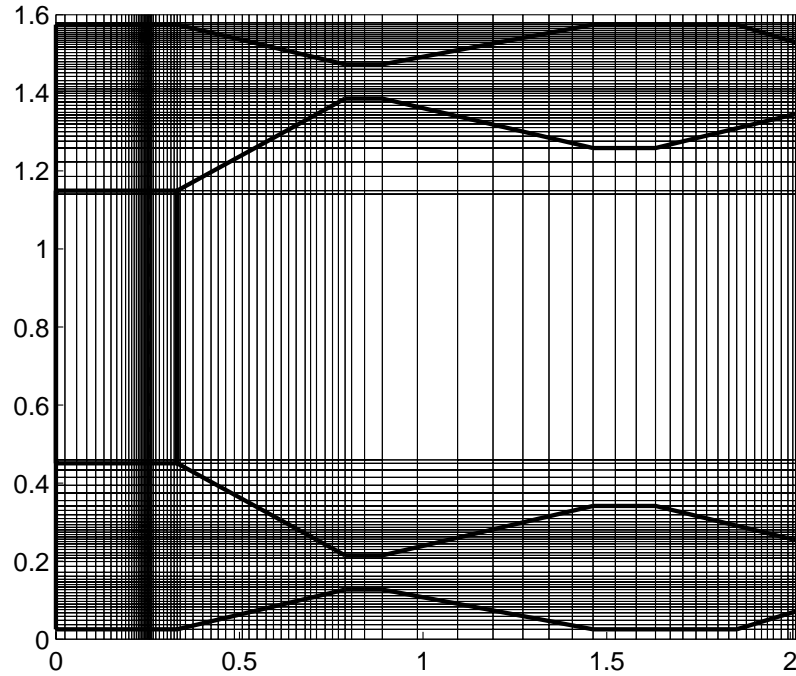


Fig. 3.17 Grid distribution for the AAB slider. $I_{pmax} = 0$, no smoothing and gradient limit

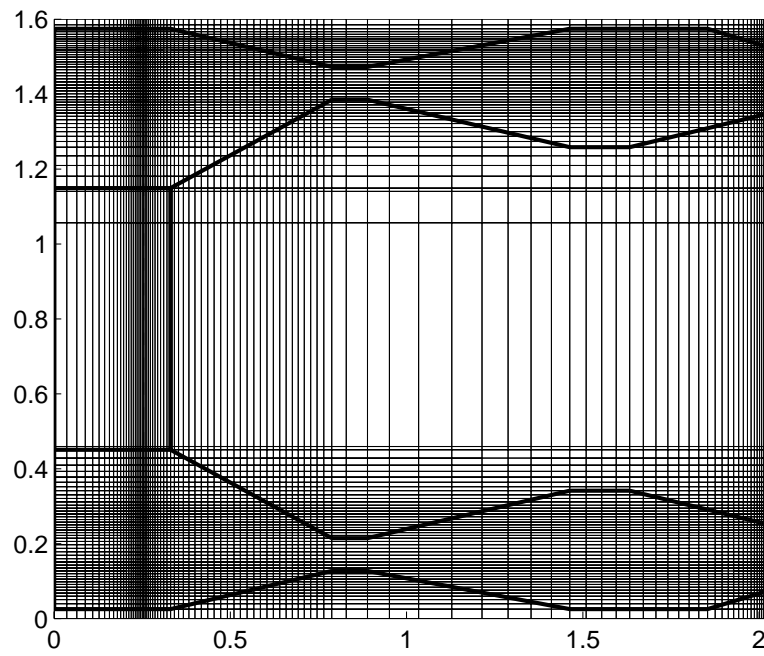


Fig. 3.18 Grid distribution for the AAB slider. $I_{pmax} = 0$, decayfactor = 60, no gradient limit

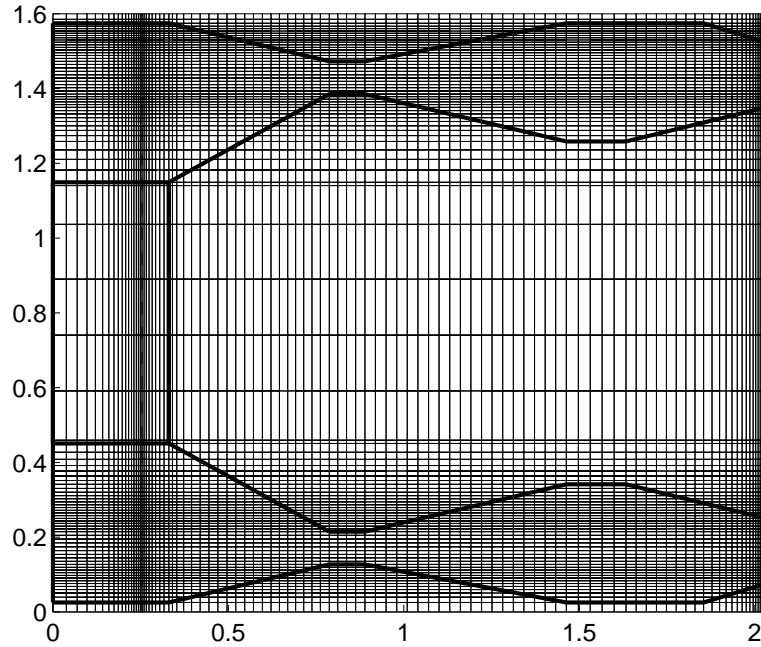


Fig. 3.19 Grid distribution for the AAB slider. $I_{pmax} = 0$, $decayfactor = 60$, $difmax = 30$

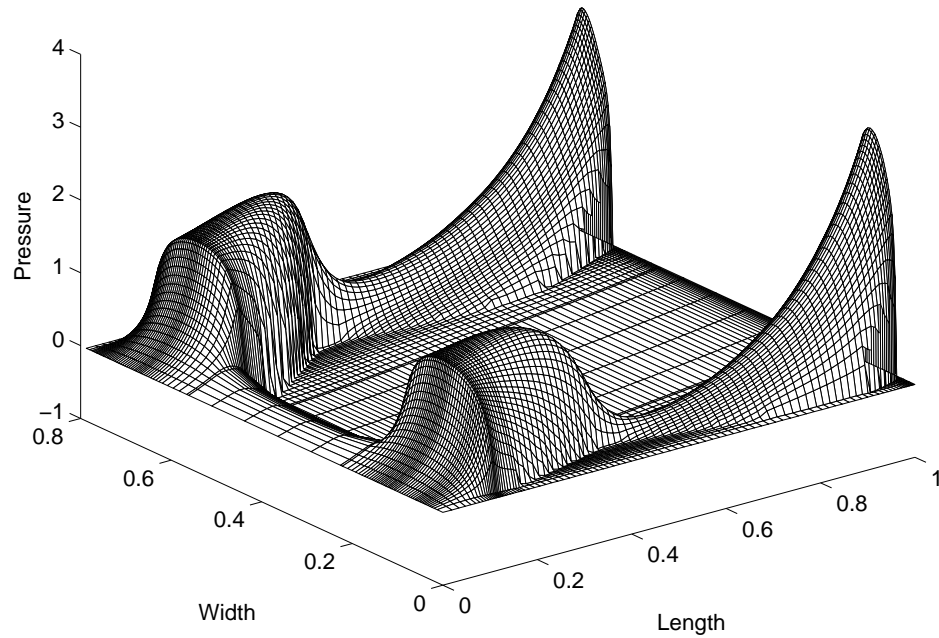


Fig. 3.20 3-D pressure profile of the AAB slider

CHAPTER 4

A MULTI GRID SOLVER FOR THE GENERALIZED REYNOLDS EQUATION

4.1 Introduction

The discretized Reynolds equation can be solved iteratively using the line by line method described in Chapter 2. However, it is observed that the convergence of the solution slows down as the iteration process continues. The process of obtaining the final solution iteratively from an initial guess is called “smoothing”. Brandt (1977) demonstrated that only those error components with wavelength comparable to the mesh size are smoothed efficiently, and that error components with longer wavelengths are smoothed at progressively slower rates.

The multi-grid technique, originally developed for the efficient solution of elliptic partial differential equations (Brandt, 1977), has been gaining popularity, especially in the field of computational fluid dynamics and heat transfer. In the field of lubrication, it has been used to solve EHD lubrication problems (for example, Lubrecht, 1987 and Osborn *et al.*, 1992). The multi-grid method recognizes the fact that the long wavelength (smooth) error components on a fine grid are shorter relative to the mesh size when seen from a coarser grid. Thus, they can be smoothed more efficiently if the solution is moved to a coarser grid. By moving the solution back and forth between a set of different grid levels, both long and short wave length error components can be smoothed efficiently.

A multi-grid method based on the one proposed by Shyy and Sun (1992) has been implemented. The full approximation storage used in this formulation deals more efficiently with the nonlinearity of the equation than the simpler correction storage method. The efficiency of the multi-grid method is optimum compared to single grid iterative methods in the sense that the computation effort is linearly proportional to the number of degrees of freedom. The multi-grid method becomes even more superior when the system of equations becomes larger.

4.2 Numerical Method

Using the control volume method described in Chapter 2, we obtain the following discretized system of equations:

$$a_P P_P = a_E P_E + a_W P_W + a_N P_N + a_S P_S + b \quad (4.1)$$

Eq.(4.1) can be expressed in the matrix form:

$$[A]\langle P \rangle = \langle b \rangle \quad (4.2)$$

where $\langle P \rangle$ is the vector of pressure on all grid points, $[A]$ is the matrix formed by the coefficients a_P , a_E , a_W , a_N and a_S , and $\langle b \rangle$ is the source vector. Due to the nonlinearity of the original equation, the solution of Eq.(4.2) involves two levels of iterations: the inner iteration updates $\langle P \rangle$ for fixed $[A]$ and $\langle b \rangle$, while the outer iteration updates $[A]$ and $\langle b \rangle$ using the most recent $\langle P \rangle$.

4.2.1 Full Approximation Storage (FAS) Scheme

The current implementation of the multi grid method is based on the FMG-FAS (full multi grid – full approximation storage) method used by Shyy and Sun (1992). The

computation is carried out on a series of 5 grids, G_k , with the corresponding solution $\langle P_k \rangle$, where $k = 1, 2, 3, 4, 5$, with $k = 5$ representing the finest mesh. The grid lines of G_k correspond to the odd grid lines of G_{k+1} , where $k = 1, 2, 3, 4$. The solution for $\langle P_k \rangle$ on grid G_k satisfies the equation

$$[A_k] \langle P_k \rangle = \langle b_k \rangle \quad (4.3)$$

where $[A_k]$ and $\langle b_k \rangle$ are the coefficient matrix and the source vector derived directly from the discretization procedure on the appropriate grid level. Therefore, at convergence, $[A_k]$ and $\langle b_k \rangle$ are based on the final solutions of $\langle P_k \rangle$ on grid G_k . During the iteration procedure, they are estimated based on the most current values of $\langle P_k \rangle$. We use a top bar to denote the intermediate variables. Unless the approximate solution $\langle \bar{P}_k \rangle$ satisfies Eq. (4.3), there will be a residual $\langle R_k \rangle$, given by

$$[\bar{A}_k] \langle \bar{P}_k \rangle = \langle \bar{b}_k \rangle - \langle R_k \rangle \quad (4.4)$$

Combining Eq.(4.3) and Eq.(4.4), we can write the fine grid residual equation as

$$[A_k] \langle \bar{P}_k + \delta P_k \rangle - [\bar{A}_k] \langle \bar{P}_k \rangle = \langle b_k \rangle - \langle \bar{b}_k \rangle + \langle R_k \rangle \quad (4.5)$$

where $\delta P_k = P_k - \bar{P}_k$. Eq.(4.5) can be written on the coarse grid by restricting $\langle \bar{P}_k \rangle$ and $\langle R_k \rangle$:

$$[A_{k-1}] \langle I_k^{k-1} \bar{P}_k + \delta P_{k-1} \rangle - [\bar{A}_{k-1}] \langle I_k^{k-1} \bar{P}_k \rangle = \langle b_{k-1} \rangle - \langle \bar{b}_{k-1} \rangle + \langle I_k^{k-1} R_k \rangle \quad (4.6)$$

where I_k^{k-1} is the restriction operator that transmits the information from a fine grid to a coarse grid. In the current implementation, the “direct injection” method is used which assigns the value on the fine grid directly to the corresponding coarse grid point.

Putting the known quantities in Eq.(4.6) to the right hand side, we can reduce Eq.(4.6) to

$$[A_{k-1}] \langle \hat{P}_{k-1} \rangle = \langle \hat{b}_{k-1} \rangle \quad (4.7)$$

where
$$\hat{P}_{k-1} = I_k^{k-1} \bar{P}_k + \delta P_{k-1} \quad (4.8)$$

and
$$\langle \hat{b}_{k-1} \rangle = \langle b_{k-1} \rangle + [A_{k-1}] \langle I_k^{k-1} \bar{P}_k \rangle - \langle \bar{b}_{k-1} \rangle + \langle I_k^{k-1} R_k \rangle \quad (4.9)$$

$[A_{k-1}]$ and $\langle \hat{b}_{k-1} \rangle$ are updated in the outer iteration using the most recent value of \hat{P}_{k-1} .

Note that in Eq.(4.9), only $\langle b_{k-1} \rangle$ need be updated. The rest of the right hand side is only computed once at the beginning of the coarse grid iteration.

This scheme is called the full approximate storage scheme because the complete solution $\langle \hat{P}_{k-1} \rangle$, not just the correction δP_{k-1} , is computed. After Eq.(4.7) is solved, the correction δP_{k-1} is obtained first via Eq.(4.8), and the fine grid solution is updated using the equation

$$\bar{P}_k^{new} = \bar{P}_k + I_{k-1}^k \delta P_{k-1} \quad (4.10)$$

where I_{k-1}^k is the prolongation (interpolation) operator. A simple bilinear interpolation is used in the current implementation, which can be expressed as

$$P_{2i,2j}^k = P_{i,j}^{k-1}, \quad (4.11a)$$

$$P_{2i+1,2j}^k = \frac{1}{2} (P_{i,j}^{k-1} + P_{i+1,j}^{k-1}), \quad (4.11b)$$

$$P_{2i,2j+1}^k = \frac{1}{2}(P_{i,j}^{k-1} + P_{i,j+1}^{k-1}) \quad (4.11c)$$

and

$$P_{2i+1,2j+1}^k = \frac{1}{4}(P_{i,j}^{k-1} + P_{i+1,j}^{k-1} + P_{i,j+1}^{k-1} + P_{i+1,j+1}^{k-1}) \quad (4.11d)$$

where the superscripts denote the grid level and the subscripts are the grid indices. For non-uniform grids, the weighting coefficients could be adjusted to reflect the grid variation. However, the Eq.(4.11) is used in the current implementation.

4.2.2 Full Multi Grid Algorithm

The procedure of the multi grid cycling is illustrated in Fig. 4.1, after Shyy and Sun (1992), with slight difference in the number of iterations at each level. In a V-cycle at each grid level, the solver performs a few iterations on the fine grid, then the residual is restricted (injected) to the next coarser grid to form the equation on that grid. A few iterations are then performed on that grid. The same procedure goes on to the coarsest grid. After a number of iterations on the coarse grid, the solution correction is prolonged (interpolated) back to the next finer grid. A small number of iterations is performed and then the solution is again prolonged to the next finer grid until the finest grid on that level is reached. This completes the V-cycle. The numbers of iterations indicated in Fig. 4.1 are the upper limits. Fewer iterations may actually be performed if convergence is reached.

A good initial approximation may reduce the number of iterations required to reach convergence. To get a better initial guess, it is helpful to interpolate the solution on a coarse grid to the fine grid. In the full multi grid strategy, the solution is first obtained on the coarsest level and then interpolated to the next grid. The V-cycle is performed on that level until convergence is obtained. Then the solution is interpolated to the next finer

grid and the V-cycle is again performed. The final solution is obtained when the V-cycle converges on the finest grid.

4.3 Results and Discussions

As an example, the Tri-rail slider (Chapter 3) is used to illustrate the multi grid configuration. Fig. 4.2 - Fig. 4.5 illustrate four successively finer levels of grid (the coarsest grid not shown) used in the computation. The 3-D pressure profiles are plotted in Fig. 4.6 – Fig. 4.9 for each grid, respectively.

It has been observed that a savings of more than one order of magnitude in computation time can be achieved with the typical grid size used in air bearing simulations. The multi grid method becomes even more superior when a larger grid size is used.

4.4 Summary

A full multi grid – full approximation storage method is implemented which deals with the nonlinearity of the equation effectively. Computational efficiency is improved dramatically.

Full Multigrid (FMG) V-cycle

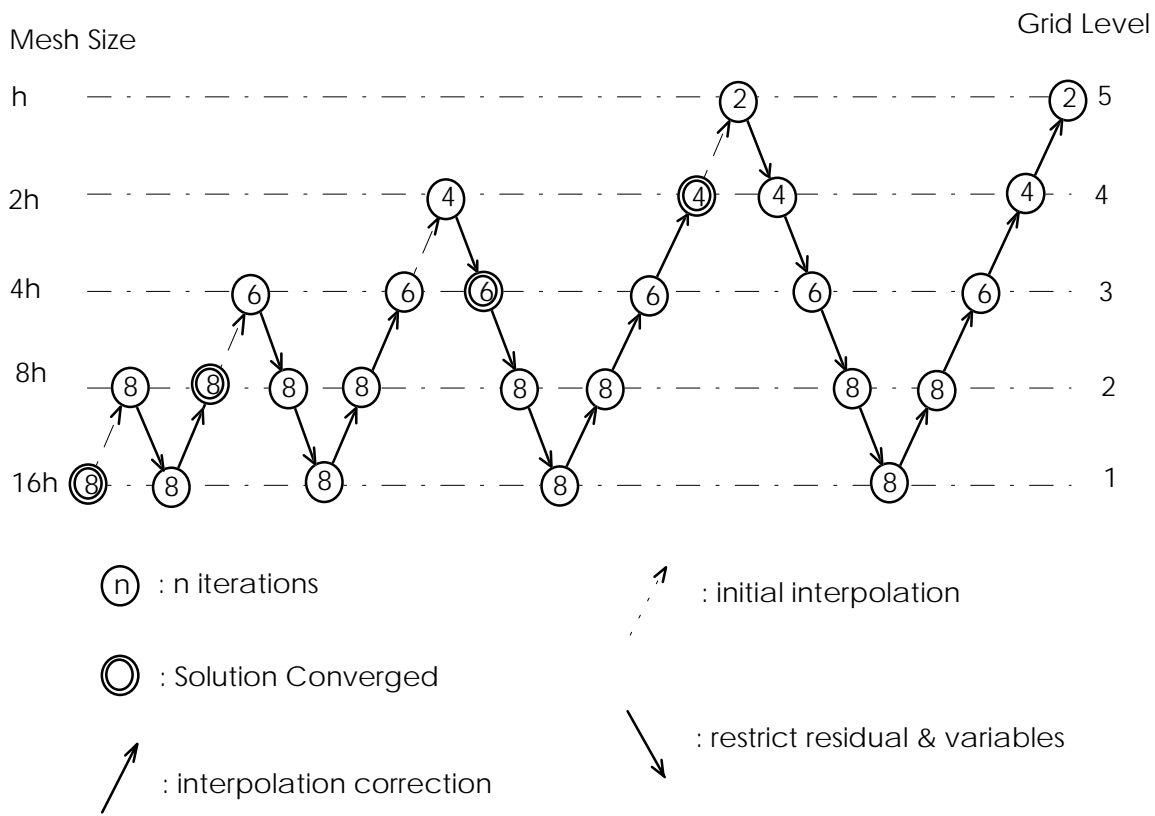


Fig. 4.1 The full multi grid procedure (after Shyy and Sun, 1992)

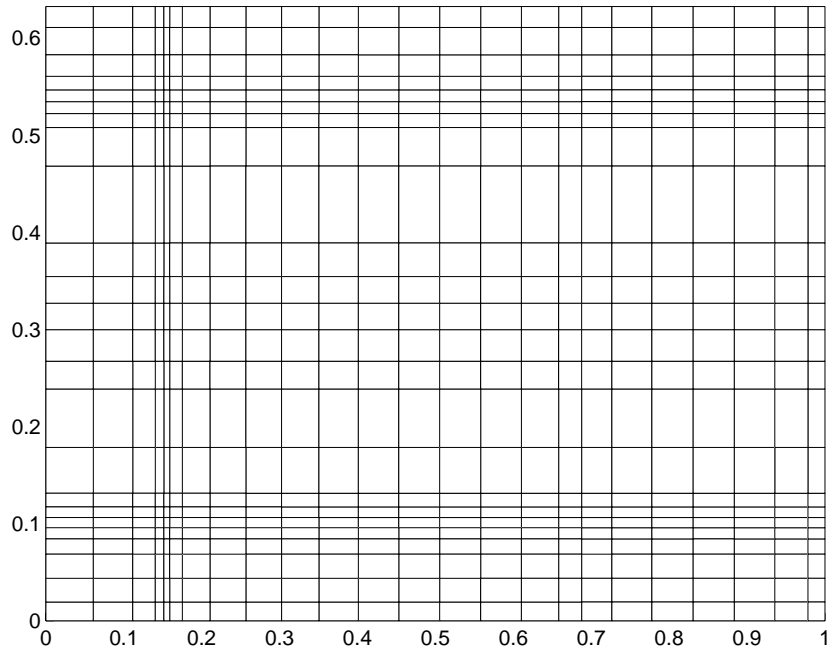


Fig. 4.2 Multi grid for the Tri-rail slider, grid level 2: 25 x 25

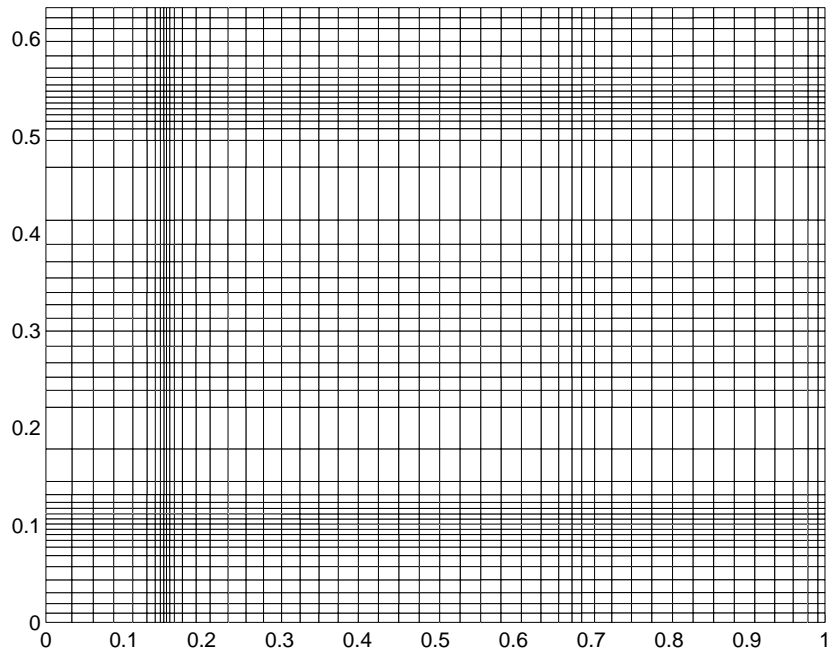


Fig. 4.3 Multi grid for the Tri-rail slider, grid level 3: 49 x 49

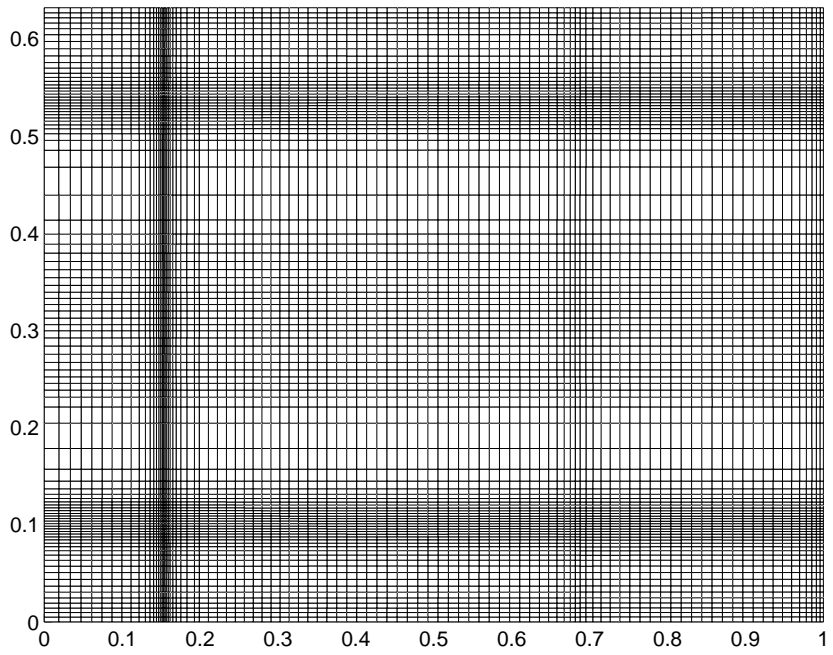


Fig. 4.4 Multi grid for the Tri-rail slider, grid level 4: 97 x 97

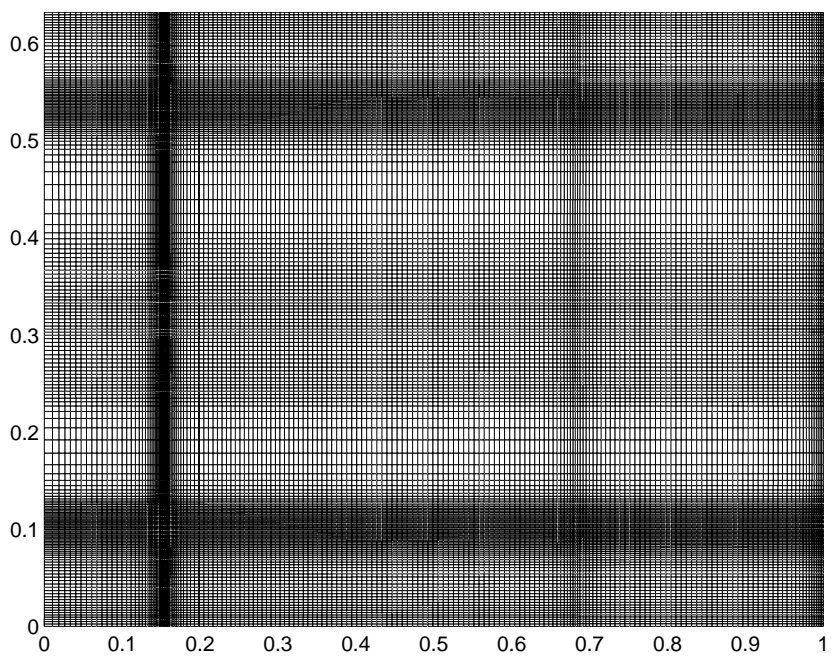


Fig. 4.5 Multi grid for the Tri-rail slider, grid level 5: 193 x 193

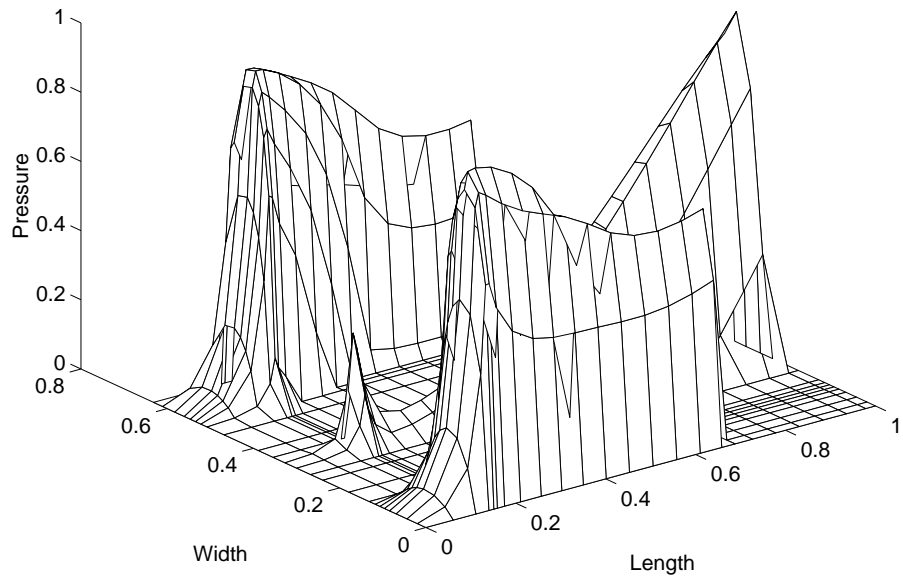


Fig. 4.6 3-D pressure profile for the Tri-rail slider, grid level 2: 25 x 25

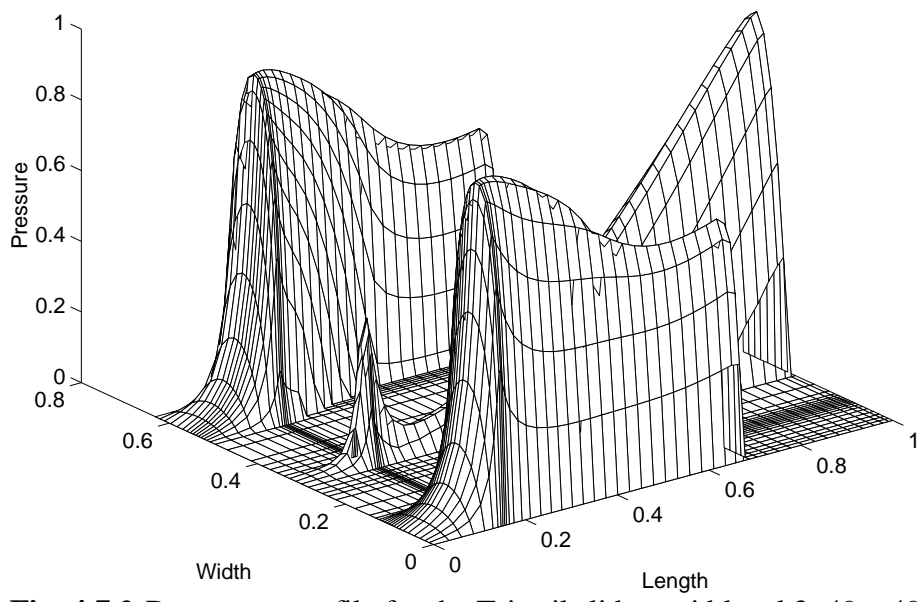


Fig. 4.7 3-D pressure profile for the Tri-rail slider, grid level 3: 49 x 49

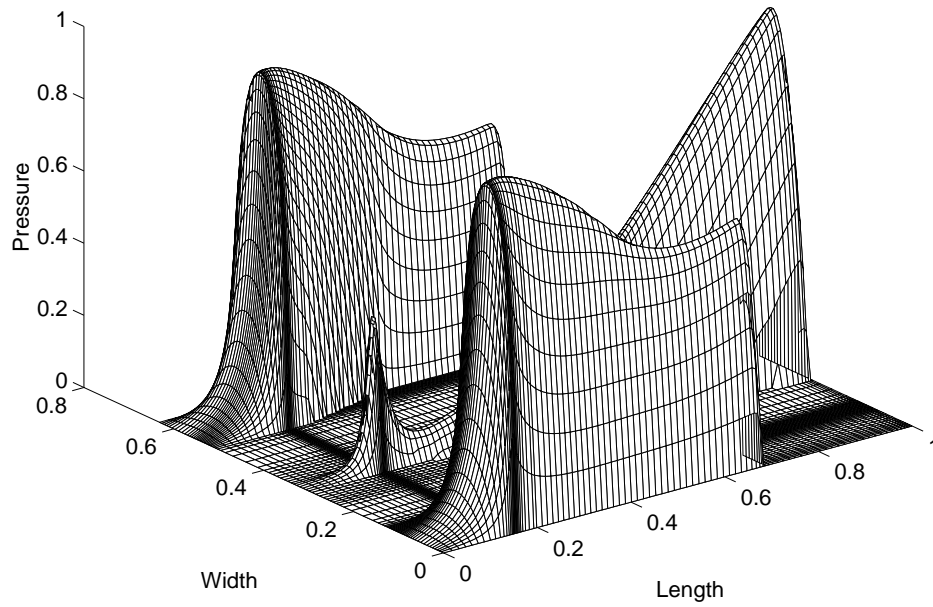


Fig. 4.8 3-D pressure profile for the Tri-rail slider, grid level 4: 97 x 97

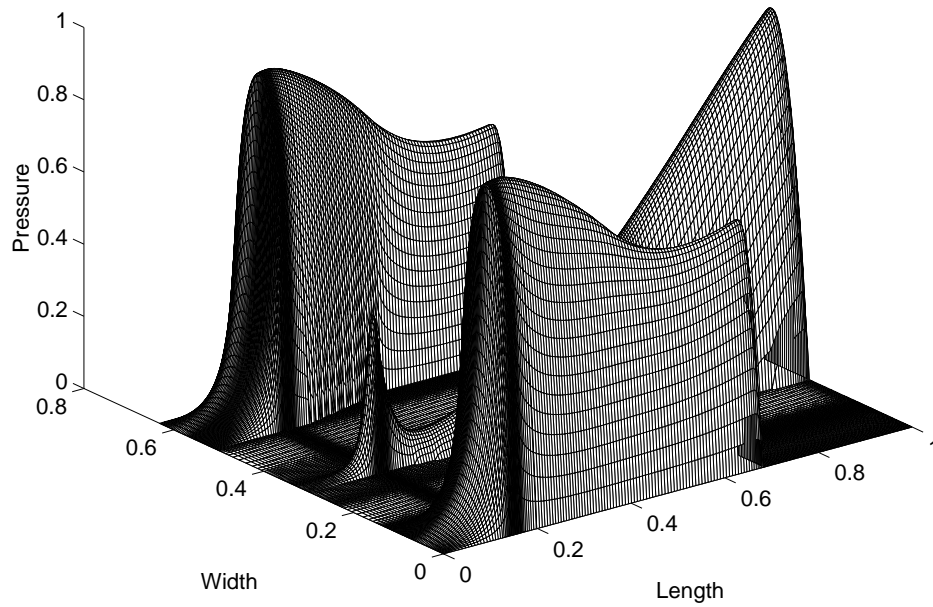


Fig. 4.9 3-D pressure profile for the Tri-rail slider, grid level 5: 193 x 193

CHAPTER 5

COMPARISON OF CONVECTION SCHEMES

5.1 Introduction

A control volume formulation of the generalized Reynolds equation has been detailed in Chapter 2. In high speed gas lubricated bearings, a simplistic treatment of the convective term using central difference often leads to numerical instability. In order to make a sound choice among different alternatives, a comparative study is carried out in this chapter. The convective schemes used are: modified central difference, upwind, hybrid, power-law and QUICK. It is concluded that the hybrid scheme is superior in terms of stability, accuracy and computational efficiency.

5.2 Numerical Method

The control volume method discussed in Chapter 2 is used to discretized the generalized Reynolds equation. The resulting system of linear equations has the following form:

$$a_P P_P = a_E P_E + a_W P_W + a_N P_N + a_S P_S + b \quad (5.1)$$

where

$$a_E = D_e A(|P_e|) + \max(-F_e, 0) \quad (5.2a)$$

$$a_W = D_w A(|P_w|) + \max(F_w, 0) \quad (5.2b)$$

$$a_N = D_n A(|P_n|) + \max(-F_n, 0) \quad (5.2c)$$

$$a_s = D_s A(|P_s|) + \max(F_s, 0) \quad (5.2d)$$

$$a_p = a_E + a_w + a_N + a_s + \max(0, F_e - F_w + F_n - F_s) \quad (5.2e)$$

$$b = \max(0, F_w - F_e + F_s - F_n) P_p \quad (5.2f)$$

where the dependent variable in Eq.(5.2f) is assumed to be known using the most current value; the function $A(|P|)$ depends on the convective scheme chosen, according to

$1 - 0.5 P $	central difference
1	upwind
$\max(0, 1 - 0.5 P)$	hybrid
$\max(0, (1 - 0.1 P)^5)$	power-law
$ P / (e^{ P } - 1)$	exponential

The stability of the central difference scheme can be enhanced by casting $A(|P|)$ into the form of the hybrid scheme and putting the difference into the source term. This is the implementation used in this study.

The exponential scheme is rarely used in practice because exponentials are expensive to compute and it is based on the exact solution only for steady one dimensional linear problems without the source term, therefore it is not necessarily accurate for more general problems and is not included in this study.

The QUICK scheme originally devised by Leonard (1979) employs a three-point upstream-weighted quadratic interpolation method to evaluate the dependent variable at the control volume faces, therefore it has a higher order of formal accuracy than the central difference scheme. Hayase *et al.* (1992) proposed a formulation of QUICK through rearrangement of the source term, which has better convergence performance

than other QUICK schemes. This formulation of QUICK is also investigated in the current study.

5.3 Results and Discussions

Two slider designs are used in this study, a simple straight rail TPC slider and a negative pressure slider (Nutcracker) with shaped rails. The rail shapes are plotted in Fig. 5.1 and Fig. 5.2, respectively. The TPC slider is held at fixed attitude with fly height, pitch and roll set at 75 nm, 93.75 μ rad and 0 μ rad, respectively. The air bearing pressure is solved for using each of the convective schemes on four sets of grids of size 49 x 49, 97 x 97, 193 x 193 and 385 x 385. The fly height, pitch and roll for the Nutcracker slider is 25 nm, 131.7 μ rad and 0 μ rad respectively. The pressure is obtained for grid sizes 97 x 97, 193 x 193, 289 x 289 and 385 x 385. The convergence of peak pressure and bearing load with grid size are monitored.

5.3.1 Results for the TPC Slider

All of the cases for the TPC slider converged without a problem. However, when the central difference scheme is used, a pressure spike at the trailing edge of the slider appears if there is not enough grid resolution (Fig. 5.3). The spike disappears when more grid lines are concentrated at the trailing edge. It also takes significantly more iterations for the central difference scheme to converge.

The peak pressures for different grid sizes using each of the convective schemes are plotted in Fig. 5.4. It is interesting to note that the maximum pressure for both the central difference and the hybrid scheme are the same for all grid sizes and they reach the asymptotic value the fastest. The peak pressure converges at a slower rate for the

QUICK and power-law schemes. All four schemes reach the same peak pressure at the maximum grid size of 385 x 385. The grid convergence rate of the upwind scheme is much slower than the other schemes. The numerical diffusion introduced by the upwind scheme reduces the peak pressure.

Fig. 5.5 demonstrates the convergence of the bearing load for the different schemes. It can be seen that the bearing load converges to the asymptotic value from above for the hybrid scheme while it converges from below for the central difference scheme, despite the fact that the peak pressures are the same for the two schemes. The bearing loads for the two schemes reach the same value at the maximum grid size, while it is still slightly different for the power-law and the QUICK scheme. This implies that the power-law and QUICK schemes have slightly slower convergence rates.

5.3.2 Results for the Nutcracker Slider

The solution fails to converge for the central difference scheme starting from a uniform grid. When the adaptive grid generated by the power-law scheme is used, the solution does converge, though much slower than for other schemes. The pressure spike along the trailing edge is also observed on the 97 x 97 grid (Fig. 5.6). The pressure distribution obtained from the QUICK scheme on a 97 x 97 grid also has pressure spikes along the trailing edge, as can be seen in Fig. 5.7. This is caused by the quadratic interpolation at places with sharp gradient changes.

The maximum pressure plotted in Fig. 5.8 indicates that the central difference scheme renders a high peak pressure on the 97 x 97 grid. This is due to the pressure spike along the trailing edge. The peak pressure for the hybrid scheme almost reaches the asymptotic value at grid size 197 x 197, while the peak pressure for the central difference

scheme joins that of hybrid scheme at grid size 289×289 . Unlike the TPC slider case, however, the peak pressures for the power-law and QUICK schemes still have not reached the asymptotic value at the maximum grid size of 385×385 . The QUICK scheme converges to the asymptotic value slightly faster than the power-law scheme. The worst performer again is the upwind scheme.

Fig 5.9 shows that the asymptotic convergence of the bearing load is slower than the peak pressure. None of the schemes fully reaches the final value at the maximum grid size of 385×385 . The central difference scheme converges to the asymptotic value the fastest. It is joined by the hybrid scheme at finer grid size. The QUICK and power-law schemes have slightly slower convergence rates. Lagging far behind is the upwind scheme.

5.4 Summary

An comparative study of convective schemes shows that the central difference scheme is unstable for high bearing numbers and shaped rails without a properly distributed grid. However, when it converges, the central difference scheme exhibits the fastest asymptotic behavior. On larger grids, the hybrid scheme gives essentially the same result as the central difference scheme, because the hybrid scheme recovers the central difference form for small Peclet numbers. The upwind scheme consistently yields lower pressure peaks and therefore load carrying capacity, because it has the lowest order of accuracy among all schemes. The high accuracy of the quadratic interpolation of the QUICK scheme is decimated by the geometric discontinuities in the air bearing and the

sharp pressure drop at the trailing edge. The grid convergence rates for the QUICK and the power-law schemes are about the same.

In terms of computational efficiency measured by CPU time needed to obtain a pressure solution on a given grid, the upwind scheme is the fastest due to its extremely simple form, followed by the hybrid scheme and the power-law scheme. The QUICK scheme is more CPU and memory intensive because of its complicated interpolation coefficients for non-uniform grids. The central difference scheme takes the longest time to converge due to its stability limitations.

Overall, the hybrid scheme combines excellent stability, fast grid convergence and high computational efficiency. It is the scheme of choice for air bearing simulations.

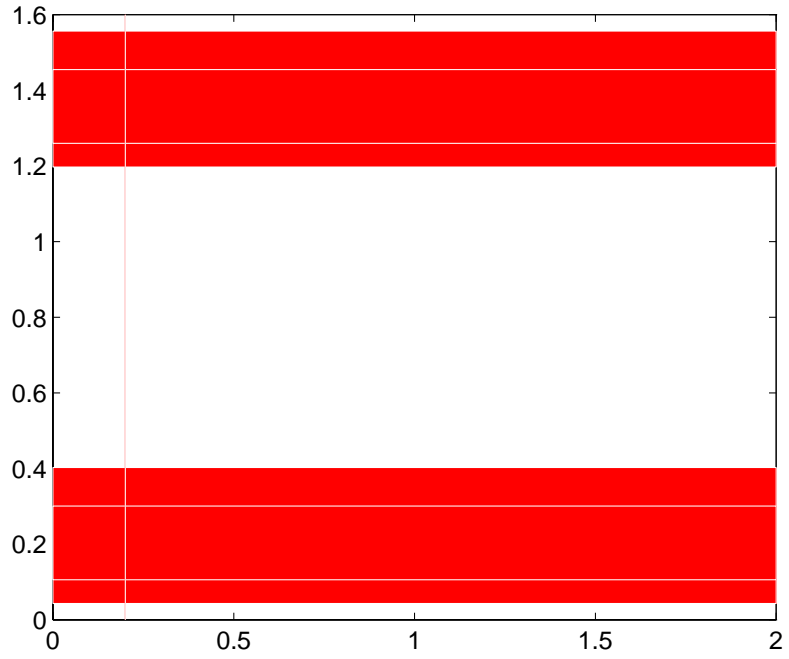


Fig. 5.1 Rail shape of the TPC slider

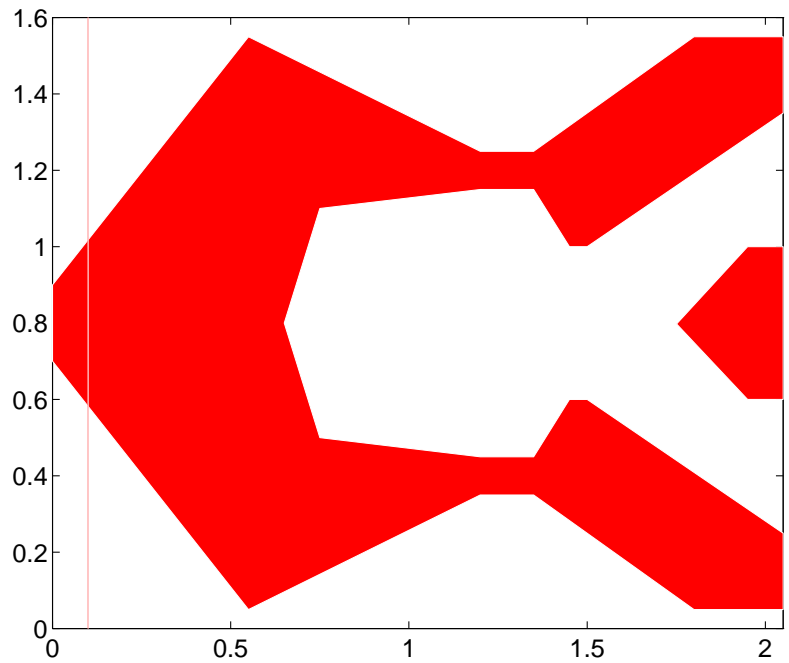


Fig. 5.2 Rail shape of the Nutcracker slider

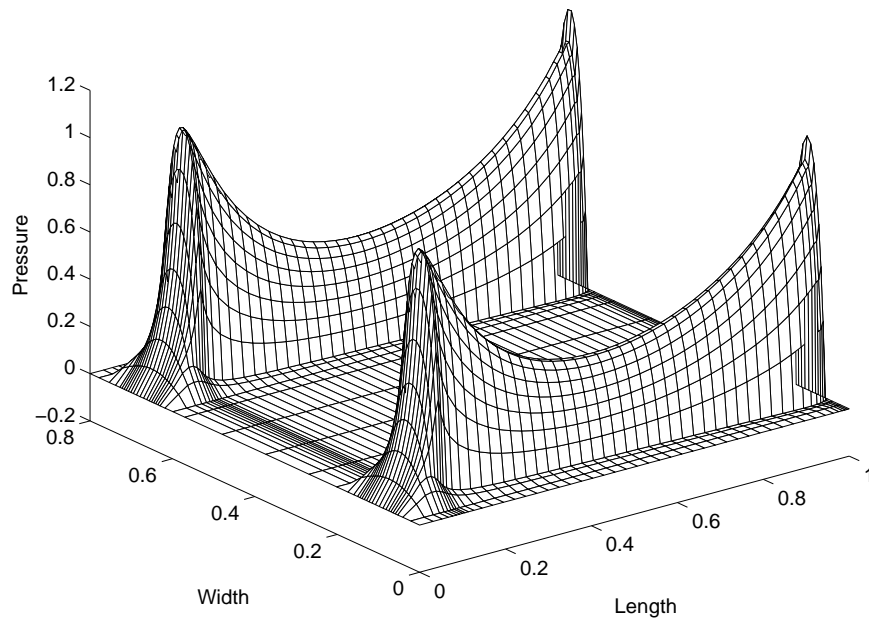


Fig. 5.3 3-D pressure profile of the TPC slider using central difference scheme on a 49 x 49 grid

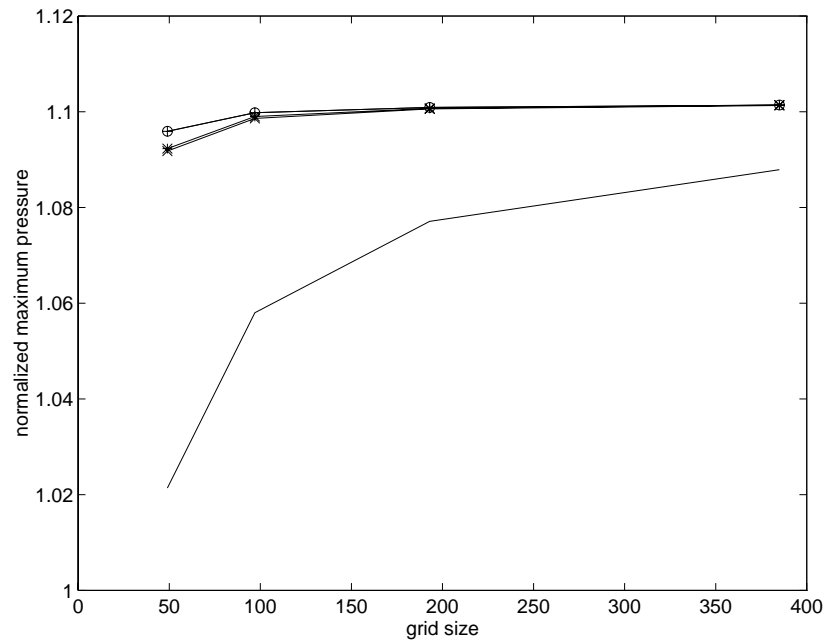


Fig. 5.4 Convergence of normalized peak pressure with grid size for TPC slider using different convective schemes. (o): central difference; (x): power-law; (*): QUICK; (+): hybrid; solid line: upwind

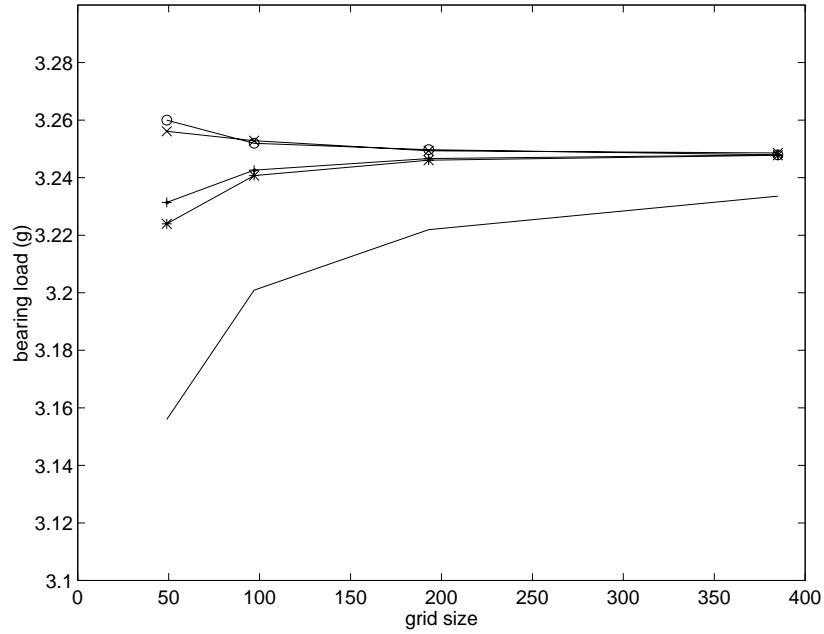


Fig. 5.5 Convergence of bearing load with grid size for TPC slider using different convective schemes. (o): central difference; (x): power-law; (*): QUICK; (+): hybrid; solid line: upwind

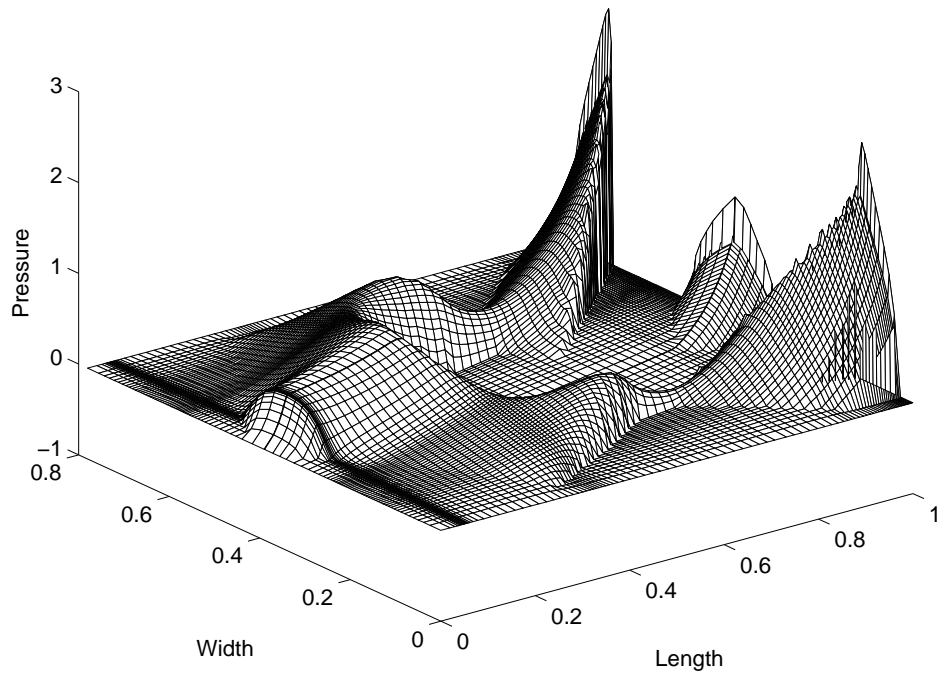


Fig. 5.6 3-D pressure profile of the Nutcracker slider using central difference scheme on a 97 x 97 grid

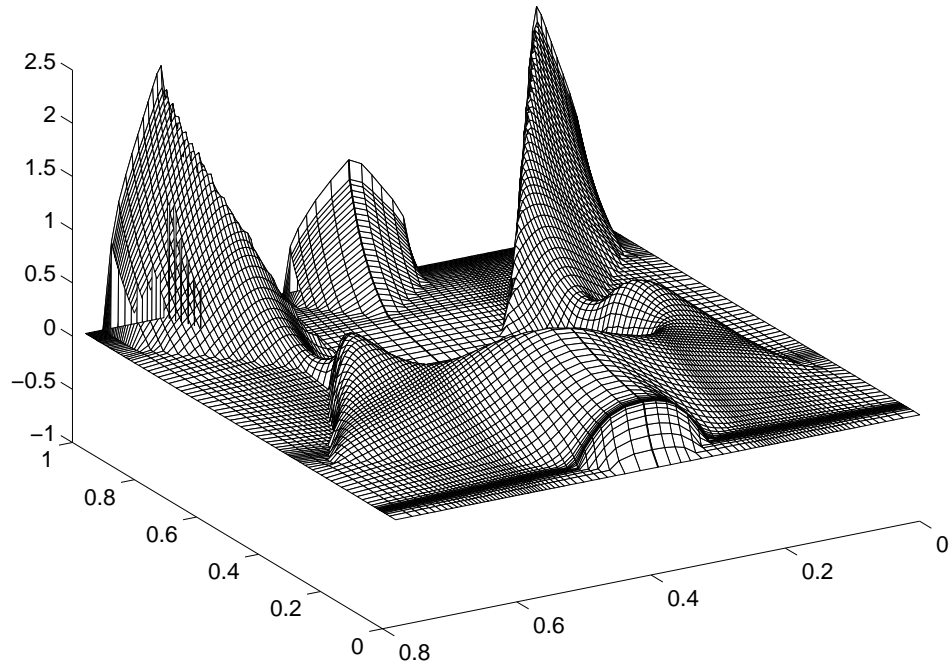


Fig. 5.7 3-D pressure profile of the Nutcracker slider using the QUICK scheme on a 97 x 97 grid

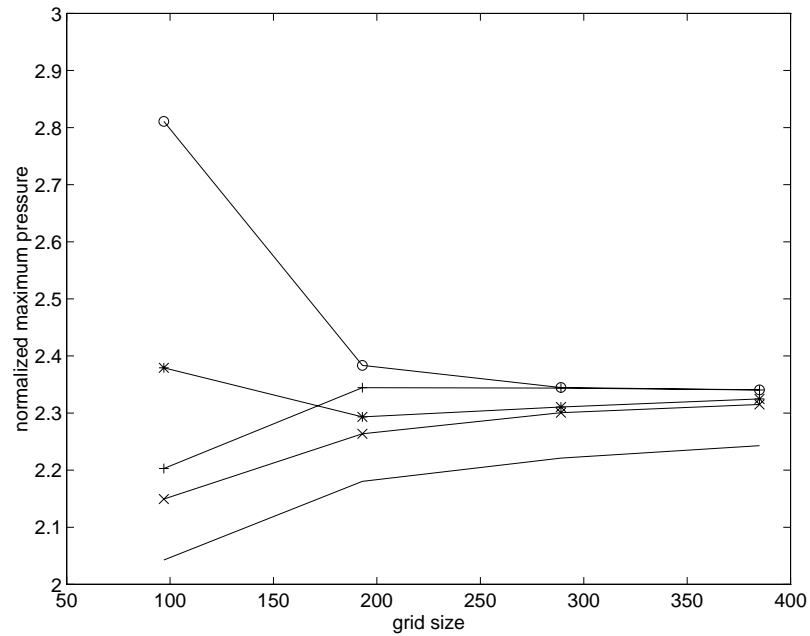


Fig. 5.8 Convergence of normalized peak pressure with grid size for the Nutcracker slider using different convective schemes. (o): central difference; (x): power-law; (*): QUICK; (+): hybrid; solid line: upwind

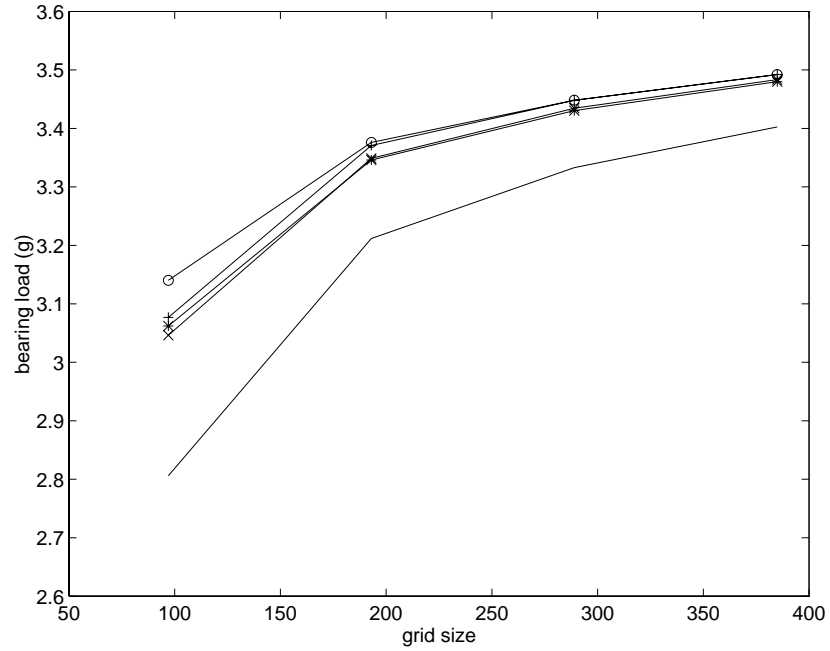


Fig. 5.9 Convergence of bearing load with grid size for the Nutcracker slider using different convective schemes. (o): central difference; (x): power-law; (*): QUICK; (+): hybrid; solid line: upwind

CHAPTER 6

SOME SUB-25 NM NEGATIVE PRESSURE SLIDER DESIGNS¹

6.1 Introduction

In the near future magnetic hard disk drives are expected to achieve densities approaching 10 gigabits per square inch. This will require magnetic spacing between the read/write transducer and magnetic disk of less than 25 nm. Such spacings are being referred to in the industry as “near contact”. In these designs, negative pressure (sub-ambient pressure) sliders are desirable because they can provide a constant fly height profile, have a low take-off speed and high air bearing stiffness. While the fly height has been decreasing, the miniaturization of sliders also continues. The slider size has dropped from 4 mm x 3.2 mm (100%) to the current dominant 50% “nano sliders”, with 30% “pico sliders” appearing in the market. The decrease in size makes the slider more compliant to the disk topography and reduces the damage caused by slider-disk contact.

This Chapter presents several sub 25 nm sliders with shaped rails and sub-ambient pressure zones. The first 50% / 25 nm slider design were fabricated using chemical etch techniques, and their spacings were measured against a glass disk by an interferometer. The measurement system was the Phase Metrics DFHT. It was found that the measured spacings were substantially greater than the design values. However, stylus measurements of the etch profiles indicated slopes different from those

¹ This part of the project is supported by the National Storage Industry Consortium.

incorporated in the simulator. After accounting for these slopes in the simulator input data we found that the subsequently obtained simulation results were in good agreement with measurements. The simulation results for a modified 50% / 25 nm (Nutcracker), a 50% / 15 nm, and a 30% / 15 nm slider are also presented.

6.2 Numerical Models

The generalized Reynolds equation is solved using the CML air bearing design program, detailed in previous chapters. The shaped rail designs are accomplished by use of a mouse, as explained in the graphical interface described in Appendix A.

6.3 Results and Discussions

6.3.1. A 50% Slider Design for 25 nm Spacing

Fig. 6.1 gives the rail outline for the 50%, 25 nm slider. The front region contains a 0.1mm flat taper. The recess at the taper front is 1 micron. The nominal etch depth is 5 microns, and the rails have a crown of 15 nm and a camber of 10 nm. The suspension preload is 3 grams. The recess wall is assumed to be vertical in the simulation. The design goal was a trailing edge fly height that is uniform across the radius of the disk, taking into account the skew that would accompany an in-line suspension with a rotary actuator (-4° at the ID and 18° at the OD) on a 65 mm disk. The rail has concave shapes on both sides to achieve the uniform fly height. The 3 dimensional pressure profile at the ID is illustrated in Fig. 6.2. Fig. 6.3 plots the simulated fly height profile at the center rail trailing edge. It is seen that a uniform flying height is achieved quite well, to within 2 nm. The pitch (Fig. 6.4) varies from $117 \mu\text{rad}$ at the ID to $165 \mu\text{rad}$ at the OD, while the

roll (Fig. 6.5) has a range of 1 μ rad to -19 μ rad. The take-off fly height profile in Fig. 6.6 shows that the slider has fast take-off characteristics typical of negative pressure sliders. The fly height actually peaks at around 4000 rpm and drops slightly at the normal operational speed of 5400 rpm, because the negative pressure develops faster with increase in speed than the positive pressure in this range.

This slider design was fabricated in Read-Rite using chemical etch methods. The sliders were attached to Hutchingson 1950 type suspensions with a preload of 3 grams and their fly heights were measured by the Phase Metrics DFHT. The fly height measuring point was 75 microns from the trailing edge center.

Fig. 6.7 shows the measured mean flying heights (o) of the sliders as a function of radial position. Clearly this flying height is not in agreement with the simulation prediction at the measuring point (x). The measured roll (o) in Fig. 6.8 is also larger in magnitude than the prediction (x).

In order to find out the cause of the difference between measured fly heights and the design nominals, it is essential to obtain the deviation of the actual slider geometry from the design specifications. Therefore details of the ABS geometry of the fabricated sliders were measured. The rail dimensions were obtained by using a Zygo NewView 100, and the etch slope and recess depth were measured by a stylus profilometer with a particularly sharp stylus. It was found that the etch slope was a ramp with about 20 microns displacement at the bottom of the etched region, while in the design, a vertical wall is assumed. The shallow slope was confirmed by the SEM picture provided by Dr. Singh Bhatia of IBM(Fig. 6.9). In addition to the ramp angle mentioned above, this

figure shows that the etched surface has high surface roughness that needs to be incorporated in future simulations.

The simulations were repeated using the measured 20 micron etch ramp, and the results are indicated as the (*) lines in Figs. 6.7 & 6.8 . Here it is seen that fairly good agreement is achieved between the mean measurement of the set of fabricated sliders and the simulation result.

6.3.2. Three Sub-25 nm Spacing Slider Designs

This section presents three more air bearing surface designs, which are all of the sub-ambient pressure type. The 50% / 25 nm (Nutcracker, Fig. 6.10) design has an active center pad that carries the read-write element. The 50 % / 15 nm (Fig. 6.16) and the 30% / 15 nm (Fig. 6.22) designs are both of twin rail type with the read-write element at the outer rail trailing edge. In all three designs, the rail shapes are concave on both sides to minimize the fly height change across the disk by compensating for the change in skew angle. The connected front regions of the ABS enable the efficient generation of sub-ambient pressure in the recessed regions that follow immediately behind. Examples of pressure distribution for the three designs are given in Fig. 6.11, Fig. 6.17 and Fig. 6.23, respectively. All are obtained with a grid size of 193 x 193. The nominal designs are actually obtained on a grid size of 385 x 385, because the slow grid convergence for shaped-rail sliders(Chapter 5, Fig. 5.9). The design fly height profiles at the read-write element are given in Fig. 6.12, Fig. 6.18 and Fig. 6.24. It can be seen that the sliders have quite flat fly height profiles across the entire disk radius. The pitch angle increases with speed (disk radius) almost linearly, as can be seen on Fig. 6.13, Fig. 6.19 and Fig. 6.25. The variation of the roll over the disk radius is quite small (Fig. 6.14, Fig. 6.20 and

Fig. 6.26). The take-off fly height profiles in Fig. 6.15, Fig. 6.21 and Fig. 6.27 show that these sliders have low take-off low speeds, which is typical of negative pressure sliders. In terms of RPM needed to achieve a fixed percentage of nominal fly height, the two 15 nm designs seem to take off faster than the 25 nm “Nutcracker” design.

6.4 Summary

Several important results have been demonstrated by the first 50% / 25 nm slider design. First, the design is sensitive to etch ramp angle, and a 20 micron lateral offset at the bottom of the etch is sufficient to substantially raise the flying height, especially at the outside radius. Second, if the ramp offset is incorporated in the simulation, then the agreement between the measured and simulated results is good. Third, designs of low flying etched sliders must include the etch ramp angle expected during fabrication as an important design constraint.

Three other negative pressure slider designs are obtained, which have constant fly height profile and low take-off speed.

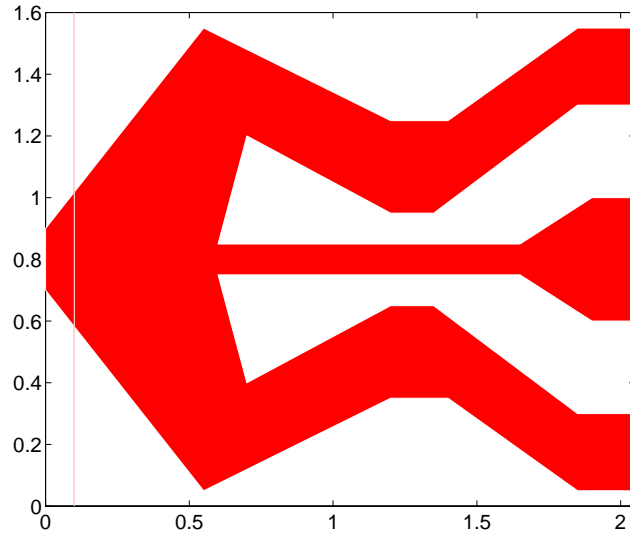


Fig. 6.1 Rail outline of the 50%, 25 nm slider

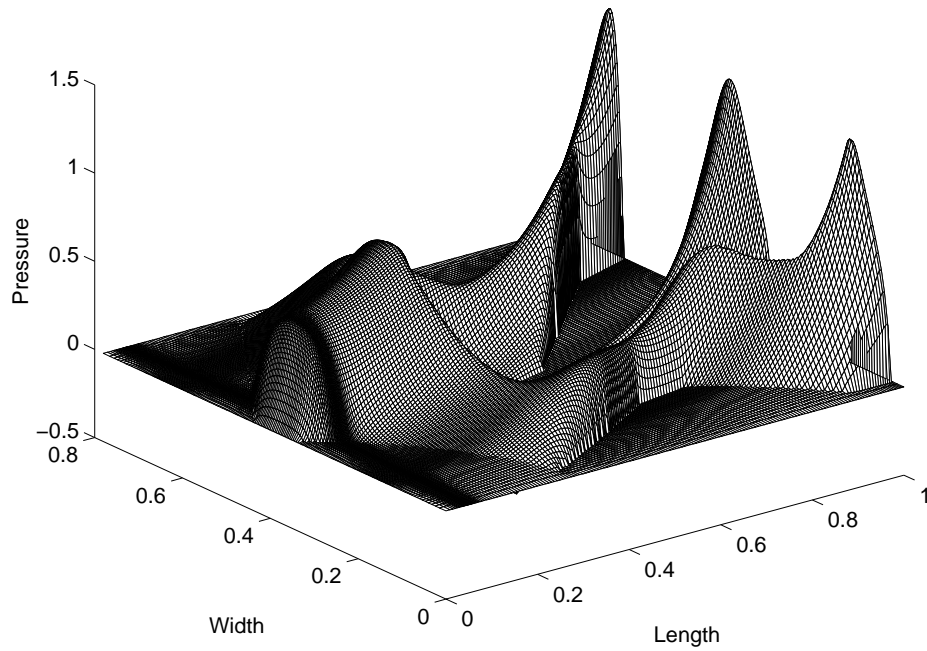


Fig. 6.2 3-D pressure profile for the 50%, 25 nm slider. Radius = 15, skew = -3.88°

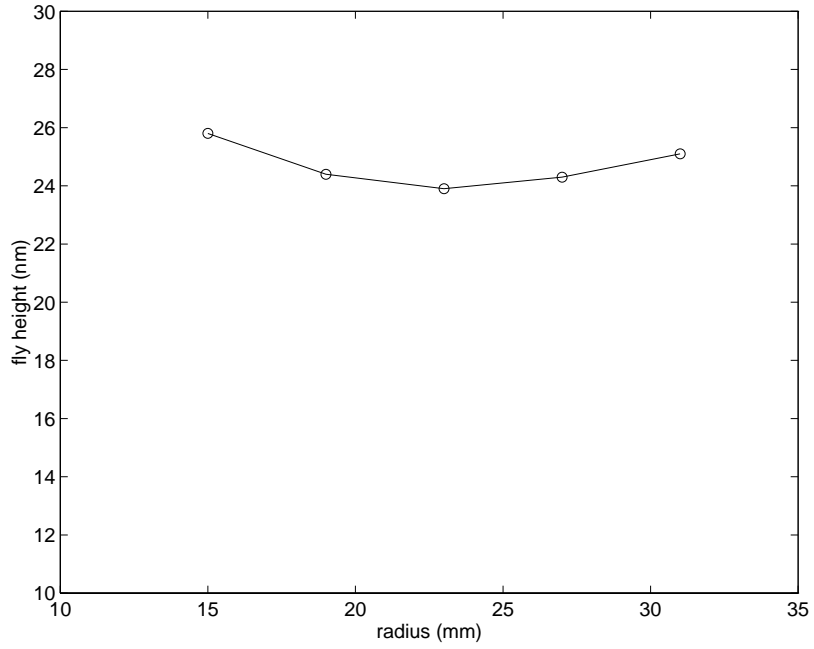


Fig. 6.3 Fly height profile of the 50%, 25 nm slider. Skew = -3.88° to 17.85°

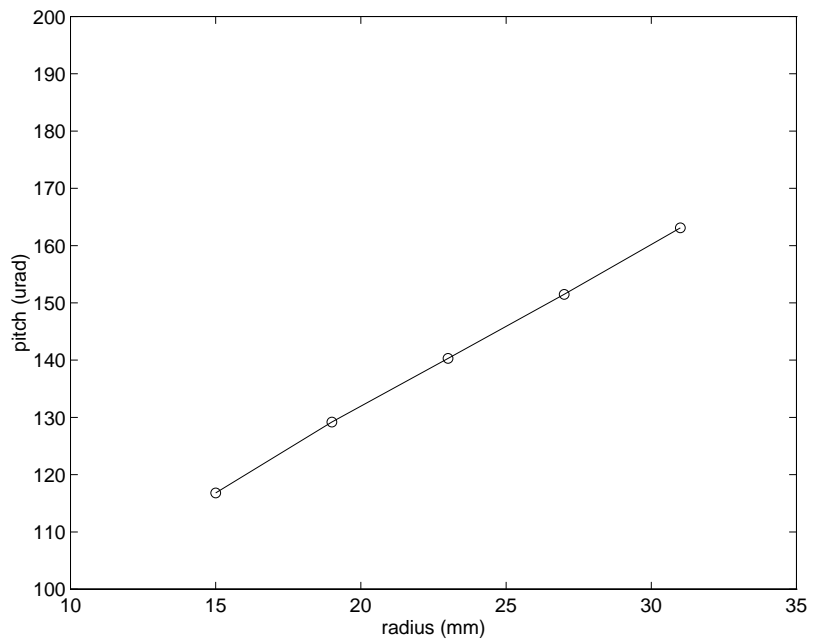


Fig. 6.4 Pitch profile of the 50%, 25 nm slider

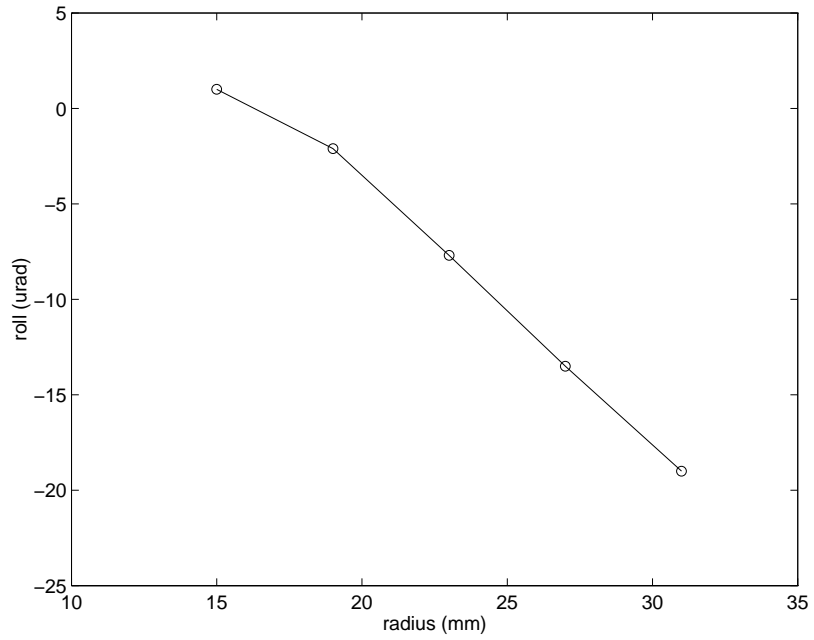


Fig. 6.5 Roll profile of the 50%, 25 nm slider

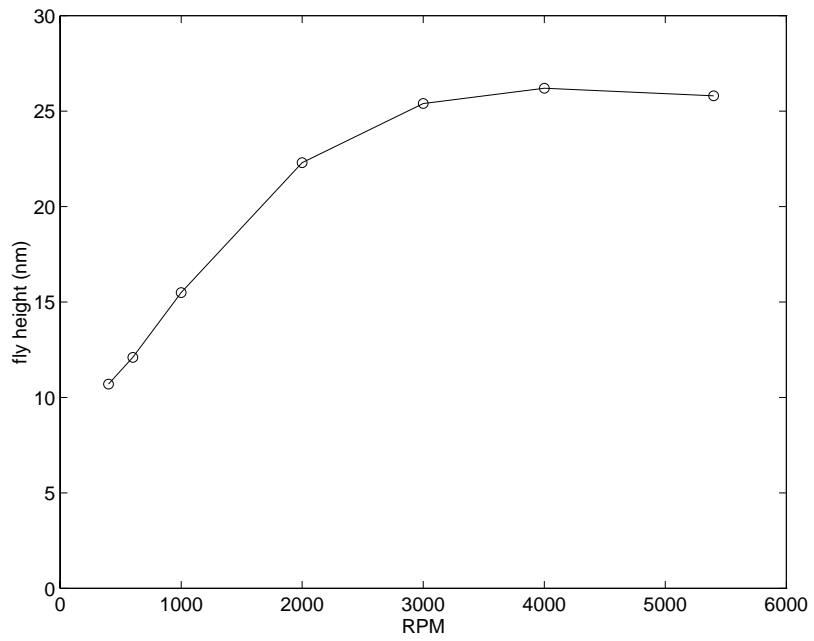


Fig. 6.6 Take-off fly height profile of the 50%, 15 nm slider at ID

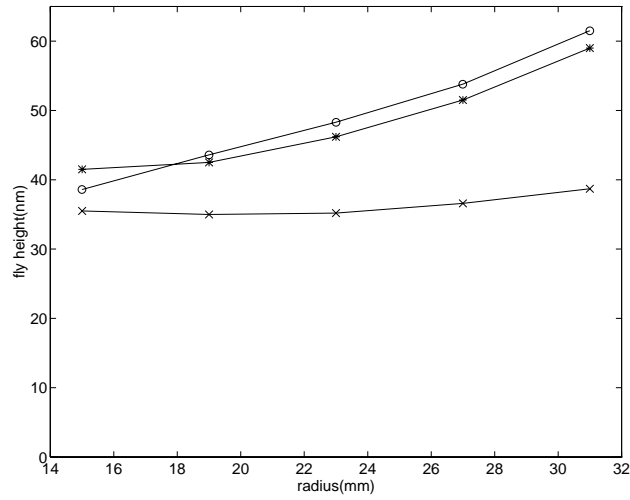


Fig. 6.7 Fly height profile at measuring point. (x): original prediction; (o): measurement; (*): re-calculated

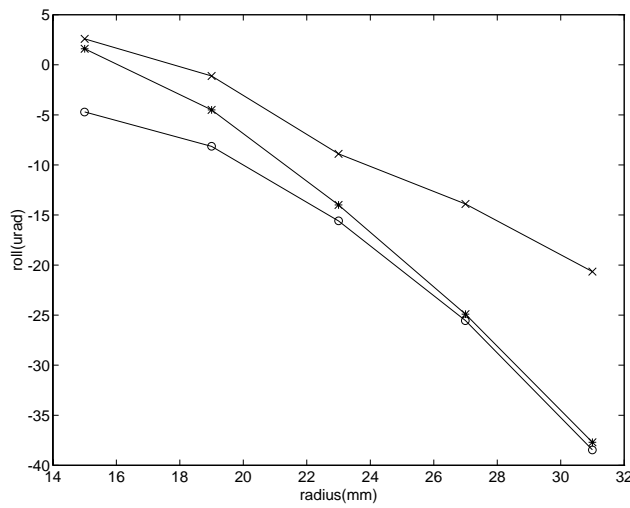


Fig. 6.8 Slider roll (x): original prediction; (o): measurement; (*): recalculated

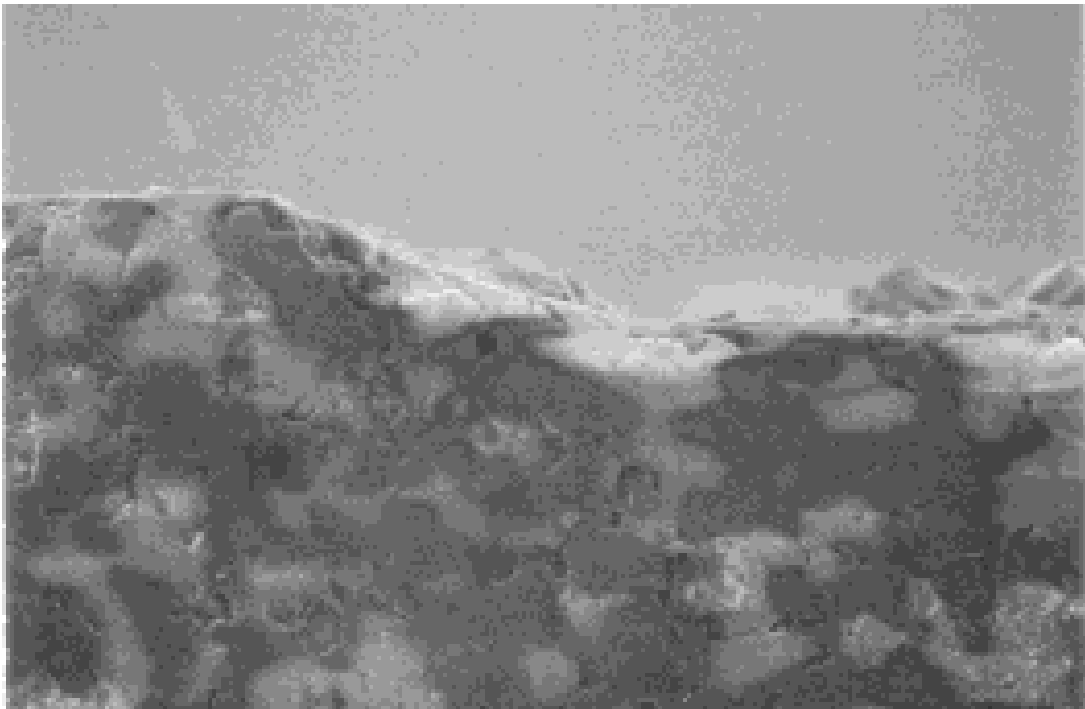


Fig. 6.9 SEM image of the etch slope profile

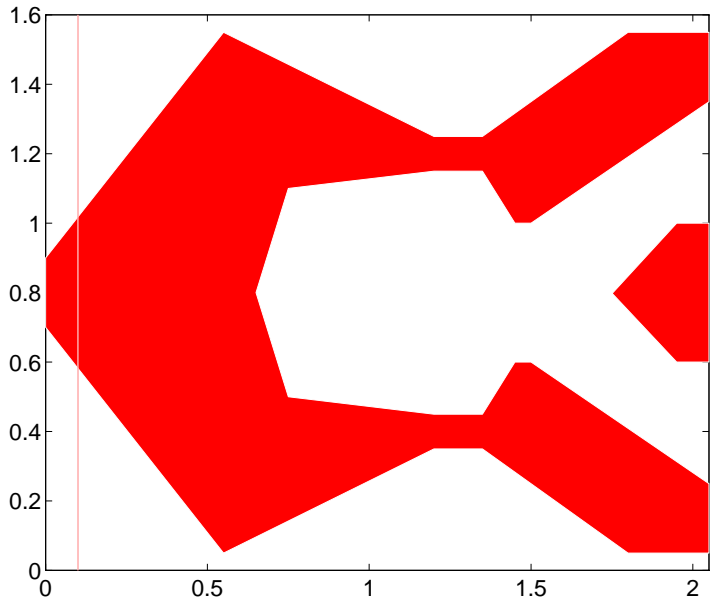


Fig. 6.10 Rail shape of the 50 %, 25 nm Nutcracker slider

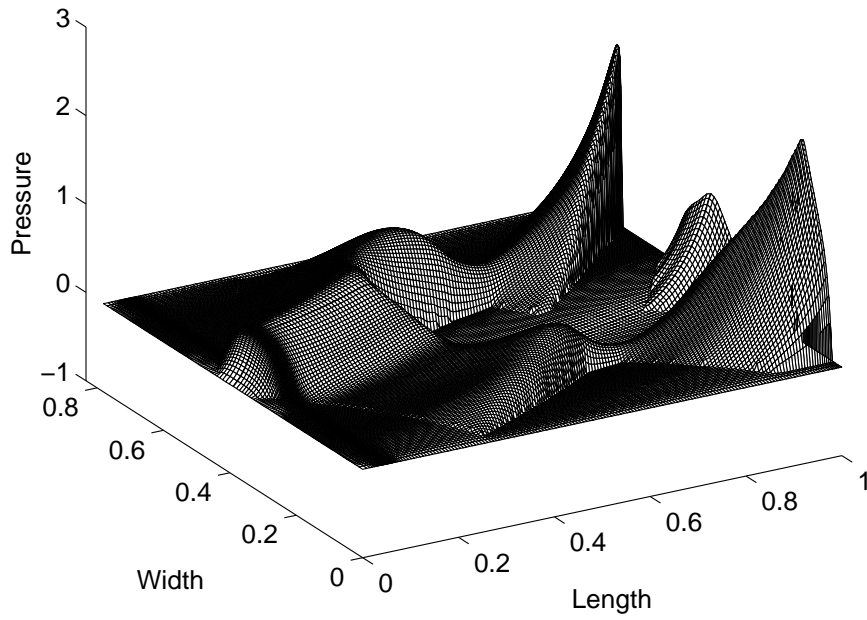


Fig. 6.11 3-D pressure profile of the Nutcracker slider. Radius = 15 mm, skew = -3.88°

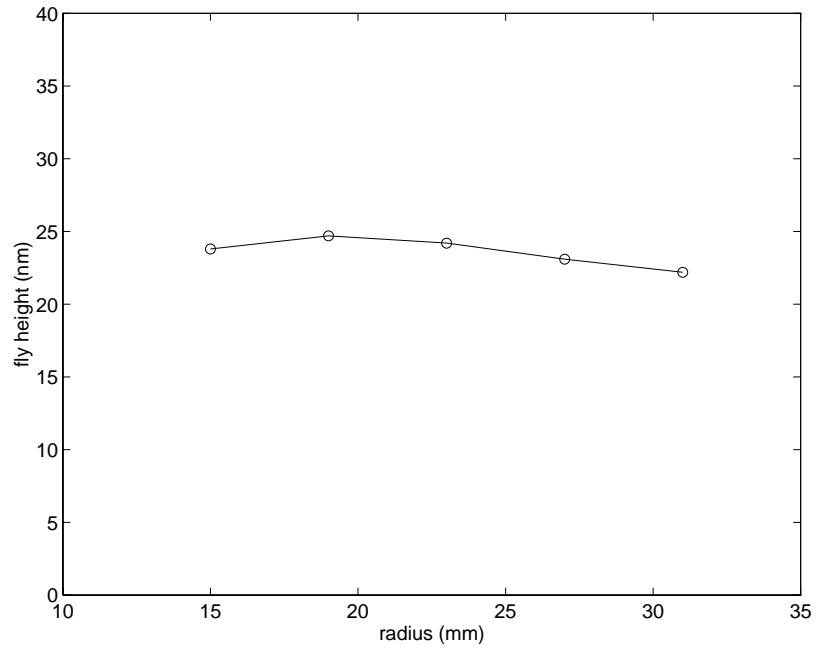


Fig. 6.12 Fly height profile of the Nutcracker slider. Skew = -3.88° to 17.85°

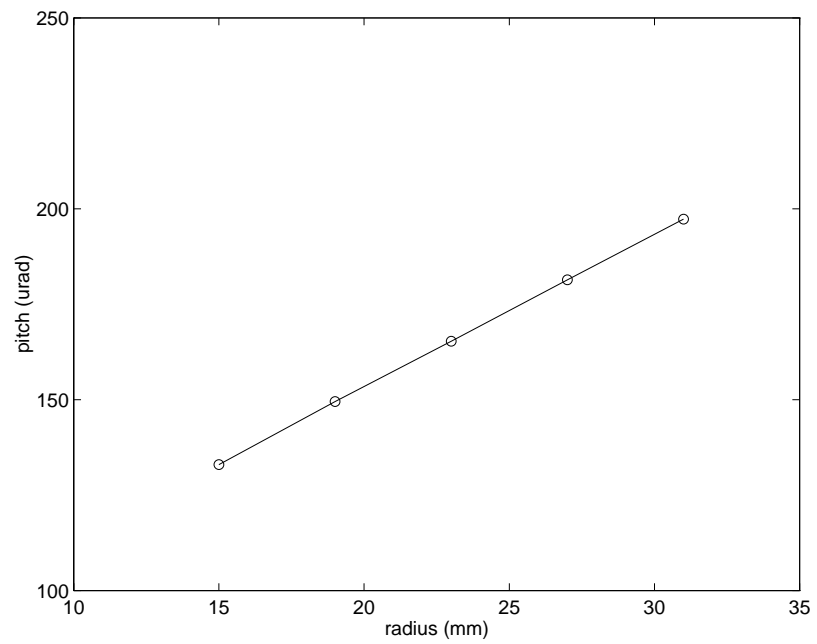


Fig. 6.13 Pitch angle profile of the Nutcracker slider

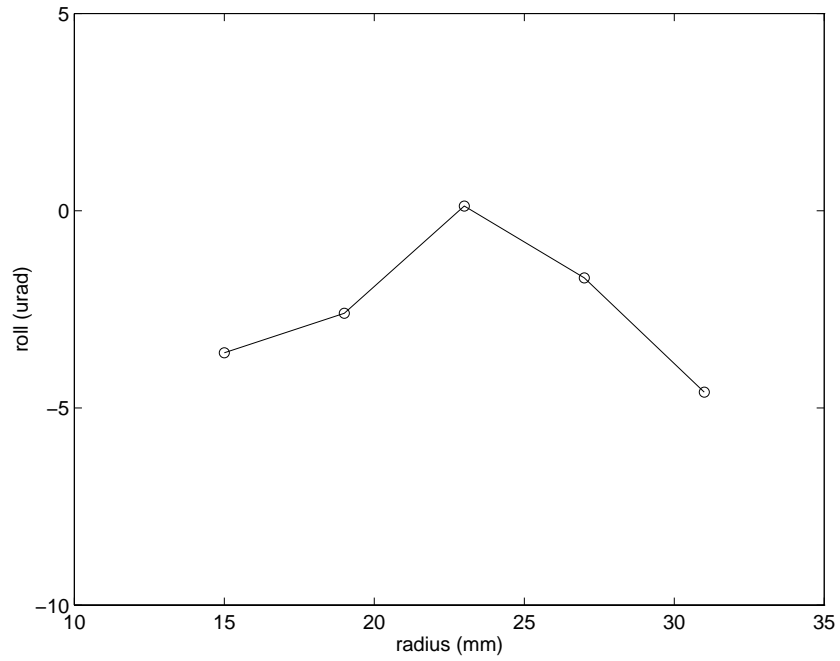


Fig. 6.14 Roll profile of the Nutcracker slider

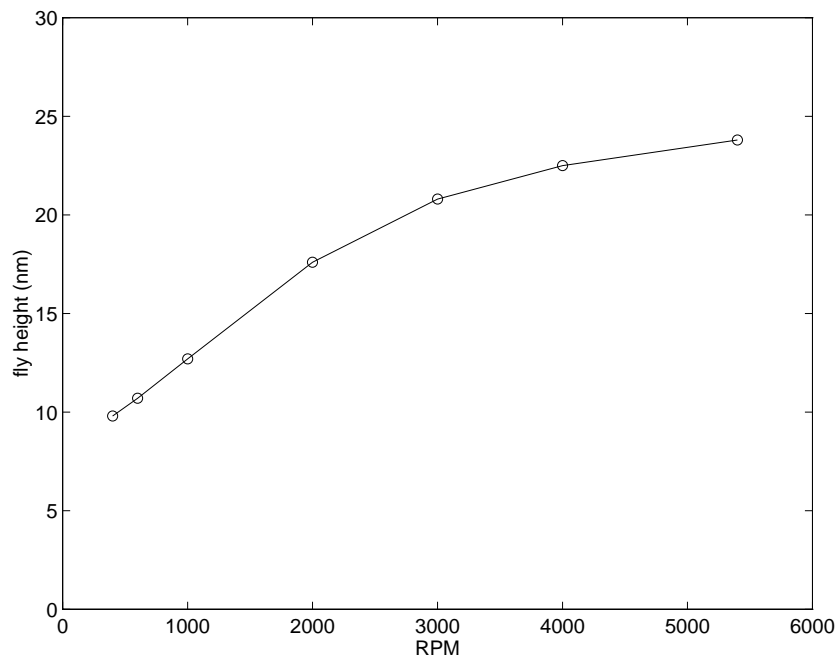


Fig. 6.15 Take off fly height profile of the Nutcracker slider at ID

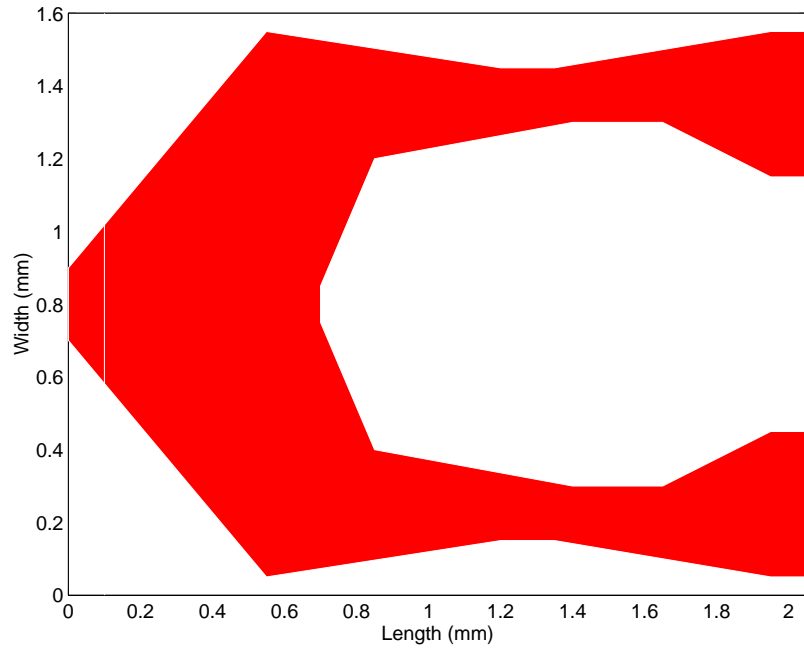


Fig. 6.16 Rail shape of the 50%, 15 nm slider

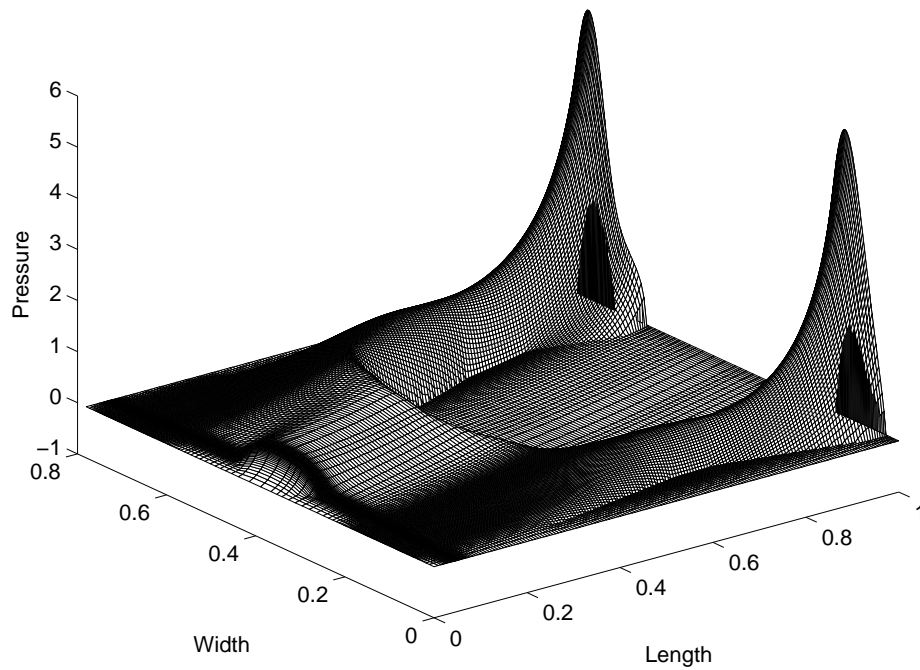


Fig 6.17 3-D pressure profile of the 50%, 15 nm slider. Radius = 15 mm, skew = -6.27°

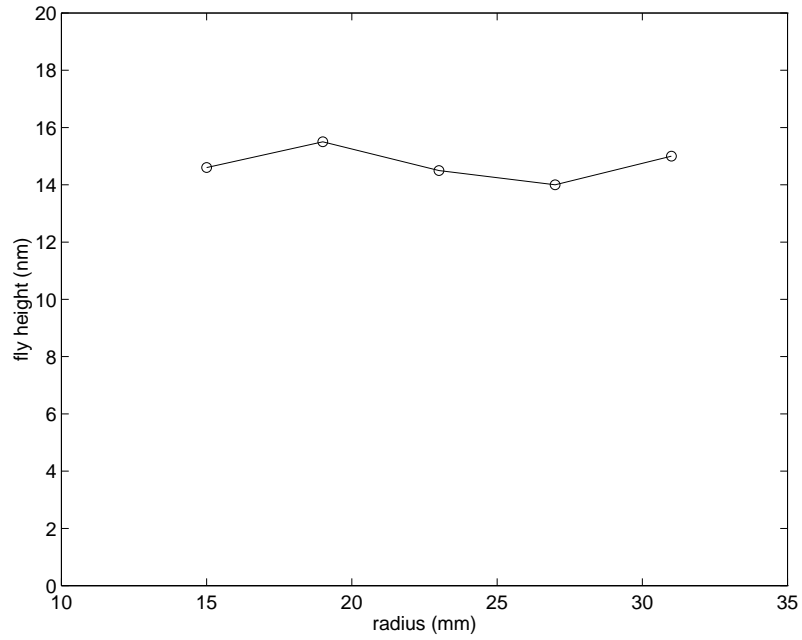


Fig. 6.18 Fly height profile of the 50%, 15 nm slider. Skew = -6.27° to 17°

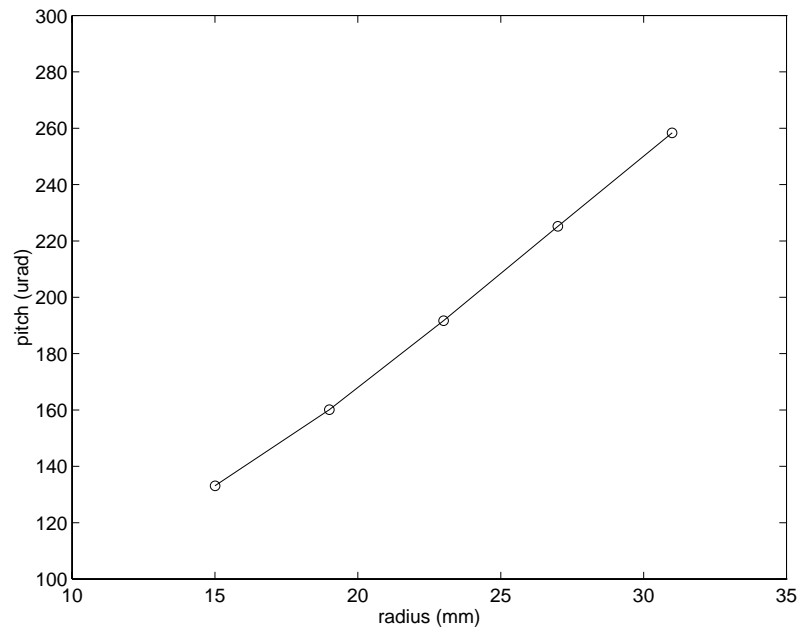


Fig. 6.19 Pitch profile of the 50%, 15 nm slider

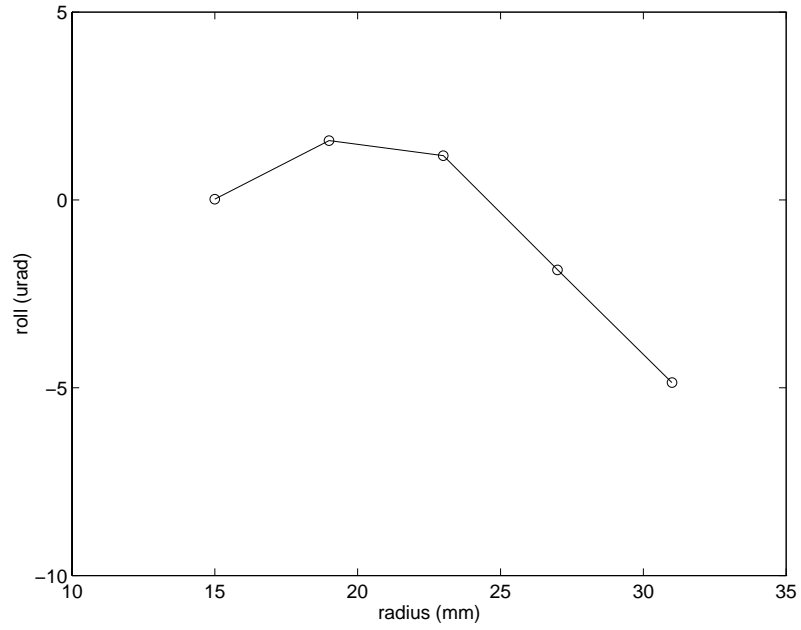


Fig. 6.20 Roll profile of the 50%, 15 nm slider

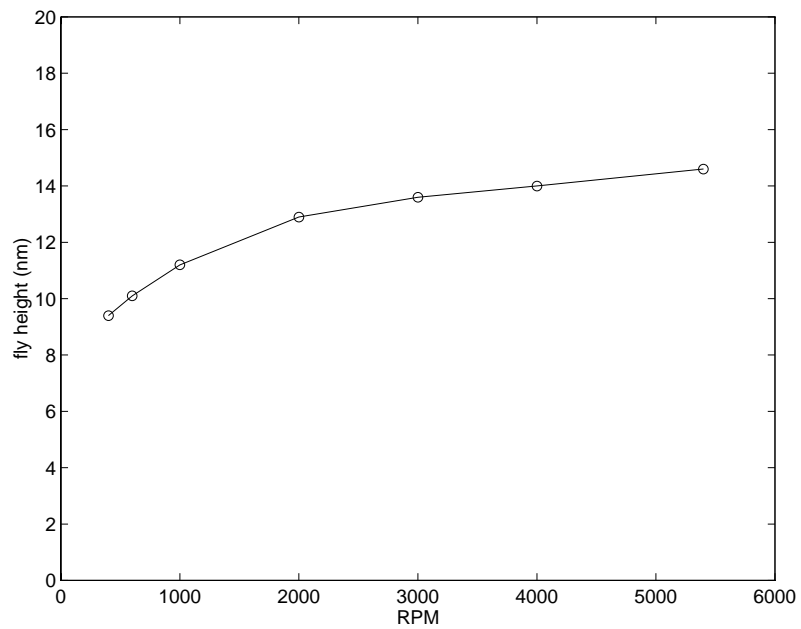


Fig. 6.21 Take-off fly height profile of the 50%, 15 nm slider at ID

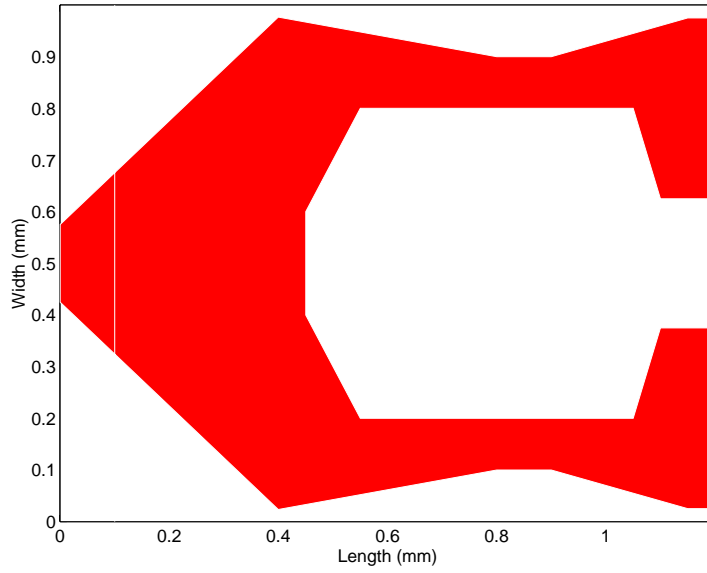


Fig. 6.22 Rail outline of the 30%, 15 nm slider

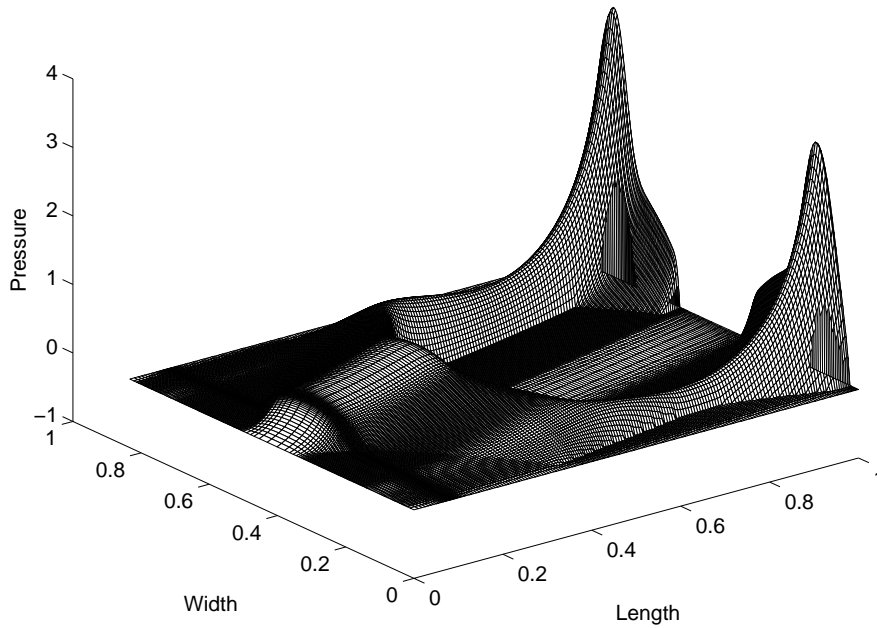


Fig. 6.23 3-D pressure profile for the 30%, 15 nm slider. Radius = 15 mm, skew = -1.22°

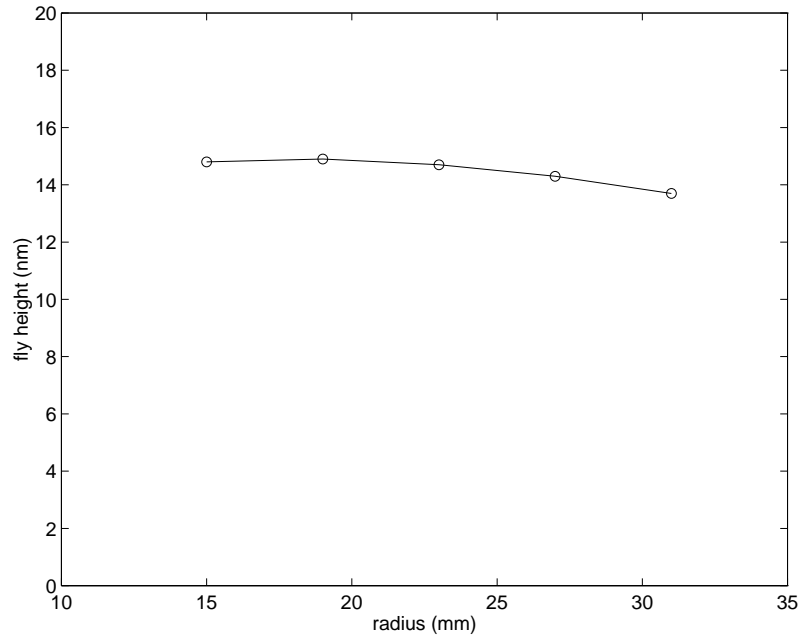


Fig. 6.24 Fly height profile of the 30%, 15 nm slider. Skew = -1.22° to 17.39°

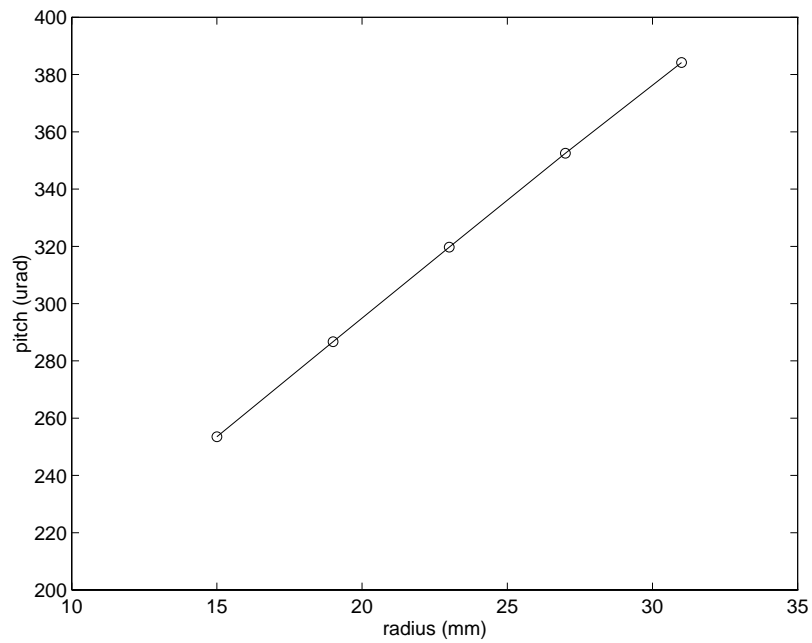


Fig. 6.25 Pitch profile of the 30%, 15 nm slider

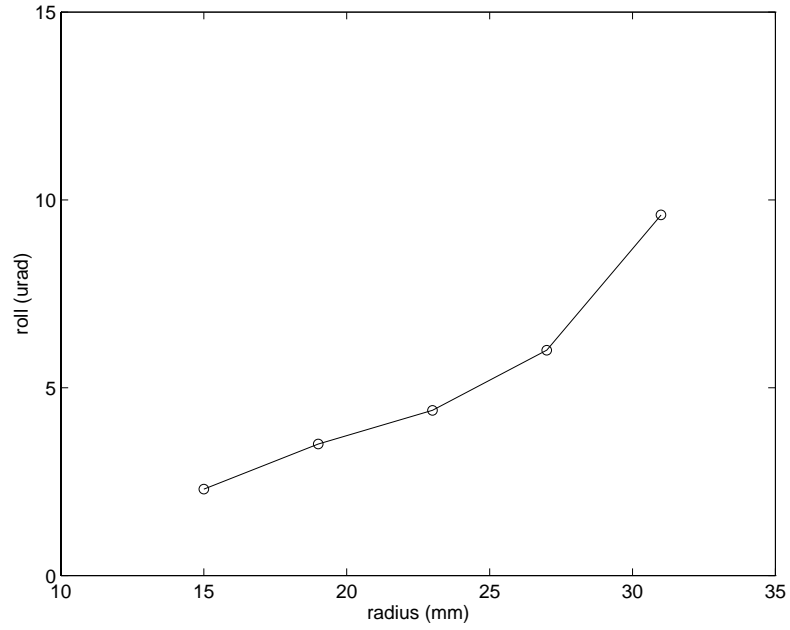


Fig. 6.26 Roll profile of the 30%, 15 nm slider

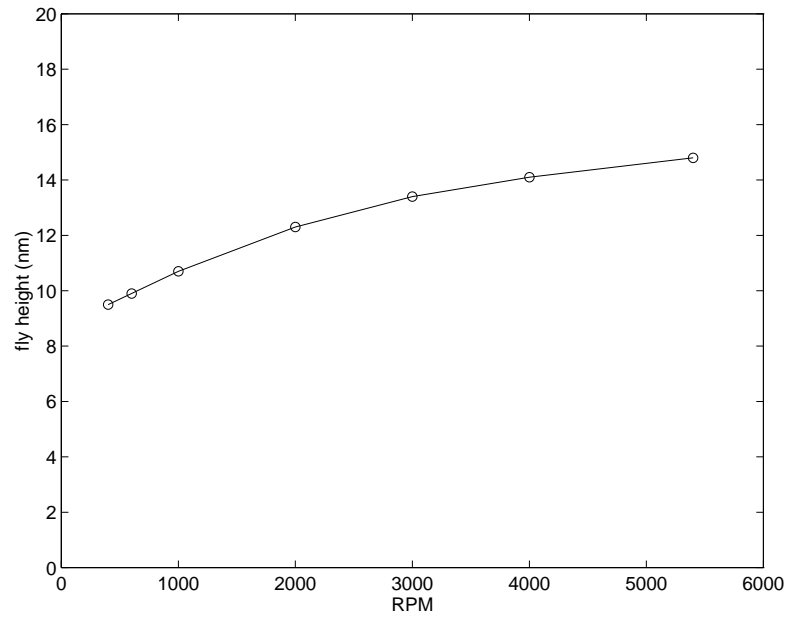


Fig. 6.27 Take-off fly height profile of the 30%, 15 nm slider at ID

CHAPTER 7

CONCLUSION

The continual increase of hard disk drive storage density is driving the slider fly height down to near contact. Sophisticated air bearing designs are being used to meet the demand for air bearing performance characteristics such as constant fly height profile and low altitude sensitivity. The main purpose of this dissertation is to develop a powerful, general purpose air bearing design program that can incorporate all the air bearing features that are being used, including shaped rails, arbitrary wall profiles and multiple etch depths. In addition, a few low flying slider designs are presented, and some air bearing characteristics are studied.

A simple yet powerful control volume method for solving the rarefied gas lubrication equation is outlined in Chapter 2. A mass flow rate averaging method is used for clearance discontinuities, which improves the accuracy of the solution. The effect of the shear force is found to be significant for air bearings with low stiffness.

Chapter 3 presents a piece-wise geometric progression grid generation method as well as a powerful adaptive strategy for grid generation. Grid snapping at the rail boundaries as well as at the taper end is found to be a very effective way of improving solution accuracy and consistency. A multi grid method is implemented in Chapter 4 which improves solver efficiency dramatically. It is particularly effective in dealing with the nonlinearity in the generalized Reynolds equation.

The convective term in the generalized Reynolds equation may cause numerical difficulty if not treated properly, especially under low spacing, high speed conditions. A comparative study is conducted in Chapter 5, using central difference, upwind, hybrid, power-law and QUICK schemes. It is concluded that the hybrid scheme is the best overall.

A few low flying, negative pressure sliders are presented in Chapter 6. It is found that the wall angle produced in the etching process can alter the flying characteristics significantly. Good agreement is found between the predicted and the measured fly height after taking into account the wall angle effect. The negative pressure slider designs all have relatively flat fly height profiles and low take-off speeds.

The air bearing simulation program developed here has become a powerful design tool and is now widely used in the hard disk drive industry.

REFERENCES

Alexander, F. J., Garcia, A. L., and Alder, B. J., 1994, "Direct Simulation Monte Carlo for Thin-film Bearings," *Physics of Fluids*, Vol. 6, No. 12, pp. 3854-3860.

Brandt, A., 1977, "Multi-level Adaptive Solutions to Boundary-value Problems," *Mathematics of Computations*, Vol. 31, pp. 333-390.

Burgdorfer, A., 1959, "The influence of the Molecular Mean Free Path on the Performance of Hydrodynamic Gas Lubricated Bearings," *ASME Journal of Basic Engineering*, Vol. 81, pp. 94-100.

Castelli, V., and Pirvics, J., 1968, "Review of Numerical Methods in Gas Bearing Film Analysis," *ASME Journal of Lubrication Technology*, Vol. 90, pp. 777-792.

Cha, E., 1993, "Numerical Analysis of Head-Disk Assembly Dynamics for Shaped Rail Sliders with Sub-ambient Pressure Regions," *Doctoral Dissertation*, Department of Mechanical Engineering, University of California, Berkeley.

Cha, E., and Bogy, D. B., 1995, "A Numerical Scheme for Static and Dynamic Simulation of Subambient Pressure Shaped Rail Sliders," *ASME Journal of Tribology*, Vol. 117, pp. 36-46.

Fukui, S., and Kaneko, R., 1988, "Analysis of Ultra-thin Gas Film Lubrication Based on Linearized Boltzmann Equation: First Report - Derivation of a Generalized Lubrication Equation Including Thermal Creep Flow," *ASME Journal of Tribology*, Vol. 110, pp. 335-341.

Fukui, S., and Kaneko, R., 1990, "A Database for Interpolation of Poiseuille Flow Rates for High Knudsen Number Lubrication Problems," *ASME Journal of Tribology*, Vol. 112, pp. 78-83.

Gans, R., 1985, "Lubrication Theory at Arbitrary Knudsen Number," *ASME Journal of Tribology*, Vol. 107, pp. 431-433.

Garcia-Suarez, C., Bogy, D. B., and Talke, F. E., 1984, "Use of an Upwind Finite Element Scheme for Air Bearing Calculations," *ASLE SP-16*, pp. 90-96.

Gross, W. A., Matsch, L. A., Castelli, V., Eshel, A., Vohr, J. H., and Wildmann, M., 1980, *Fluid Film Lubrication*, Wiley, New York.

Hardie, C., Menon, A., Crane, P., and Egbert, D., 1994, "Analysis and Performance Characteristics of the Seagate Advanced Air Bearing Slider," *IEEE Transaction on Magnetics*, Vol. 30, No. 2, pp. 424-432.

Hayase, T., Humphrey, J. A. C., and Greif, R., 1992, "A Consistently Formulated QUICK Scheme for Fast and Stable Convergence Using Finite-Volume Iterative Calculation Procedures," *Journal of Computational Physics*, Vol. 98, pp. 108-118.

Hsia, Y. T., and Domoto, G. A., 1983, "An Experimental Investigation of Molecular Rarefaction Effects in Gas Lubricated Bearings at Ultra-Low Clearances," *ASME Journal of Lubrication Technology*, Vol. 105, pp. 120-130.

Kogure, K., Fukui, S., Mitsuya, Y., and Kaneko, R., 1983, "Design of Negative Pressure Slider for Magnetic Recording Disks," *ASME Journal of Lubrication Technology*, Vol. 7, pp. 496-502.

Leonard, B. P., 1979, "A Stable and Accurate Convection Modeling Procedure Based on Quadratic Upstream Interpolation," *Computer Methods in Applied Mechanics and Engineering*, Vol. 19, pp. 59-98.

Lu, S., Hu, Y., O'Hara, M., Bogy, D. B., Bhatia, C. S., and Hsia, Y. T., 1996, "Air Bearing Design, Optimization, Stability Analysis and Verification for Sub-25 nm Flying," *IEEE Transaction on Magnetics*, Vol. 32, pp. 103-109.

Miu, D., and Bogy, D. B., 1986a, "Dynamics of Gas Lubricated Slider Bearings in Magnetic Recording Disk Files: Part I - Experimental Observation," *ASME Journal of Tribology*, Vol. 108, pp. 584-588.

Miu, D., and Bogy, D. B., 1986b, "Dynamics of Gas Lubricated Slider Bearings in Magnetic Recording Disk Files: Part II - Numerical Simulation," *ASME Journal of Tribology*, Vol. 108, pp. 589-593.

Patankar, S. V., 1980, *Numerical Heat Transfer and Fluid Flow*, McGraw-Hill, New York.

Ruiz, O. J., and Bogy, D. B., 1990a, "A Numerical Simulation of the Head-Disk Assembly in Magnetic Hard Disk: 1. Component Models," *ASME Journal of Tribology*, Vol. 112, pp. 593-602.

Ruiz, O. J., and Bogy, D. B., 1990a, "A Numerical Simulation of the Head-Disk Assembly in Magnetic Hard Disk: 2. Solution of the Coupled System," *ASME Journal of Tribology*, Vol. 112, pp. 603-613.

Shyy, W., and Sun, C. S., 1993, "Development of a Pressure-correction/Staggered-grid Based Multi Grid Solver for Incompressible Recirculating Flows," *Computers and Fluids*, Vol. 22, NO. 1, pp. 51-76.

White, J. M., and Nigam, A., 1980, "A Factored Implicit Scheme for the Numerical Solution of the Reynolds Equation at Very Low Spacing," *ASME Journal of Lubrication Technology*, Vol. 102, pp. 80-85.

White, J. M., 1983, "Flying Characteristics of the 'Zero-load' Slider Bearing," *ASME Journal of Lubrication Technology*, Vol. 105, pp. 484-490.

White, J. M., 1991, "The Transverse Pressure Contour Slider: Flying Characteristics and Comparisons with Taper-Flat and Cross-Cut Type Sliders," *Advances in Information Storage Systems*, Vol. 3, pp. 1-14.

Yoneoka, S., Yamada, T., Aruga, K., Ooe, T., and Takahashi, M., 1987, "Fast Take-off Negative Pressure Slider," *IEEE Transaction on Magnetics*, Vol. MAG-23, No. 5, pp. 3464-3466.

APPENDIX A

CML AIR BEARING DESIGN PROGRAM

USER'S MANUAL (MATLAB VERSION)

1. Introduction

This manual describes the Air Bearing Design Program (version 3) developed in the Computer Mechanics Laboratory at the University of California at Berkeley. The current version is fully integrated with MATLAB, which performs the pre and post processing for the simulation. The code solves the slider air bearing pressure distributions for given flying attitude or suspension preload. The latter case is called the inverse problem, and there the steady state flying attitude is found through a Quasi-Newton search procedure.

With the rapid decrease of slider flying height in magnetic disk drive technology in the effort to increase the recording density, air bearing surface designs are becoming more complicated. Sub-ambient pressure air bearing designs are gaining popularity, and they often contain rails with complex shapes. This calls for a robust design tool.

The program described here is intended to facilitate the design of shaped rail sliders. The rail shapes are defined by piece-wise linear boundaries. A rail can be a step with a given recess depth, or it can be defined as a 'ramp', i.e., a flat plane having an arbitrary orientation. Each rail may have a different recess depth. Normally, a zero recess is assigned to the main air bearing surface.

A multi grid method is implemented, dramatically shortening the run time. This method is optimally efficient in the sense that the time for convergence increases only

linearly with the number of unknowns, so its superiority is strongly realized when the number of unknowns is large. An adaptive grid method is also implemented in the program, which can adjust the grid distribution according to the pressure gradient. This usually results in better usage of the available grid points.

2. MATLAB Interface

The pre and post processing is performed through the Matlab interface. To initiate a session, Matlab must be started by entering the command 'Matlab'. Then type 'steady' in the Matlab command window. A greeting will appear on the screen along with a menu bar at the top (Fig. 1). The menu items are labeled *PreProcessor*, *Run*, *PostProcessor*, and *GraphicsOptions*. In the MS-Windows environment, these items are preceded by a few other default menu items (File, Edit, Windows, Help). The user often needs to supply or modify the design parameters through editable texts. To change the editable texts, click the left mouse button once to select and modify, or double click (the box turns black) to overwrite the old values.

2.1 Preprocessor

A sub-menu will appear after clicking on *PreProcessor*, with the choices *SteadyDefinition*, *RailCreation*, *Loadcase*, *Savecase* and *Exit*.

2.1.1 Steady Definition

The prompt for a set of parameters will appear in the graphics window after the *SteadyDefinition* is chosen from the *PreProcessor* sub-menu. The parameters used to define a static air bearing problem are entered through this window (Fig. 2).

Title: enter a name for the case here. It should not contain any dots (.).

Units: choose from SI, British or custom. This will affect the units of most of the parameters. If custom unit is selected, you are prompted to enter the unit conversion factor to millimeters.

Slider length and width: slider dimensions in units specified by units above. Default values are 2 mm x 1.6 mm.

Recess: recess depth for all areas not covered by any of the rails (defined in the RailCreation window chosen from the PreProcessor sub-menu).

Crown, Camber and Twist: enter here the values of global crown, camber and twist in nanometers. These are the second order surface topography components superimposed on each other over the whole slider. Positive crown and camber values represent convex parabolae in the length and width directions, respectively. With a positive twist, the inner leading edge and outer trailing edge are recessed (larger spacing) while the outer leading edge and inner trailing edge are raised (smaller spacing).

Radial position: the distance from the geometrical center of the slider to the disk center.

Revolutions per minute: disk rotation speed.

Skew: skew angle in degrees at the geometrical center of the slider. For positive skew, the flow comes from the inner leading edge towards the outer trailing edge.

Ambient pressure: ambient pressure in Pascals, used as the boundary condition around the entire slider.

Mean free path: mean free path of the air molecules in meters.

Viscosity: viscosity of air in NS/M².

Maximum residual: residual of the discretized Reynolds equation normalized by the main term in the equation, used as the convergence criterion. The default value is small enough for most cases.

Scheme: different schemes have been implemented to treat the convective term in the Reynolds equation; Up-wind, Hybrid, Power-law and QUICK. Considering accuracy, stability and convergence characteristics, the Hybrid or Power-law scheme is recommended.

Model: three different correction models to the Reynolds equation have been implemented to account for the rarefaction effects. Among the First-order Slip Model, the Second-order Slip Model, and the Fukui-Kaneko's Linearized Boltzmann Equation Model, the last one seems to render the best results for low flying, high bearing number cases and it is the default choice.

Stiffness calculation/No stiffness calculation: when this switch is turned on, the program calculates and outputs the 3x3 stiffness matrix. It represents the ratio of the change in bearing force components (bearing load, pitch moment and roll moment) over the change in displacement components (height, pitch and roll). In the current setup, the results are stored in the file 'result.dat'.

Taper specification/No taper: there are two ways to define a taper. In the first way, the taper length and taper angle should be given when this switch is turned on. Accordingly, a wedge with the given taper angle starting at a taper length from the leading edge will be removed from the slider. If the taper can not be properly defined in this manner, it may be defined in the 'RailCreation' window as ramps(see 2.1.2). In this case, the taper switch should still be on, with correct taper length and zero taper angle, so that

when the adaptive grid option is selected, the program will resolve the taper end with enough grid points.

Initial flying attitude: the flying attitude used to start the calculation, including nominal trailing edge center height Hm, pitch and roll. For positive pitch, the spacing at the leading edge is larger than at the trailing edge, and the spacing at the outer rail is larger than at the inner rail for positive roll. For the inverse problem, the specified values are only initial guesses. But the convergence to the steady state flying attitude can be accelerated by using a better initial guess.

Solution for given attitude/Steady steady solution: when solution for given attitude is chosen, the program only calculates the pressure distribution for the given flying attitude. Otherwise, it computes the inverse solution. The code will search for the steady state flying attitude using the Quasi-Newton method. The user has to supply the load and the load position offsets in the pitch (x) and roll (y) directions with the origin at the slider center. The suspension static pitch moment and roll moment can also be supplied. Currently, a non-standard unit of gram-mm is used. Positive static pitch tends to increase the pitch angle and positive static roll tends to lift the outer rail. Maximum error is the normalized difference between the computed bearing load including its moments and the suspension preload as well as its static moments. It is used as a criterion for convergence in the inverse solution. Points of interest allows the user to specify up to four points for which the program outputs the fly heights. The x and y coordinates need to be specified.

Quasi-static take-off/No take-off simulation: when this option is turned on, the user can enter a RPM vector, with the numbers separated by blanks. The code then solves for different RPMs and stores the results in 'result.dat'.

Fixed position only/A group of radial positions/A matrix of radii and skews: the code only solves for one radius when the first option is chosen. The user needs to supply a vector of radii and a skew vector for both the second and third options. In the second option, the length of the radii vector and of the skew vector have to be the same, since there is one-to-one correspondence.

Initial grid: the initial grid can either be created or imported. When the latter is selected, the program reads the grid data from 'x.dat' and 'y.dat' files. These files are created when the program finishes a run. If the initial grid needs to be created, more parameters have to be entered. x grid and y grid are the number of grid points in the x (length) and y (width) directions. They are rounded by the program to the nearest number having the form $(16n+1)$, dictated by the multi grid method in the solver. For example, 100 will be rounded to 97. The program uses piece-wise geometric progression to generate the grids. A uniform grid is generated by default. x controls are a set of points (separated by blanks) by which the slider length is cut into segments. For example, two points cut the length into three segments. In each segment, the successive grid size changes at a fixed ratio. x indices are the grid indices for the control points. The ratios of successive grid sizes in each segment are specified by x ratios. It is similar in the y direction, except that if the symmetry in width is chosen instead of specify entire width, the grid needs only to be specified on half the width.

Adaptive grid control: no matter how the initial grid is obtained, the user has the option to use adaptive grid or fixed grid only. When adaptive grid is chosen, the program will generate an adaptive grid according to various measures of the pressure gradient after an initial calculation. The user has some control over the method by which the adaptive

grid is generated. In order to compute the grid density in one direction, e.g., x direction, the user can choose to use either the maximum or the averaged pressure gradient along all the y locations. The pressure gradient in some area may be very small(e.g., a fully relieved region), but some minimum grid concentration may be needed. The user can specify the ratio max/min pressure gradient(grid density). A smaller ratio generates a more uniform mesh. Also, the pressure gradient may change abruptly, but such abrupt changes in the grid distribution should be avoided to reduce discretization error. A smoothing method has been implemented so that the pressure gradient at one point not only affects the grid density at that point, but also has an exponentially decaying influence over neighboring locations. The larger the decay factor, the more abruptly the grid density changes.

2.1.2 Rail Creation

Choosing this option from the 'PreProcessor' sub-menu will create a new window for drawing the rail shapes by use of the mouse (Fig. 3). If some old rail data already exist in Matlab, the user will first be prompted by the choices: Erase old rails, Edit old rails and Add new rails. The first option erases the old rail data, while the second option enters the editing mode. The last option keeps the old data and allows the user to add new rails.

The rectangular box in the window with a dashed square grid represents the slider. The grid lines in the box are reference lines. The units of the axes are given by units discussed in 2.1.1. In the lower left corner of the window, the current position of the mouse pointer is indicated.

Drawing the rails: the rail shapes are generated by piece-wise linear segments. The user can input a rail point at the mouse pointer by clicking the left mouse button. To

drag the line only horizontally, type 'h' on the keyboard while holding the mouse still. Type 'v' to drag it only vertically. The right mouse button should be used to fix the last point of the rail. The rail boundaries are marked by lines of different colors, with small circles around the rail points. The rails and boundary points are labeled by letters in the same color as the lines. For some rail shapes, the rail label may fall outside its boundary. When the last rail is finished, click the right mouse button again. Two small editing windows then appear on the right side of the window (Fig. 3).

Editing the rail as a whole: the upper editing window is used to edit each rail. The user can either click on the letters 'Rail No.x' on the rail to make that rail current, or the user can click and change the rail number on the first line in the editing window. The next two lines display the \underline{x} and \underline{y} limits of the smallest rectangle containing the current rail to help the user identify the current rail. The push buttons that follow perform the editing functions. Mirror creates another rail which is a mirror image of the current rail with respect to the slider's center line. Clicking on Delete will delete the rail. To move the current rail to another location, click on Move, then click on any place in the slider and move the mouse, click again when the rail arrives at the desired location. The amount of displacement is shown in the lower left corner. A similar procedure can be used to Copy the current rail and put it in a new location. If one single rail is symmetrical with respect to the slider's center line, the user needs only to draw half of the rail, and use Symmetry to create the other half. Note that the first and last points in the half rail will be connected to their corresponding mirror images. The user should arrange these two points properly in the half rail to create the correct rail. Rotate can be used to change the orientation of the rail. The procedure is similar to that of moving the rail. Sometimes the display may be

incorrect after editing, possibly due to Matlab graphics bugs. The problem can be corrected by going back to the top menu and returning to the *RailCreation* window again.

Next, the user can specify whether the rail is a *step* or a *ramp*. A step has a uniform *recess* depth. The number is positive for recess under the ABS. Arbitrary wall profiles can be specified around the entire rail. Here, the wall profile can include both the edge blend and the etch slope. The profile is approximated piece-wise linearly. The user can enter a series of *points* by specifying their distance to the nominal edge, separated by blanks. The coordinates may start from negative numbers (edge blend) and end with positive numbers (etch slope). Corresponding to each point, a *recess* value should be specified. The recess values should be separated by blanks. When the same point is repeated and given different recess values, a discontinuity can be included. If the number of points is less than 2, the wall profile is ignored by the program and a nominal discontinuity is assumed. A *ramp* is a plane having an arbitrary orientation. It can be used to define a taper region (another way to define a taper is described in 2.2.1). It is defined by specifying the *recess depths at the first three rail points* (they should not be on the same line). Again, positive recess is below the ABS. Wall profiles can not be specified for a ramp.

Editing the rail points: the lower window provides functions for editing the rail boundary points. Clicking on the point index letter on the rail will make that point current, or the user can click and change the *rail* and *point* indices on the first line of the editing window. The next two lines show the x and y coordinates of the current point. The user may enter different coordinates to change the current point. This may be useful when exact coordinates are desired, since the mouse input has limited resolution, or the

user can choose Change and click at a new point on the slider to change the current rail point graphically to the new point. To insert points between the current rail point and the next one, select Insert and click on new points on the slider. Use the left button to insert points and the right button for the last point.. Snap moves the current rail point to its closest neighbor. This function is used when two points belonging to different rails are meant to be identical. Select Delete to delete the current rail point. Pivot works similarly to Insert, except that all the points inserted are projected to the arc beginning from the current rail point and pivoted at the user specified pivot point, whose coordinates are entered from the box appearing on the right. This provides a convenient way to define an arc in the rail boundary.

2.1.3 Load Case

Existing cases can be loaded into Matlab by choosing LoadCase in the menu. The case files are in .mat format. The user is provided with a list of cases to choose from. The input data files STEADY.DEF, RAIL.DAT, MULTCASE.DAT and TOL.DAT are updated to the current case.

2.1.4 Save Case

The SaveCase option saves the current case in .mat format. It also generates the input files STEADY.DEF, RAIL.DAT, MULTCASE.DAT and TOL.dat used by the simulator. The user will be prompted to enter the case name, which can be modified here.

2.2 Run

After the case is saved, the user can start the simulation by choosing this item and clicking on Steady. The letters 'Simulator Running ...' will appear on the screen. The user can monitor the progress through the output window(in X Windows, bring up the Matlab

command window). When the program finishes, the results are loaded into Matlab and saved in the .mat format.

When running on a PC, the program is loaded into memory much faster in the DOS environment than in Windows, since other Windows programs take away part of the RAM. Here is the procedure to do this:

After saving the case, quit Matlab and MS-Windows, go to the appropriate directory in DOS, start the simulator by the command QUICK301(executable file of the simulator). When the case is finished, start MS-Windows and Matlab, go to the appropriate directory, start the interface STEADY, choose LoadCase in the Preprocessor, load the saved case, go to the PostProcessor menu, choose Loaddata. The case will now be saved along with the result data and will be ready for post processing.

2.3 Post Processor

The functions provided in this menu can be used for post processing of the data generated by the simulator. It has limited capability so far.

2.3.1 Load Data

This is only used when the simulator is run outside the interface(see 2.2).

2.3.2 View Grid

The final grid used in the computation is displayed.

2.3.3 View Rail

The rail areas are filled with color.

2.3.4 3-D Pressure

The 3-D pressure contour is displayed with a color scale.

2.3.5 Settling History

The Quasi-Newton iteration history of various variables is displayed. The eight figures are the iteration histories of :

load err(normalized difference between bearing load and moments and the suspension load and static torques);

nominal trailing edge center flying height(on the flat reference plane with pitch and roll)(nm);

pitch angle(micro radian);

roll angle(larger outer rail gap for positive roll)(micro radian);

flying heights for four points of interest(coordinates start from the inner leading edge, normalized with slider's length)(nm);

2.3.6 Print

This option will invoke the Matlab print command to print out the contents of the current figure window, equivalent to typing 'print' in the Matlab command window.

2.4 Graphics Options

This menu provides some graphics options mainly for the 3D pressure contour.

2.4.1 Color Control

Color map: the user can choose different colormaps to plot the pressure. By default, Matlab colormap 'jet' is used, which ranges from blue for the low pressure region to red in the high pressure region.

Shading: flat shading fills the surface with piece-wise uniform colors, while the interpolated shading smoothes the color between grid lines by linear interpolation.

Faceted shading adds black grid lines to the flat shading. The *no shading* option draws only the color coded grid lines, which is the default choice.

Brighten: A slider will appear at the bottom of the figure window. The user can adjust the brightness of the picture using the slider.

2.4.2 View

When this option is selected, sliders will appear at the lower left corner of the figure window. The viewing angle can be adjusted through the sliders or by just typing in the numbers. Two angles can be adjusted. The viewer moves around the object counter-clockwise in the horizontal plane with the increase of *azimuthal angle*. The viewer looks straight downward with 90 degrees *elevation angle*, horizontally at 0 degrees, and straight upward with negative 90 degrees.

3. Tutorial

In this tutorial, the usage of the interface is illustrated through an example.

3.1 Some Rules for Creating the Rails

The current implementation enables the inclusion of very complex rails and geometric features. In order to simplify the rail creation process and ensure consistency, it is important to follow the basic rules outlined below.

1. A 'rail' is classified into two types: *step* and *ramp*. A *step* is parallel to the reference surface, while a *ramp* is a plane with arbitrary spatial orientation. In fact, a *ramp* can also be used to define a *step*.
2. Any area that is not defined as a 'rail' assumes the recess depth defined in the *recess* box in the *SteadyDefinition* window.

3. Any given area on the slider can be occupied by more than one rail. The only rail that is effective in the given area is the one with the highest rail index (the last one created). This rule can be utilized to simplify the creation of certain rails, e.g., the TPC rails.
4. In the current version, each rail of the *step* type can have an arbitrary wall profile. A *ramp* does not have a wall profile. Also, for any given point, if it is covered by some *ramp*, then it does not belong to any wall profile region. If a wall profile extends beneath some other surface or another wall profile, that part of the wall profile is ignored.

3.2 An Example

To start Matlab, type 'matlab' in the command shell.

Type 'steady' in the Matlab command window. Figure 1 shows the interface window as it appears in MS-Windows environment.

Choose the *PreProcessor* on the top menu bar, and select *Steady Definition*. A table of parameters appears(see Fig. 2). The user may change the default values by double clicking and typing new numbers. Some parameters shown in Fig. 2 have already been modified from the default values.

Next, choose *Rail Creation* in the *PreProcessor* menu to start drawing the rails. The rectangular box represents the slider. Click the left button of the mouse to enter rail boundary points. Rail shapes are approximated by piece wise linear segments. Click the right mouse button when entering the last point in a rail. When all the rails are drawn, click the right mouse button again to finish the drawing mode and enter the editing mode. Figure 3 shows two rails. Note that Rail No. 2 has only two points at this stage. Don't be

concerned if mistakes are made or the locations of the points are not accurate. Everything can be corrected in the editing mode.

In the editing mode, two small editing windows appear on the right side of the slider box (see Fig. 3). The top one is for editing the rail as a whole, and the bottom one is for editing individual points on the rail. To select a particular rail to edit, click on 'Rail No.x' in the middle of the rail(the rail index may be outside the rail for some concave rails), or simply type the rail index number on the top of the rail editing window. Similarly, to choose a point to edit, click on the point indices on rail boundaries or enter the indices on the top of the point editing window.

Now, the point coordinates for Rail No. 1 can be modified by using the point editing functions if necessary. In fact, the exact coordinates can be entered directly in the point editing window. The two points in Rail No. 2 are meant to be coincident with Points 1 and 2 of Rail No. 1. However, when they are entered from the mouse, this can not be done exactly. The way to correct it is to either enter the coordinates directly or use the *snap* editing function.

After all the coordinates are made exact, select Rail No. 2 and click on the *Symmetry* function of the rail editing window. The other half of Rail No. 2 is created (see Fig. 4). Then select Rail No. 1 and click on the *Mirror* function in the rail editing window. A mirrored rail is now generated (also see Fig. 4). The height information for the rails can be entered from the lower part of the rail editing window. The rails here are defined as *steps*. The first *recess* describes the global rail height relative to the reference surface. Usually, the nominal ABS is used as the reference surface. Therefore, Rail No. 1 is given zero recess. An arbitrary piece-wise linear wall profile can be entered using no

more than ten points. If fewer than two points are given, a vertical wall is assumed. Here, a linear etch slope is given for Rail No. 1 (see Fig. 4) and Rail No. 3, extending from the ABS to the etched pocket (3 um deep as prescribed in *SteadyDefinition* window) with a width of 15 um. On the other hand, Rail No. 2 near the leading edge has 1 um recess relative to the ABS, thus its wall profile also starts from 1 um recess(see rail editing window in Fig. 3). The rails are now fully defined.

Now go back to *PreProcessor* and select *SaveCase*. The title is prompted on the screen and can be modified. Click on *OK* to save the case.

Choose *Run* on the menu bar and click on *New*. The program now starts to run. When the case finishes, the data are loaded into Matlab automatically and are ready for post processing. An alternative way to run the program on a PC is described in 2.2.

Go to *Post Processor* on the menu bar. Figure 5 shows the three dimensional pressure contour generated by the *3-D Pressure* option. The effect of the recess of Rail No. 2 on the leading edge pressure is evident in this plot. The final grid generated by the adaptive grid algorithm is shown in Fig. 6.

4. Input And Output Data Files

When the case is saved in the Matlab interface, a few data files are generated which are ready to be used by the FORTRAN program.

4.1 Input File 'steady.def'

The file 'steady.def' contains most of the parameters in the *SteadyDefinition* menu in the interface. Not all the parameters in this file are currently used by the program.

The following is a list of currently active parameters:

hm(m) : nominal initial trailing edge center flying height. Note that the reference point is on the nominal plane with pitch and roll, not including crown, twist or camber.

h0 : nominal leading edge center height, normalized with hm.

hs(rad) : roll, positive roll widens the outer rail gap.

xl(m) : slider length.

yl : slider width normalized with xl.

ske(deg) : skew angle, positive skew implies that the air flows from the inner to the outer rail.

ra(m) : radial position of the slider center.

rpm : revolutions per minute.

isolv : 0 = solve for fixed flying attitude, 1 = find steady state flying height.

f0 (kg) : suspension load

xf0 : load x-position, normalized with xl, starting from leading edge.

yf0 : load y-position, normalized with xl, starting from center towards outer edge.

xfS : static pitch moment in g-mm, positive value tends to increase the leading edge spacing.

yfS : static roll moment, positive value tends to increase the outer rail spacing.

istiff : 0 = no stiffness calculation; 1 = calculate stiffness matrix.

akmax : normalized residual of Reynolds equation, criterion of convergence of the solver.

emax : normalized difference between the current bearing load and the target suspension load, the criterion of convergence for the inverse solution.

p0(pa) : ambient pressure.

al(m) : mean free path of air.

iadpt : 1 = use adaptive grid; 0 = disable adaptive grid;

isymmetry: 0 = manually generate the grid over the whole slider width; 1 = generate only half of the grid, which is symmetrical in the slider width direction. This has no effect when the adaptive grid option is used.

ioldgrid: 0 = either use adaptive grid or manually generated grid; 1 = use the old grid locations in the files x.dat and y.dat.

nx, ny : grid size, must be in the form of $(16n+1)$ because of multi grid method.

nsx, nsy : number of grid sections in x and y directions, respectively, for manually generated grids.

nest : multi grid level. nest = 4 is the highest level and should be used.

xnt(i) : i from 2 to nsx, coordinates for the end of each section in the x direction, normalized with xl.

nxt(i) : i from 2 to nsx, grid indices for the end of each section in the x direction.

dxr(i) : i from 1 to nsx, ratio of grid size over previous one for each section in the x direction.

ynt(i) : i from 2 to nsy, coordinates for the end of each section in the y direction, normalized with xl.

nyt(i) : i from 2 to nsy, grid indices for the end of each section in the y direction.

dyr(i) : i from 1 to nsy, ratio of grid size over previous one for each section in the y direction.

vis1 : viscosity of air.

idisc : different schemes for treating the convective term. 1=power-law; 2=central difference; 3=upwind; 4=hybrid; 5=central difference in the hybrid form; 6= QUICK; idisc=1 is recommended.

iqpo : slip flow models, 0=continuum model; 1=first order slip model; 2=second order slip model; 5=Fukui-Kaneko linearized Boltzman equation model. 5 is the recommended choice.

difmax : used in the adaptive grid, a larger number allows a larger grid density difference.

decay : used in the adaptive grid, a larger number has less smoothing effect, and the grid density depends more on the local pressure gradient and may change more abruptly.

ipmax : used in the adaptive grid, 0 = use averaged pressure gradient in each direction along the cross section grid locations; 1 = use

the maximum gradient in each direction along the cross section grid locations.

4.2 Input File 'rail.dat'

The first line in 'rail.dat' indicates how many rails are defined and how many different recess heights they possess.

The data for each rail follow. First, the number of boundary points, the recess height index of the current rail and the number of points in the wall profile are given. The last number should be less than two if the rail is of the ramp type (the recess height index is 0). Next, the coordinates of the boundary points normalized with slider length are shown, with the origin at the inner leading edge. If the recess height index is 0, there is an additional line consisting of recess depths for the first three boundary points of the rail. Finally, if the wall profile has at least two points (otherwise a vertical wall is assumed), two more lines are used to describe it. The first line gives the coordinates of the points in terms of the normal distance to the nominal wall normalized by the slider length. Points with negative coordinates are inside the nominal rail boundary, and those with positive coordinates are outside the boundary. The second line contains the recess values (in meters) for the wall profile points.

After all the rails are defined, there is a line which gives the base recess depth (areas not defined as rails), and rail recess depths in index order. All recess values are in meters. The next line shows taper length (normalized with slider length) and taper depth in meters. If a virtual taper exists, but is defined using 'ramps' instead of by the 'taper specification' section in the 'SteadyDefinition' of the interface, the taper length should be

set to the actual value, with zero taper depth at the front. The code will then try to resolve the taper end automatically when the adaptive grid is used.

The next line contains information on crown, twist and camber in meters. The crown is a longitudinal parabolic surface superimposed on the whole slider. A positive crown decreases the spacing between the slider and the disk. The camber is the same as the crown except that it is in the transverse direction. The twist is given in terms of the relative height of four corners to the center. A positive twist increases the separation between the slider and the disk at the inner leading edge and the out trailing edge, and decreases the separation at the outer leading and inner trailing edge.

The last two lines give the x and y normalized coordinates of four points on the slider, respectively. The program outputs the fly height at these four points.

4.3 Input File 'tol.dat'

This file contains the information about sensitivity parameters. It is currently inactive. The first parameter should be set to zero.

4.4 Input File 'multcase.dat'

This file can be used to run multiple cases for different skew, radius, RPM.

The first line contains five integers: itake, nrpms, imultcase, nrads, and nskew.

itake: 0, no quasi-static take-off simulation; 1, yes.

nrpms: number of different RPMs for the take-off (maximum 10).

imultcase: 0, fixed radius; 1, a group of cases with a different skew corresponding to each radius; 2, a matrix for a set of skews and a set of radii.

nrads: number of different radii(maximum 10).

nskew: number of different skews (maximum 10, = nrads if imultcase = 1).

Lines 2 - 4 contains a group of RPMs, radii and skews, respectively.

4.5 Output Files

The pressure matrix is stored in the file 'p2.dat'. The files 'x.dat' and 'y.dat' contain the normalized x and y coordinates, respectively. The iteration history of the flying attitudes is stored in the file 'invs.dat'. The file 'result.dat' contains the final flying attitudes and the stiffness matrix.

APPENDIX

Installation Guide

There are two main directories on the diskette, which are for PCs and UNIX workstations respectively. The .m files and FORTRAN source codes are in the PC directory only, since they are the same for workstations. The FORTRAN source programs should be renamed '*.f' from '*.for' for the workstation version. Only the executable files are provided in the workstation directory. They may be either in DEC Alpha or IBM RS/6000 format depending on the user's specification. For other computer models, the user needs to re-compile the source programs. The user interface requires Matlab 4.1 or later version.

a. PC version

1. There should be at least 8 MB RAM available. The system should be running MS-Windows 3.0 or later.
2. Put .m files in a separate directory. Add its path to 'matlab\matlabrc.m'.
3. Put 'new4g.vmc' in the c:\ directory. Add the contents in 'autoexec.cml' to 'autoexec.bat'.

4. Put the other files in a separate directory and add the path in 'autoexec.bat'.
5. Set the MS-Windows swap space to 30 MB. Please refer to MS-Windows User's Manual.
6. Create or edit 'matlab\startup.m' if necessary. For example, adding the line 'cd c:\case' enables Matlab to go to directory 'c:\case' when it is started.

b. UNIX workstation version

1. Put .m files in the '~/matlab' sub-directory of the home directory and Matlab will search for these files automatically. '~' in this instance refers to the user's home directory.
2. Put the other files in a separate directory and set the path in '~/login' to include this directory.



Fig. 1. Initial Matlab interface window

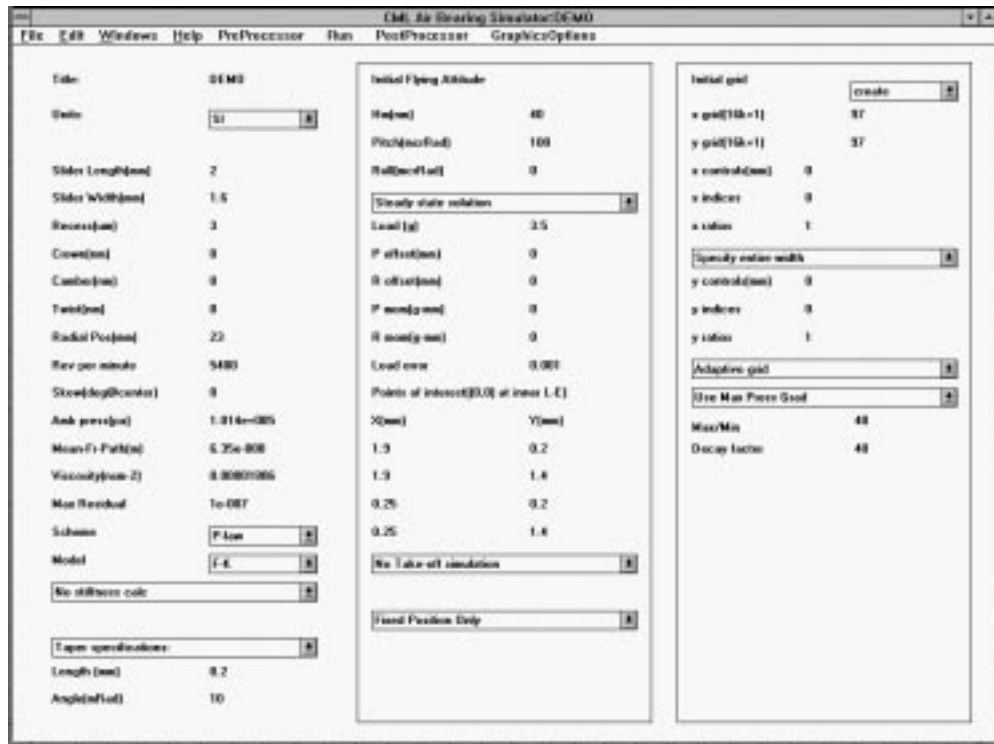


Fig. 2. Steady Definition window of the pre-processor

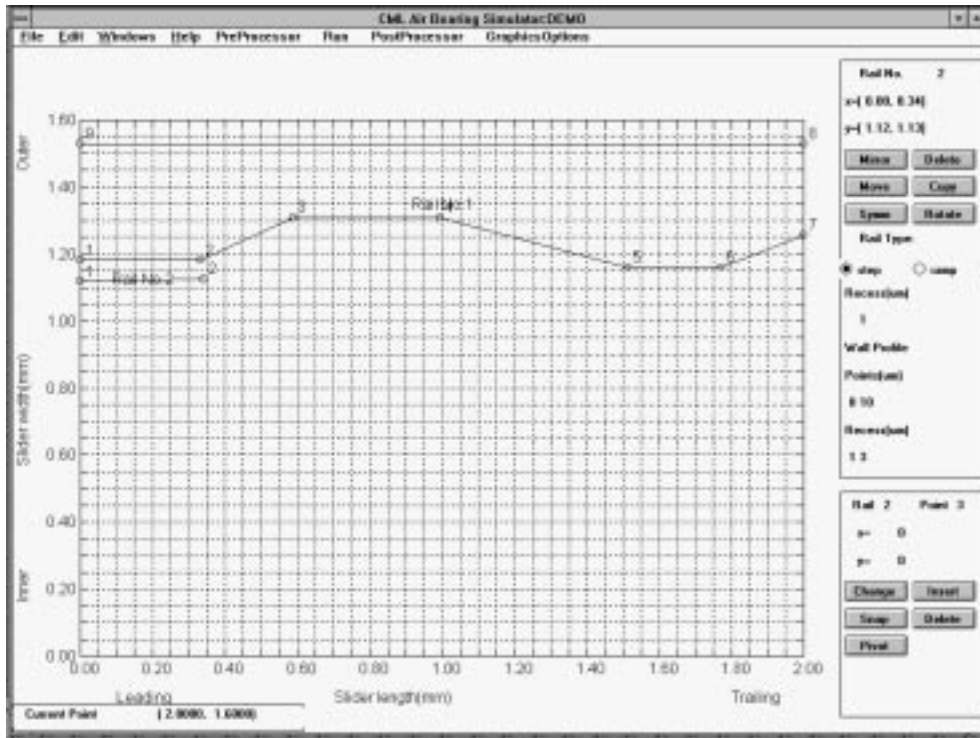


Fig. 3. Rail creation. Part

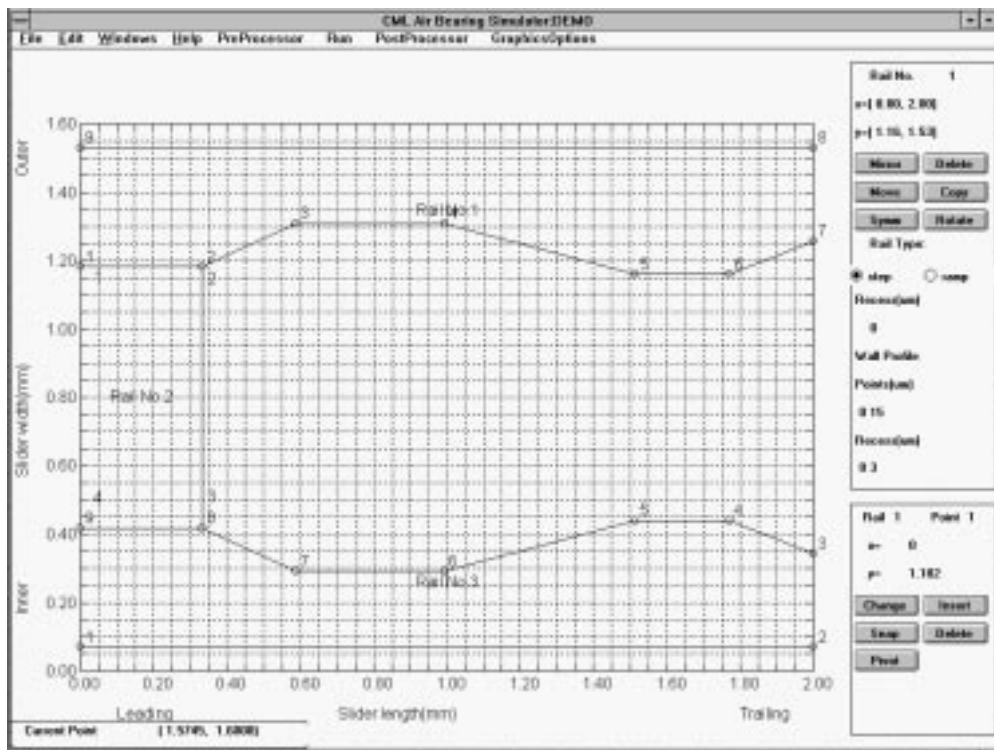


Fig. 4. Rail creation. Part 2.

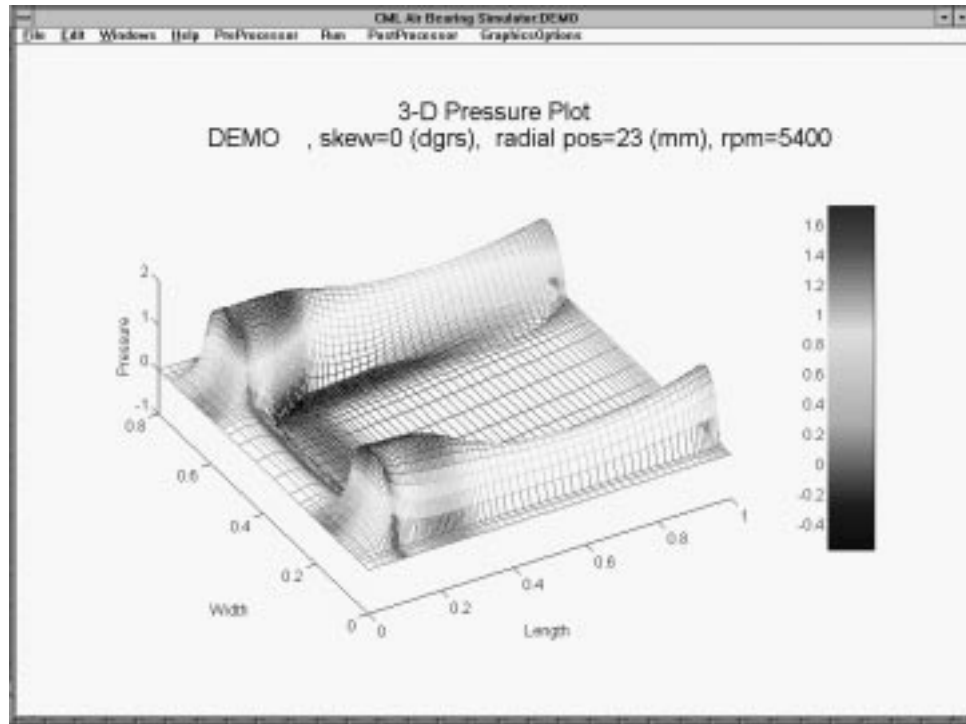


Fig. 5. 3-D pressure plot

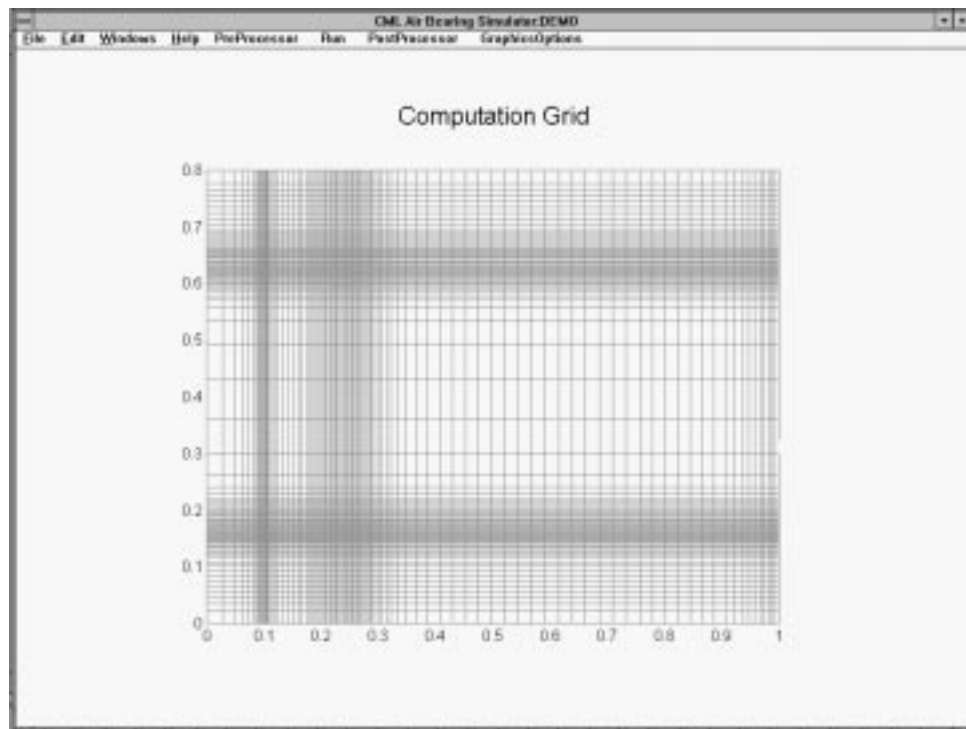


Fig. 6. Final computation grid

APPENDIX B

CML AIR BEARING DESIGN PROGRAM

USER'S MANUAL (WINDOWS VERSION)¹

1. Introduction

This manual describes the CML Air Bearing Design Program (version 4) with its new Windows interface, as well as the revised input data format. This manual is also available as a windows help file and which is included with the CML Air Bearing Design Program distribution files.

The Windows interface has been developed to replace the previous interface written in Matlab, which is a commercial mathematics and data visualization package. The Windows interface consists of a pre-processor that generates input data files readable by the solver, and a post-processor for visualization of output files generated by the solver.

The air bearing solver is written in FORTRAN 77 and has been tested under Linux, Digital UNIX, IBM AIX as well as PC/Windows. It can be easily ported to other platforms with a F77 compiler. The interface is a 16-bit Windows application that runs under both Windows 3.1 and Windows 95.

2. Installation

There are two parts in the package: the solver and the interface. They are packed in two ZIP files: quick413.zip and cmlair16.zip respectively.

¹ Co-authored by R. Grisso

2.1 Air Bearing Solver

Create a directory to hold the solver files. Unzip quick413.zip into that directory.

The files are organized into a few sub directories.

2.1.1 Files and Installation

The following is a description of the contents:

Files in the top level directory are **make** utilities: **makefile**, **make.bat**, **make**, and **sys_def**. They are only useful if the user wants to recompile the source code.

Sub directory **src/** contains the source code and includes files: **version.fi**, **size.fi**, **common.fi**, **openout.fi**, **quick.f**, **reynolds.f**, **init.f**, **grid.f**, **mult.f**, **misc.f**, **util.f**, **force.f**, **inv.f**.

Sub directory **sys/** contains the compiler specific (UNIX or PC/Watcom) **makefile** definitions: **sys_unix**, **sys_win**.

Sub directory **ibm/** contains the pre-compiled binary file **quick413** for IBM RS/6000 systems.

Sub directory **dec/** contains the pre-compiled binary file **quick413** for DEC Alpha machines.

Sub directory **pc/** contains the Windows executable **quick413.exe** generated with the Watcom compiler. To help the user re-compile the code, **make.exe** is also included. It is a PC port of the free GNU make utility, taken from the DJGPP package. The source code is generally available from GNU.

Sub directory **obj/** contains the object codes generated during compilation. It is empty at the time of distribution.

Sub directory **sample/** contains a set of sample data files: rail.dat and run.dat. They can be used to check whether the solver is properly installed. The interface should also be able to read them once installed.

For platforms where the binary file is available, the user needs only the binary file. After setting the proper path for the binary, simply go to the **sample/** directory and try to run it with the sample data files. However, the user must re-compile the code if the target platform is not directly supported. Re-compilation is also necessary when the user wishes to change some array limits. The process of re-compilation is discussed in the next section.

2.1.2 Compiling the Source Code

As described in the last section, some make utilities are provided to facilitate user compilation. Only the Watcom compiler is directly supported on the PC. Before using the Watcom compiler, append the following line to **autoexec.bat**:

```
set finclude= %finclude%;src
```

Make sure that this line appears after the original statement of "set finclude=..." (needed in setting up the Watcom compiler). Run **autoexec.bat** or reboot for the change to take effect.

If nothing in the source code needs to be altered, simply type **make** in the top distribution directory on all platforms.

On the PC, **make.bat** is executed first. It first copies **sys_win** from the **sys/** directory to **sys_def** which contains Watcom specific variable definitions for **makefile**. **Make.bat** then invokes **pc/make.exe** to make the binary.

On UNIX workstations, a shell script **make** in the current directory is invoked. It first copies **sys_unix** from the **sys/** directory to **sys_def** which contains UNIX specific variable definitions for **makefile**. The script then starts the **make** utility on the workstation to generate the binary. It assumes that **/bin/make** is the path for the **make** utility. If this is not the case, it should be changed in the shell script.

The binary file generated by **make** is in the top level directory. On UNIX machines, it is named **quick413**, while on PC it is **quick413.exe**.

In most cases, the only files the user wants to change are **size.fi** and **openout.fi**. The **size.fi** file sets the grid size, rail and wall profile array size limits. These variables are self-descriptive and can be easily modified. The second file is concerned with the problem of writing and reading many numbers in one long line. If there is an input-output problem apart from the initial reading of the **rail.dat** and **run.dat** files, check this file and make modifications. It is self-explanatory.

If the user does not often modify the code and re-compile, the object files in **obj/** generated by the compiler can be deleted to save some disk space. Just type **make clean** after compilation.

2.2 Windows Interface Installation

The installation package for the Windows interface is a zipped file **cmlair16.zip**. Unpack the file into a temporary directory with an unzip utility such as **pkunzip** from Pkware. As an example, we will assume the directory is **c:\cmltemp**, and the Windows directory is **c:\windows**.

Run the **c:\cmltemp\setup.exe** program and follow the instructions. Choose an installation directory. After installation, a program group **cmlair** and an icon should be

automatically generated in Windows. The executable of the Windows interface is **cmlair16.exe**. Before the program can be used, run **c:\cmlair\regsvr.exe c:\windows\system\vcfi16.ocx** in Windows (assuming the interface was installed in c:\cmlair).

3. Interface Guide

The interface program can be invoked by double clicking the program icon in Windows. When the interface starts, it first presents an image with the CML logo. Then a main menu bar appears at the top with a tabbed Window below it.

3.1 Menu Bar

The menu bar has two menus: *File* and *Options*.

3.1.1 File menu

There are four selections under the *File* menu: *Open*, *Save*, *Save As*, *Convert Old* and *Exit*. A dialogue box for file selection appears if *Open* is clicked. After a directory and file name are chosen, the program tries to load **rail.dat** and **run.dat** in the specified directory. The file name selected has no significance. Similarly for *Save* and *Save As*, the program saves the input files as **rail.dat** and **run.dat**. These are the only input files to the solver. This implies that the user should create a different sub directory for each case.

Convert Old lets the user to convert the prior release **quick300** input files **steady.def**, **rail.dat** and **multcase.dat** to the current form. It works just like opening and then saving files. Since there are significant changes in the input format and solver

options, the user needs to check the converted data carefully. Choosing Exit terminates the interface session.

3.1.2 Options menu

This menu contains two sub-menus: Slip Model and Solution.

Slip Model: choose from 1-order slip, 2-order slip and F-K Boltzmann models.

The F-K model is the default.

Solution: calculate pressure at Fixed Attitude or obtain steady state Fly Height iteratively. The Fixed Attitude option turns off several of the other functions. If many input frames in the tabbed Parameter window(next section) are disabled (unavailable), this option may be on!

3.2. Tabbed Parameter Window

Most of the input parameters are entered through the tabbed window shown in Figure 1. The parameters are grouped into six tabs: **General**, **Rails**, **Wall Profiles**, **Partial Contact**, **Grid** and **Run Setup**.

3.2.1 General Tab

The parameters under the **General** Tab are divided into several frames: *Slider Geometry*, *Initial Flying Attitude*, *Suspension*, *Points of Interest*, *Convergence* and *Comments*. See Figure 1.

3.2.1.1 Slider Geometry

Length, width and height : slider dimensions, default values are 2.05 mm, 1.6 mm, 0.43 mm respectively, which is standard for 50% sliders.

Crown, camber and twist: these are the second order surface topography components superimposed on each other over the whole slider. Positive crown and

camber values represent convex parabolas in the length and width directions, respectively. With a positive twist, the inner leading edge and outer trailing edge are recessed (larger spacing) while the outer leading edge and inner trailing edge are raised (smaller spacing).

Taper length and taper angle: a wedge with the given taper angle starting at taper length from the leading edge will be removed from the slider. In some cases, the taper is machined before the etching process, resulting in a recessed ramp in the frontal area. This area can be modeled by defining a ramp (see 3.2.2.3).

3.2.1.2 Initial Flying Attitude

An initial flying attitude is needed to start the calculation, no matter whether the goal is to obtain the pressure for fixed attitude or to predict the fly height. In the former case, the initial attitude is given, while in the latter case, a guessed attitude is used. The attitude has three components: TEC, pitch and roll.

TEC is the height of the trailing edge center at the zero recess plane. It is only a reference point, not a physical one. To track the fly heights at physical points on a slider, define points of interest (see 3.2.1.4). In version 3 (**quick300**), TEC must be positive. However, in certain designs, TEC can be negative at steady state if the entire trailing edge is recessed. Negative TEC is allowed in this version to allow faster convergence to steady state fly height in these situations.

For positive pitch, the spacing at the leading edge is larger than at the trailing edge, and the spacing at the outer rail is smaller than at the inner rail for positive roll. **IMPORTANT:** the roll sign convention has been changed in this version from that in the previous version in order to comply with the IDEMA standard.

3.2.1.3 *Suspension*

The parameters in this frame are needed if the fly height is sought under a given suspension load. The code searches for the steady state flying attitude using the Quasi-Newton method.

Load: suspension load.

POffset: from the center of the slider, positive value moves load point towards trailing edge.

ROffset: from the center of the slider, positive value moves load point towards outer rail.

PTorque: static pitch torque to create the static pitch.

RTorque: static roll torque to create the static roll. **Note the new sign convention for roll angle.**

3.2.1.4 *Points of Interest*

These points are used to track the fly heights of the sliders. Up to four points can be specified. The origin of the coordinate system is the inner leading edge. The input format consists of one pair of x and y (separated by a comma or space) coordinates per line.

3.2.1.5 *Convergence*

There are the two convergence criteria for the solution of the Reynolds equation and the fly height iteration.

Reynolds Equation: normalized residual for Reynolds equation. The default value of 10^{-7} is usually enough. A smaller number may be needed in some cases.

Load error: the normalized difference between suspension load and the bearing load, including torque balance. This is used in finding the steady state fly height. The default value is 10^{-3} .

3.2.1.6 Comments

This text box accepts comments about the current case.

3.2.2 Rails

Use this tab to create and modify rails (Figure 2). In this version, each edge of a rail can have a different **wall profile**. See section 3.2.3 for instructions on how to create wall profiles.

3.2.2.1 Rail Points

This text box is for entering rail shapes. On each line, type in the x, y coordinates of a rail point and the **wall profile** index (separated by space or comma) for the edge starting at this point. Use zero for the wall profile index wherever a vertical wall is needed. The origin of the rail point coordinates is at the inner leading edge.

3.2.2.2 Rail Index

The index of the current rail is displayed. Use the spin buttons on the right to switch to other rails.

3.2.2.3 Rail Type

A rail can either be a step or a ramp. A step has a uniform recess height. A ramp is a plane with arbitrary orientation. The recess heights for the first three rail points must be specified for a ramp. **IMPORTANT**: never have three collinear points for a ramp.

3.2.2.4 Base Recess

This is the recess height for all points not covered by any rail.

3.2.2.5 Miscellaneous

The command buttons *Add*, *Delete* and *Update* are used to add a rail, delete a rail and update the changes made to a rail, respectively.

The box at the lower right corner shows the number of *total rails*.

3.2.3 Wall Profiles

In Section 3.2.2, it is mentioned that for each rail edge, a **wall profile** identified by an index can be specified. These profiles are created and modified in the **Wall Profiles** tab (Figure 3).

3.2.3.1 Profile Index

The index for the current profile is shown in the box. Click on the spin buttons to select other profiles.

3.2.3.2 Profile

The *Profile* frame contains the coordinates of points defining the profile. The two coordinates are: normal distance from the nominal edge and the recess height. A negative normal distance indicates that the point is inside the rail boundary.

3.2.3.3 Miscellaneous

The box *Total Profiles* at the lower left corner indicates the total number of wall profiles defined.

The command buttons *Add*, *Delete* and *Update* are used to add a profile, delete a profile and update the changes made to a profile, respectively.

The lower right part is a graph plotting the current profile. Note that the recess heights are plotted as negative numbers.

3.2.4 Partial Contact

Partial Contact models are incorporated into the current version (Figure 4).

3.2.4.1 Model

Two models can be selected from this drop down menu: the Greenwood-Williamson or the Elastic-Plastic model. Benchmarks show that these two models produce similar results.

3.2.4.2 Surface

A few surface roughness parameters.

Asperity Density: aerial density of asperities.

STD of Asperity Height: standard deviation of asperity heights.

Radius of Curvature: mean radius of curvature for asperities.

3.2.4.3 Material

This frame contains material properties of the disk: Young's modulus, Poisson's Ratio, Yield strength and friction coefficient.

3.2.5 Grid

This tab deals with the computation grid (Figure 5).

3.2.5.1 Computation Grid

There are several grid generation options.

Initial Grid: either use the existing grid or generate a new grid using a piece-wise geometric series. If the first option is chosen, the solver will use the existing grid data files (x.dat and y.dat). The latter option is discussed in detail below.

Symmetry in Width: when checked, the grid needs only to be specified for half the width, the other half is generated using symmetry.

Adaptive Grid / Fixed Grid: In order to make better use of the available grid size, an adaptive grid method is implemented. If the adaptive grid option is on, the grid is redistributed according to pressure gradients obtained from the initial calculation. With fixed grid, only the initial grid is used. The parameters controlling the adaptive grid are described below.

3.2.5.2 Adaptive Grid

These are the parameters controlling the *adaptive grid*.

Pressure Gradient: the grid density function used to adjust the grid distribution is based on the pressure gradient obtained from the initial calculation. In order to compute the grid density in one direction, e.g., the x direction, the user can choose to use either the maximum or averaged pressure gradient along all the y locations.

Max/Min: the pressure gradient in some areas may be very small (e.g., a fully recessed region), but some minimum grid concentration may be needed the calculation. The user can specify the Max/Min pressure gradient (grid density) ratio. A smaller ratio generates a more uniform mesh.

DecayFactor: the pressure gradient may change abruptly in some regions. However, such abrupt changes in the grid distribution should be avoided to reduce discretization error. A smoothing method has been implemented so that the pressure gradient at one point not only affects the grid density at that point, but also has an exponentially decaying influence over neighboring locations. The larger the DecayFactor, the more abruptly the grid density changes.

3.2.5.3 Geometric Series

A new grid can be generated with a piecewise geometric series.

Total Grid Sizes: total number of grid lines in the x and y directions. The program uses a multi-grid method to achieve solver efficiency and requires that the grid numbers have the format $(16k + 1)$, where k is an integer.

X Control Points and Y Control Points: a set of points by which the slider length and width are cut into segments, respectively. For example, two points generate three segments. Within each segment, the successive grid size changes at a fixed ratio (geometric series).

X Grid Indices and Y Grid Indices: grid indices at X Control Points and Y Control Points, respectively.

X Grid Ratios and Y Grid Ratios: the ratios of successive grid sizes in each segment.

Note that if Symmetry in Width is checked in Section 3.2.5.1, only half of the width is needed here.

If the command button Update Grid is clicked, a graph showing the updated grid pops up (Figure 6).

3.2.6 Run Setup

This tab is used to setup the operating conditions (Figure 7).

3.2.6.1 Radial Position/Skew

Specify one Radial Position and the corresponding Skew on each line. Up to ten positions can be entered.

The order of Radial Positions should be from OD to ID, otherwise, the interface will rearrange them that way! The reason is that the solver only generates adaptive grid

at one radial position and uses it for all other cases. Since the pressure peak is usually higher at the OD, the adaptive grid should be generated there.

For positive skew, the flow goes from the outer rail towards inner rail.

IMPORTANT: the *skew* sign convention has been changed in this version from that in the previous version in order to comply with the IDEMA standard.

3.2.6.2 RPMs

Enter a series of *RPMs* separated by commas or spaces. Normally only the operating RPM is needed. Multiple *RPMs* are used for a quasi-static take-off study. The order should be from high *RPM* to low *RPM*, otherwise the interface will re-order the numbers.

3.2.6.3 Altitudes

Multiple *Altitudes* can be used to study altitude sensitivity. The order should be from low altitude to high altitude, otherwise the interface is going to re-order the numbers. If nothing is entered, then the *Air* parameters in the frame below are used. Otherwise, the *Air* frame is disabled.

3.2.6.4 Air

Specify the *ambient pressure*, *mean-free-path* and *viscosity*.

3.2.6.5 Sensitivity Increments

In order to obtain the sensitivity of slider performance with respect to certain parameters, these parameters are incremented by specified amounts. Only a positive value is needed. The program will do both negative and positive increments. Nothing is done for parameters with zero increment.

The following parameters are currently included: *Crown*, *Camber*, *Twist*, *TaperLength*, *TaperAngle*, *Load*, *PTorque*, *RTorque* and *Base Recess*. Note that *POffset* and *ROffset* are not listed, because they can be deduced from *PTorque* and *RTorque*. When *Base Recess* is changed, the wall profiles that end with the same recess height have to be adjusted accordingly. The points on the profile outside the nominal edge scale linearly with recess in the vertical direction. There are two methods to adjust the wall profile width: *proportion* or *fixed width*. *Proportion* will also scale width linearly with recess to keep the same aspect ratio, while *fixed width* only allows points to move vertically.

3.2.6.6 Miscellaneous

If *Calculate Stiffness* is checked, the program calculates and outputs a 3x3 stiffness matrix for each basic case across the disk radius. It represents the ratio of the change in bearing force components (bearing load, pitch moment and roll moment) over the change in displacement components (height, pitch and roll). Note that the sign convention has been changed for the stiffness matrix elements so that the main diagonal elements should normally be positive. A more detailed description can be found in the source code comments in **stiffness** subroutine in **misc.f**. The stiffness results are appended in the file **result.dat**. See 3.4 for a detailed description of the file **result.dat**.

Since the pressure data files are rather large, especially when there are many runs with a large grid, they are only saved when *Save Pressure* is checked. Even then, only the pressure data for basic cases across the disk radius will be saved. Three files will be saved for each radial position: **pressnum.dat**, **cprssnum.dat** and **mflownum.dat**, where

num is the index for the radial position(for example, **press01.dat** ...). Note again that the order should be from OD to ID. See 3.4 for details on output data files.

3.2.7 A Tutorial

You may have noticed that the numbers in the figures used in the above sections are actually different from the default values. This is because the figures are actually taken from a sample problem. Now it is time to put everything together and look at a complete example.

First, start up the interface by double clicking the program icon.

Click on the Options menu. Make sure *F-K Boltzmann* is selected under the *Slip Model* sub menu and *Fly Height* is selected under the *Solution* sub menu.

Select the *General* tab in the tabbed window. Enter all the parameters as shown in Figure 1.

The rails are created next. Select the *Rails* tab. In the *Rail Points* frame, enter the numbers as shown in Figure 2. The first two columns are the x and y coordinates for the rail points. The third column contains the wall profile indices for each edge. The wall profiles are defined later.

After clicking the *Add* button, the rail shape is drawn in a new window titled *Draw Rails*, as shown in Figure 3. Go back to the *Rails* tab. In the *Rail Type* frame, choose *Step* and set the *Recess Height* to 1 μm . Click on the *Update* button. Near right bottom, set the *Base Recess* to 4 μm .

Now click the *Mirror* button in the *Rails* tab, another rail is created and drawn (Figure 9). This is the mirror image of the first rail with respect to the center line. It also inherits the *Recess Height* value of the first rail.

Enter the *Rail Points* for the third rail as shown in Figure 10. Click the *Add* button. Set *Recess Height* to 0. Click *Update*. Create the fourth rail similarly (Figure 11). Figure 12 shows all four rails.

Note that all edges in the first two rails use wall profile No. 1 and all edges in the last two rails use wall profile No. 2. These wall profiles are defined next.

Select the *Wall Profiles* tab. Enter the coordinates in the *Profile* frame as shown in Figure 3. Click on the *Add* button. The new profile is now plotted in the lower right corner. Note the recess depths are negative in the plot. This is necessary in order to orient the plot properly. By convention, recess depths are represented by positive numbers in the program.

The second wall profile can be created similarly (Figure 13).

Two contact models are included in this version: *Greenwood-Williamson* and *Elastic-Plastic*. They can be selected in the *Partial Contact* tab. Enter the parameters as shown in Figure 4.

Select the *Grid* tab. Enter the grid parameters as shown in Figure 5. The adaptive grid is used with a uniform initial mesh. Click on the *Update Grid* button. A new window opens up displaying the initial mesh with the rail shapes superimposed on it (Figure 6).

Select the *Run Setup* tab. Enter the parameter as shown in Figure 7.

Since the *Altitudes* are specified explicitly, the *Air* frame is disabled.

All the parameters have been entered. The next step is to save them into the input files. Each case should have its own directory. Create a directory for the current case if you have not done so. Next click on the *File* menu and choose *Save As*. A save file

dialogue pops up. Select the correct drive and directory. The actual *File Name* entered is not important. Click on *OK* and the two files **rail.dat** and **run.dat** will be saved in the selected directory. The solver can now use these two files as input. The format of the input files is discussed in the next section.

3.3 Input Data Files

There are only two input data files in this version: **rail.dat** and **run.dat**. The first file describes the slider geometry, while the second one prescribes the test condition. There have been some changes in the input format from Version 3.

3.3.1 rail.dat

Sample **rail.dat**:

```
CML VERSION 4.0.13 RAIL.DAT
REPORT BUG TO SHA LU: shalu@cml.me.berkeley.edu
2.050E-03      1.600E-03      4.300E-04
4              2
4              1
0.000E00      5.000E-05      1
2.050E-03      5.000E-05      1
2.050E-03      4.000E-04      1
0.000E00      4.000E-04      1
1.000E-6
4              1
0.000E00      1.550E-03      1
2.050E-03      1.550E-03      1
2.050E-03      1.200E-03      1
0.000E00      1.200E-03      1
1.000E-6
4              1
0.000E00      1.500E-04      2
2.050E-03      1.500E-04      2
2.050E-03      3.500E-04      2
0.000E00      3.500E-04      2
0.000E00
4              1
0.000E00      1.500E-03      2
2.050E-03      1.500E-03      2
```

```

2.050E-03      1.300E-03      2
0.000E00      1.300E-03      2
0.000E00
4 5
0.00E+00 6.00E-06 1.20E-05 2.00E-05
1.00E-06 3.00E-06 3.60E-06 4.00E-06
-1.00E-05 -5.00E-06 0.00E+00 5.00E-06 1.00E-05
0.00E+00 1.00E-07 3.00E-07 8.50E-07 1.00E-06
2.000E-04      1.000E-02      4.000E-06
2.00E-08      1.00E-08      0.00E+00
2.025E-03 1.950E-03 2.025E-03 1.950E-03
2.500E-04 2.500E-04 1.350E-03 1.350E-03

```

The first two lines are the header. The third line contains the slider dimensions in meters: **length, width, thickness**. The fourth line indicates the **number of rails** and the **number of (different) wall profiles** used.

Next, each rail is defined in succession. The starting line for each rail describes the **number of points** and **style**. A **step** has a **style** value of 1, while a **ramp** has a **style** value of 0. The lines that follow contain the **x and y coordinates** of a rail point and the **wall profile index** for the rail edge starting at that point. Note that the **x and y coordinates** are now in meters instead of normalized, and the **wall profile indices** should be zero for a **ramp**. The final line in a rail description contains the **recess height(or three heights for a ramp)** in meters for the rail.

The line that follows the rail definitions contains **the number of wall profile points** for all wall profiles. Next, each wall profile definition occupies two lines. The first line contains the normal distances to the nominal edge for the profile points. Note the unit is now in meters. A negative value indicates that the point is inside the nominal rail boundary, while a positive value otherwise. The second line contains the recess depth in meters for each point. Note that the zero recess reference plane is the same as for all the rail recess depths, rather than the nominal recess for each rail.

The next line contains the **taper length** in meters, the **taper angle** in radians, and the **base recess** in meters. Note the units for the taper from have been changed from Version 3.

The following line gives the crown, camber and twist in meters. Note the order of camber and twist has been changed from that in Version 3.

The final two lines are the **x and y coordinates** for the points of interest. Note the unit is now meters.

3.3.2 run.dat

Sample **run.dat**:

```
CML VERSION 4.0.13 RUN.DAT
REPORT BUG TO SHA LU: shalu@cml.me.berkeley.edu
*****Solution Control*****
istiff isolv ioldg iadpt isave
1 1 0 1 1
*****Initial Attitude*****
hm(m) pitch(rad) roll(rad)
5.0000E-08 1.0000E-04 0.0000E+00
*****Runs*****
irad irpm ialt
2 2 2
radii(m)
1.5000E-02 2.3000E-02
skews(deg)
-3.0000E+00 8.0000E+00
RPMs
3.6000E+03 5.4000E+03
altitudes(m)
0.0000E+00 2.0000E+03
*****Air Parameters*****
p0(pa) al(m) vis(nsm-2)
1.0135E+05 6.3500E-08 1.8060E-05
*****Load Parameters*****
f0(kg) xf0(m) yf0(m)
3.500E-03 2.5000E-05 2.5000E-05
xfs(μNM) yfs(μNM) emax
5.0000E-01 5.0000E-01 1.0000E-03
```

```

*****Grid Control*****
nx    ny
 67   67
nsx   nsy   isymm
 1    1    0
xnt(i), i = 2, nsx

nxt(i), i = 2, nsx

dxr(i), i = 1, nsx
 1
ynt(i), i = 2, nsy

nyt(i), i = 2, nsy

dyr(i), i = 1, nsy
 1
*****Adaptive Grid*****
difmax    decay    ipmax
 40       40       0
*****Reynolds Equation*****
ischeme   imodel   akmax
 2        3        1.0000E-07
*****Partial Contact*****
icmodel   stdasp(m)   dnsasp(m-2)
 1        6.0000E-09  1.0000E+12
rdsasp(m)  eyoung(pa)  yldstr(pa)
1.0000E-08 1.0000E+10  1.0000E+12
frcoe     pratio
 0.3      0.3
*****Sensitivities*****
crowninc(m)  camberinc(m)  twistinc(m)
1.0000E-08  1.0000E-08  1.0000E-08
tlnginc(m)   tanginc(rad)   loadinc(kg)
1.0000E-05  1.0000E-03   3.0000E-04
ptrquinc(uNM) rtrquinc(uNM) recessinc(m)
5.0000E-01  5.0000E-01   5.0000E-01
iwscale
 1
*****Comments*****
" This is a test case"

```

Here are some explanations:

Solution Control:

istiff: 1 = calculate stiffness, 0 = no stiffness calculation
isolv: 1 = solve for fly height, 0 = given attitude
ioldg: 1 = use existing grid data, 0 = create new grid
iadpt: 1 = use adaptive grid, 0 = no adaptive grid
isave: 1 = save pressure and mass flow, 0 = don't save

Initial Attitude:

hm(m): nominal trailing edge height
pitch(rad): pitch, note the change in units from the previous version
roll(rad): roll

Runs:

irad: number of disk radii where the solution is sought
irpm: number of RPMs
ialt: number of altitudes, 0 = use Air Parameters
radii(m): disk radii
skews(deg): skews corresponding to each disk radii
rpms: RPMs
altitudes(m): altitudes, lowest one is the base case.

Air Parameters:

p0(pa): ambient pressure
al(m): mean free path
vis(NS/M²): viscosity

Load Parameters:

f0(kg): load

xf0(m): load point x offset, origin is at the geometric center now!
yf0(m): load point y offset
xf μ (NM): static pitch torque, note the change of unit
yf μ (NM): static roll torque
emax: convergence criterion of load error

Grid Control:

nx: total x grid number (16k+1)
ny: total y grid number (16k+1)
nsx: number of sections in length
nsy: number of sections in width
isymm: 1 = symmetry in width, 0 = specify entire width
xnt(i), i = 2, nsx: x control points in meters, no longer normalized!
nxt(i), i = 2, nsx: grid indices at x control points
dxr(i), i = 1, nsx: grid ratios for each x section
ynt(i), i = 2, nsy: y control points, use half width if **isymm = 1**
nyt(i), i = 2, nsy: grid indices at y control points
dyr(i), i = 1, nsy: grid ratios for each y section

Adaptive Grid:

difmax: ratio of max/min gradient allowed
decay: smaller value increases smoothness
ipmax: 1 = use maximum gradient, 0 = average gradient

Reynolds Equation:

ischeme: convective term scheme. No available in interface.

0 = upwind
1 = hybrid
2 = power-law; default

imodel: slip model
1 = first order slip
2 = second order slip
3 = FK; default

akmax: convergence criterion for Reynolds equation

Partial Contact:

icmodel: 0 = no contact model
1 = Greenwood-Williamson
2 = Elastic-Plastic

stdasp(m): standard deviation of asperity height

dnsasp(m⁻²): asperity density

rdsasp(m): mean radius of curvature of asperity

eyoung(pa): Young's modulus

yldstr(pa): yield strength

frcoe: friction coefficient

pratio: Poisson's ratio

Sensitivities:

Zero increment means no sensitivity is calculated for the parameter.

crowninc(m): crown increment

camberinc(m): camber increment

twistinc(m): twist increment

tlnginc(m): taper length increment

tanginc(rad): taper angle increment

loadinc(kg): load increment

ptrqinc(μ NM): pitch torque increment

rtrqinc(μ NM): roll torque increment

recessinc(m): recess increment

iwscale: used with **recessinc**

0 = stretch the profile, the normal distances are unchanged, only the depths are scaled.

1 = scale the wall profile with recess. For the part of the profile that is outside the nominal rail boundary, the normal distances will change proportionally with recess.

3.4 Output Data Files

There are three basic output files: **result.dat**, **x.dat** and **y.dat**.

The **x.dat** and **y.dat** files are one long line each containing the x grid and y grid respectively.

If *Save Pressure* (3.2.6.6) is checked, the pressure data for the basic cases across the disk radius will be saved. Three files will be saved for each radial position: **pressnum.dat**, **cprssnum.dat** and **mflownum.dat**, where *num* is the index for the radial position (for example, **press01.dat** ...). **pressnum.dat** contains the air bearing pressure matrix. The contact pressure is stored in **cprssnum.dat**. The mass flow data are written to **mflownum.dat**. The mass flow is equivalent to some stream line function. When

plotted as contours, a flow pattern is obtained. No particular physical unit is chosen for mass flow, so the absolute number has no meaning. Since the mass flow is obtained on a grid shifted by half a grid cell from the grid in **x.dat** and **y.dat**, another set of grid files **xm.dat** and **ym.dat** are also created.

3.4.1 result.dat

The following is the **result.dat** generated with the sample input file **rail.dat** and **run.dat**:

```
CML VERSION 4.0.13 RESULT.DAT
REPORT BUG TO SHA LU: shalu@cml.me.berkeley.edu
NUMBER OF DISK RADII: 2
  RADII(MM) : 23.0000 15.0000
  SKEWS(DEG) : 8.000 -3.000
NUMBER OF RPMS: 2
  RPMS : 5400.00 3600.00
NUMBER OF ALTITUDES: 2
  ALTITUDES(M): .00 2000.00
SENSITIVITY CASE IDENTIFIERS:
  CROWN : -1,+1  CAMBER: -2,+2  TWIST: -3,+3
  LOAD : -4,+4  PTORQUE: -5,+5  RTORQUE: -6,+6
  TAPER-L: -7,+7  TAPER-A: -8,+8  RECESS: -9,+9
```

```
RADIUS NO. 1  RPM  NO. 1  ALTIT. NO. 1  SENSI. NO. 0
```

```
  ERROR    NOMINAL HM(NM)  PITCH(URAD)  ROLL(URAD)
.5366E-03   74.5526    97.4190    3.5856
```

```
H(2.025, .250) H(1.950, .250) H(2.025,1.350) H(1.950,1.350)
  72.7230    77.2811    68.7788    73.3369
```

```
MIN. HEIGHT = 67.87 (NM) AT (2.032, 1.310)
POSITIVE FORCE(G): 3.7561
NEGATIVE FORCE(G): -.2579
CONTACT FORCE(G): .0000
```

X-SHEAR FORCE(G): .0937
Y-SHEAR FORCE(G): -.0187

STIFFNESS MATRIX

LOAD(G) .415202E-01 .262170E-01 -.175599E-03
P-TORQUE(uN-M) .102611E+00 .203075E+00 -.518799E-02
R-TORQUE(uN-M) .213759E-01 .917882E-02 .127288E+00
HEIGHT(NM) PITCH(uRAD) ROLL(uRAD)

RADIUS NO. 2 RPM NO. 1 ALTIT. NO. 1 SENSI. NO. 0

ERROR NOMINAL HM(NM) PITCH(URAD) ROLL(URAD)
.7169E-03 55.0433 69.3858 -7.1412

H(2.025, .250) H(1.950, .250) H(2.025,1.350) H(1.950,1.350)
46.6132 49.0687 54.4685 56.9241

MIN. HEIGHT = 45.65 (NM) AT (2.032, .337)
POSITIVE FORCE(G): 3.5199
NEGATIVE FORCE(G): -.0220
CONTACT FORCE(G): .0000
X-SHEAR FORCE(G): .0704
Y-SHEAR FORCE(G): .0045

STIFFNESS MATRIX

LOAD(G) .670632E-01 .434416E-01 -.107704E-02
P-TORQUE(uN-M) .202550E+00 .322121E+00 -.143572E-01
R-TORQUE(uN-M) -.200479E-01 -.191136E-01 .196978E+00
HEIGHT(NM) PITCH(uRAD) ROLL(uRAD)

RADIUS NO. 1 RPM NO. 1 ALTIT. NO. 1 SENSI. NO.-1

ERROR NOMINAL HM(NM) PITCH(URAD) ROLL(URAD)
.7353E-03 71.5524 92.0714 3.3781

H(2.025, .250) H(1.950, .250) H(2.025,1.350) H(1.950,1.350)
69.9568 75.4880 66.2409 71.7721

MIN. HEIGHT = 65.23 (NM) AT (2.032, 1.310)
POSITIVE FORCE(G): 3.7604

NEGATIVE FORCE(G): -.2617
CONTACT FORCE(G): .0000
X-SHEAR FORCE(G): .0938
Y-SHEAR FORCE(G): -.0187

RADIUS NO. 2 RPM NO. 1 ALTIT. NO. 1 SENSI. NO.-1

ERROR	NOMINAL HM(NM)	PITCH(URAD)	ROLL(URAD)
.6309E-03	51.6885	64.0435	-7.1190

H(2.025, .250)	H(1.950, .250)	H(2.025,1.350)	H(1.950,1.350)
43.6188	47.0479	51.4497	54.8788

MIN. HEIGHT = 42.56 (NM) AT (2.032, .337)
POSITIVE FORCE(G): 3.5214
NEGATIVE FORCE(G): -.0232
CONTACT FORCE(G): .0000
X-SHEAR FORCE(G): .0707
Y-SHEAR FORCE(G): .0045

RADIUS NO. 1 RPM NO. 1 ALTIT. NO. 1 SENSI. NO. 1

ERROR	NOMINAL HM(NM)	PITCH(URAD)	ROLL(URAD)
.5292E-03	77.5928	102.9010	3.5210

H(2.025, .250)	H(1.950, .250)	H(2.025,1.350)	H(1.950,1.350)
75.3829	78.9779	71.5097	75.1048

MIN. HEIGHT = 70.69 (NM) AT (2.032, 1.310)
POSITIVE FORCE(G): 3.7536
NEGATIVE FORCE(G): -.2541
CONTACT FORCE(G): .0000
X-SHEAR FORCE(G): .0935
Y-SHEAR FORCE(G): -.0187

RADIUS NO. 2 RPM NO. 1 ALTIT. NO. 1 SENSI. NO. 1

ERROR NOMINAL HM(NM) PITCH(URAD) ROLL(URAD)
.9494E-03 58.5525 74.7487 -7.0545

H(2.025, .250) H(1.950, .250) H(2.025,1.350) H(1.950,1.350)
49.8223 51.3059 57.5822 59.0658

MIN. HEIGHT = 48.94 (NM) AT (2.032, .337)

POSITIVE FORCE(G): 3.5189
NEGATIVE FORCE(G): -.0209
CONTACT FORCE(G): .0000
X-SHEAR FORCE(G): .0702
Y-SHEAR FORCE(G): .0045

.....
(sensitivity calculation for other parameters omitted)

RADIUS NO. 1 RPM NO. 1 ALTIT. NO. 1 SENSI. NO.-9

ERROR NOMINAL HM(NM) PITCH(URAD) ROLL(URAD)
.1610E-03 77.5524 99.1200 7.6194

H(2.025, .250) H(1.950, .250) H(2.025,1.350) H(1.950,1.350)
77.9839 82.6696 69.6026 74.2883

MIN. HEIGHT = 68.84 (NM) AT (2.032, 1.310)

POSITIVE FORCE(G): 3.7636
NEGATIVE FORCE(G): -.2633
CONTACT FORCE(G): .0000
X-SHEAR FORCE(G): .0938
Y-SHEAR FORCE(G): -.0190

RADIUS NO. 2 RPM NO. 1 ALTIT. NO. 1 SENSI. NO.-9

ERROR NOMINAL HM(NM) PITCH(URAD) ROLL(URAD)
.5924E-03 55.8462 70.4524 -7.9408

H(2.025, .250) H(1.950, .250) H(2.025,1.350) H(1.950,1.350)
47.0029 49.5385 55.7377 58.2733

MIN. HEIGHT = 46.10 (NM) AT (2.032, .337)
POSITIVE FORCE(G): 3.5192
NEGATIVE FORCE(G): -.0209
CONTACT FORCE(G): .0000
X-SHEAR FORCE(G): .0708
Y-SHEAR FORCE(G): .0046

RADIUS NO. 1 RPM NO. 1 ALTIT. NO. 1 SENSI. NO. 9

ERROR	NOMINAL HM(NM)	PITCH(URAD)	ROLL(URAD)
.8994E-03	72.7215	96.3402	.8082

H(2.025, .250)	H(1.950, .250)	H(2.025,1.350)	H(1.950,1.350)
69.3374	73.8145	68.4484	72.9256

MIN. HEIGHT = 67.43 (NM) AT (2.032, 1.310)
POSITIVE FORCE(G): 3.7499
NEGATIVE FORCE(G): -.2516
CONTACT FORCE(G): .0000
X-SHEAR FORCE(G): .0934
Y-SHEAR FORCE(G): -.0185

RADIUS NO. 2 RPM NO. 1 ALTIT. NO. 1 SENSI. NO. 9

ERROR	NOMINAL HM(NM)	PITCH(URAD)	ROLL(URAD)
.8626E-03	54.5658	68.7130	-6.5175

H(2.025, .250)	H(1.950, .250)	H(2.025,1.350)	H(1.950,1.350)
46.4618	48.8670	53.6310	56.0362

MIN. HEIGHT = 45.45 (NM) AT (2.032, .337)
POSITIVE FORCE(G): 3.5210
NEGATIVE FORCE(G): -.0227
CONTACT FORCE(G): .0000
X-SHEAR FORCE(G): .0701
Y-SHEAR FORCE(G): .0044

RADIUS NO. 1 RPM NO. 1 ALTIT. NO. 2 SENSI. NO. 0

ERROR	NOMINAL HM(NM)	PITCH(URAD)	ROLL(URAD)
.4530E-03	65.8378	97.5521	3.7931

H(2.025, .250)	H(1.950, .250)	H(2.025,1.350)	H(1.950,1.350)
64.1257	68.6938	59.9533	64.5213

MIN. HEIGHT = 59.05 (NM) AT (2.032, 1.310)
POSITIVE FORCE(G): 3.7341
NEGATIVE FORCE(G): -.2346
CONTACT FORCE(G): .0000
X-SHEAR FORCE(G): .0879
Y-SHEAR FORCE(G): -.0176

RADIUS NO. 2 RPM NO. 1 ALTIT. NO. 2 SENSI. NO. 0

ERROR	NOMINAL HM(NM)	PITCH(URAD)	ROLL(URAD)
.8447E-03	49.6137	67.5718	-7.0691

H(2.025, .250)	H(1.950, .250)	H(2.025,1.350)	H(1.950,1.350)
41.1779	43.4974	48.9539	51.2734

MIN. HEIGHT = 40.22 (NM) AT (2.032, .337)
POSITIVE FORCE(G): 3.5169
NEGATIVE FORCE(G): -.0194
CONTACT FORCE(G): .0000
X-SHEAR FORCE(G): .0650
Y-SHEAR FORCE(G): .0042

RADIUS NO. 1 RPM NO. 2 ALTIT. NO. 1 SENSI. NO. 0

ERROR	NOMINAL HM(NM)	PITCH(URAD)	ROLL(URAD)
.6483E-03	44.8390	68.4265	-.4451

H(2.025, .250)	H(1.950, .250)	H(2.025,1.350)	H(1.950,1.350)
40.0677	42.4513	40.5573	42.9409

MIN. HEIGHT = 38.53 (NM) AT (2.032, .337)
POSITIVE FORCE(G): 3.7053

NEGATIVE FORCE(G): -.2067
CONTACT FORCE(G): .0000
X-SHEAR FORCE(G): .0668
Y-SHEAR FORCE(G): -.0133

RADIUS NO. 2 RPM NO. 2 ALTIT. NO. 1 SENSI. NO. 0

ERROR	NOMINAL	HM(NM)	PITCH(URAD)	ROLL(URAD)
.7443E-03	35.7047	45.7431	-3.9767	

H(2.025, .250)	H(1.950, .250)	H(2.025,1.350)	H(1.950,1.350)
28.4240	29.1063	32.7984	33.4807

MIN. HEIGHT = 27.35 (NM) AT (2.032, .337)
POSITIVE FORCE(G): 3.5181
NEGATIVE FORCE(G): -.0203
CONTACT FORCE(G): .0000
X-SHEAR FORCE(G): .0484
Y-SHEAR FORCE(G): .0031

The top section contains general information on different runs: disk radii, RPMs and altitudes. It also gives the identifiers for different tolerance parameters. The positive and negative signs represent positive and negative increment, respectively. The rest of file contains the results for each case.

The cases are ordered using the following rules. A set of cases with different disk radii going from OD to ID is called a **disk traversal**. The **basic disk traversal** is run first, which has the highest RPM and lowest altitude.

Next the sensitivities with respect to the tolerances are calculated using the basic disk traversal as reference. Only those parameters whose increment is not zero are actually used. The parameters are ordered by the identifiers given in the top section. For

each parameter, a disk traversal is performed first with a negative increment of the parameter and then with a positive increment.

Disk traversals are performed next in the order of increasing altitudes.

Finally, disk traversals are performed in the order of decreasing RPMs.

The first line for each case is the case identifier consisting of the radius, RPM, altitude and sensitivity indices. Next the normalized error for load, the fly height at the nominal trailing edge, pitch and roll are given. The fly heights at the four points of interest follow. The minimum fly height point and its location are saved. Various integral forces are summarized next: positive force, negative force, contact force, shear force in x direction and shear force in y direction. If the stiffness calculation is enabled, the stiffness matrices are also saved for the basic disk traversal defined above.

3.4.2. Postprocessing

Included in this version is a post processor for visualization of output files. Users may also visualize output data using Matlab.

3.4.2.1 CML Post Processor (Quick Post)

If the preprocessor interface was properly installed, it should allow direct access to the CML Post Processor (Quick Post) via the *Post Processing* menu item from the *File* menu in the preprocessor interface.

3.4.2.1.1 Files

To open a document for post processing, choose “File : Open” from the main menu. Then, from the file dialog box, choose a file from the directory in which the input and output files from Quick are located. The actual file that you choose is irrelevant. Only the directory matters. This directory is called the “document directory”. (*Note:*

Quick uses the current working directory as the initial directory for the Quick Post. In other words, if you invoke Quick Post from Quick, you will not have to open any files manually).

When Quick Post opens a document, it checks for the existence of the following Quick input files **rail.dat** and **run.dat**. If these files are not in the document directory, Quick Post will issue an error message and will not be able to continue. If you receive this error message, check to make sure these files are contained in the document directory.

Quick Post also checks for Quick output files. It first reads **run.dat** to find the number and type of output files that should exist, and then checks for the existence of those files in the document directory. No warnings are issued if these files are not found.

If **rail.dat** and **run.dat** are properly formatted, Quick Post will display an initial default window of the slider rail geometry (See 3.4.2.1.2 Rails).

3.4.2.1.2 Rails

To view the rail geometry of the current slider, choose *Rails* from the *Post* menu. This is a view of the slider rail geometry. Note: Neither wall angles nor taper are displayed. This view is simply a reference for the user. There are no viewing options.

3.4.2.1.3 3-d Air Pressure

To view the air bearing pressure for the current simulation, choose *Pressure Profile* from the *Post* menu. This is a 3-d plot of the air pressure data generated by Quick. Quick Post uses X.DAT and Y.DAT as axis data and PRESS*.DAT as the pressure data. There are several viewing options:

- Dynamic Rotation

The figure can be dynamically rotated using mouse-trackball style control. Simply double-click the left mouse button and hold down the button after the second click.

By moving the mouse, the figure can be rotated as if the mouse was a trackball.

- **Menu Options**

Click the right mouse button to get a popup menu with various viewing preferences.

These include background color, zoom, Z-scale, and rotation.

3.4.2.1.4 3-d Contact Pressure

To view the contact pressure for the current simulation, choose *Contact Profile* from the *Post* menu. This is a 3-d plot of the contact pressure data generated by Quick.

Quick Post uses X.DAT and Y.DAT as axis data and CPRSS*.DAT as the pressure data.

The contact pressure plot viewing options are the same as those for the air pressure plot (see 3.4.2.1.3 3-d Air Pressure).

3.4.2.1.5 Mass Flow Contour

To view the mass flow contour plot for the current simulation, choose *Mass Flow* from the *Post* menu. This is a contour plot of the mass flow data generated by Quick.

Quick Post uses XM.DAT and YM.DAT as axis data and MFLOW*.DAT as the mass flow data.

- **Menu Options**

Click the right mouse button to get a popup menu with various viewing preferences.

The only viewing options currently included are line width and number of contour lines.

3.4.2.2 Matlab Post Processing

Although postprocessing capabilities are included in the current Windows interface, users can also can plot the data using Matlab (this is useful for users running the code on UNIX machines for which there is no bundled post-processing). For example, to see a 3-D pressure plot, using **press01.dat**, use these Matlab commands:

```
load x.dat  
load y.dat  
load press01.dat  
mesh(x, y, press01)
```

To see the averaged mass flow in **mflow01.dat**, issue the following Matlab commands:

```
load xm.dat  
load ym.dat  
load mflow01.dat  
contour(xm, ym, mflow01, 100)
```

Matlab will plot 100 equal-increment stream lines for mass flow. However, no rail shapes are superimposed on the plot.

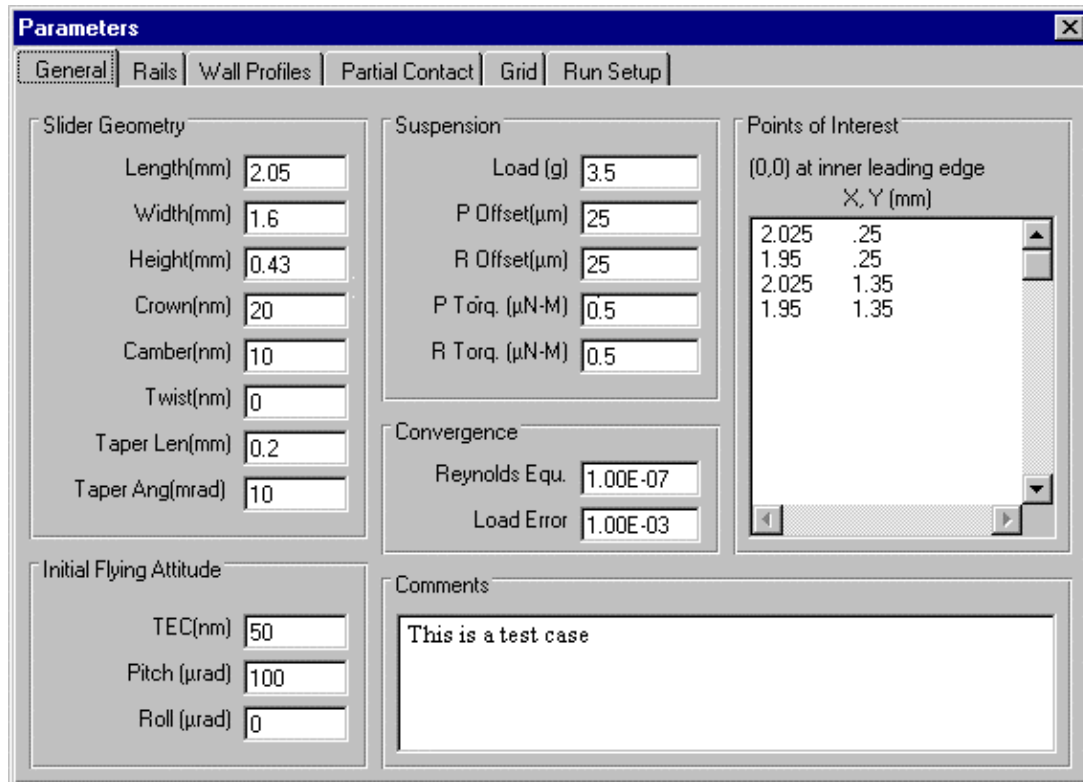


Fig.1

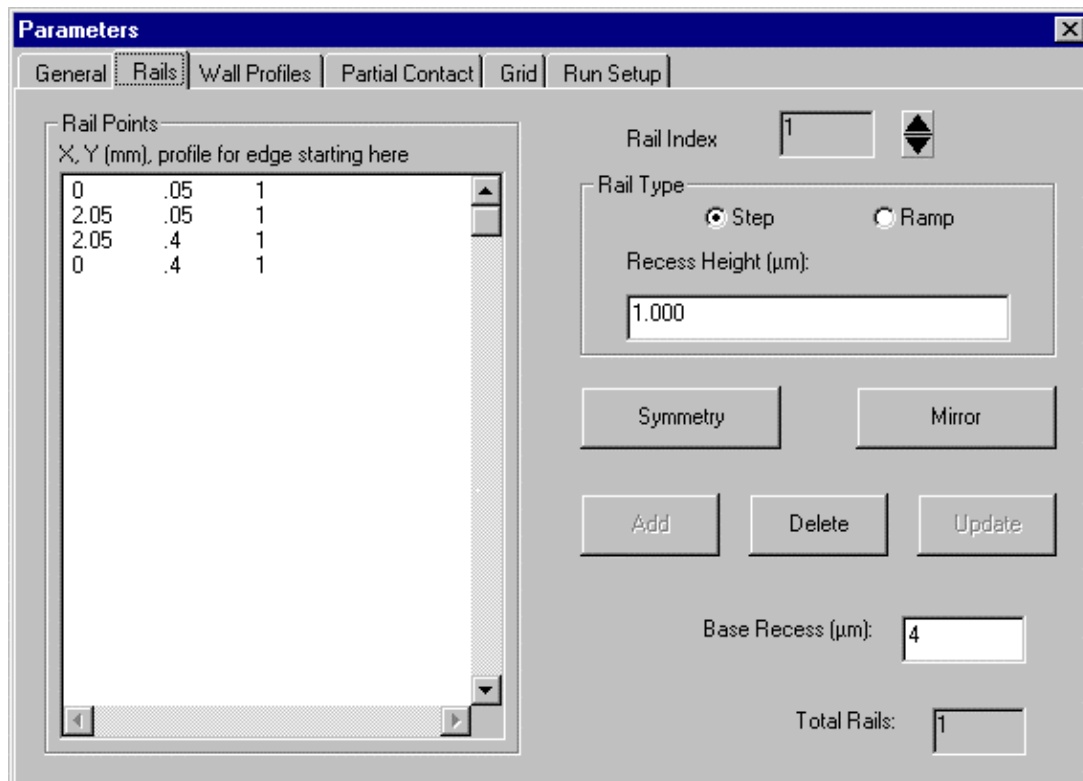


Fig. 2

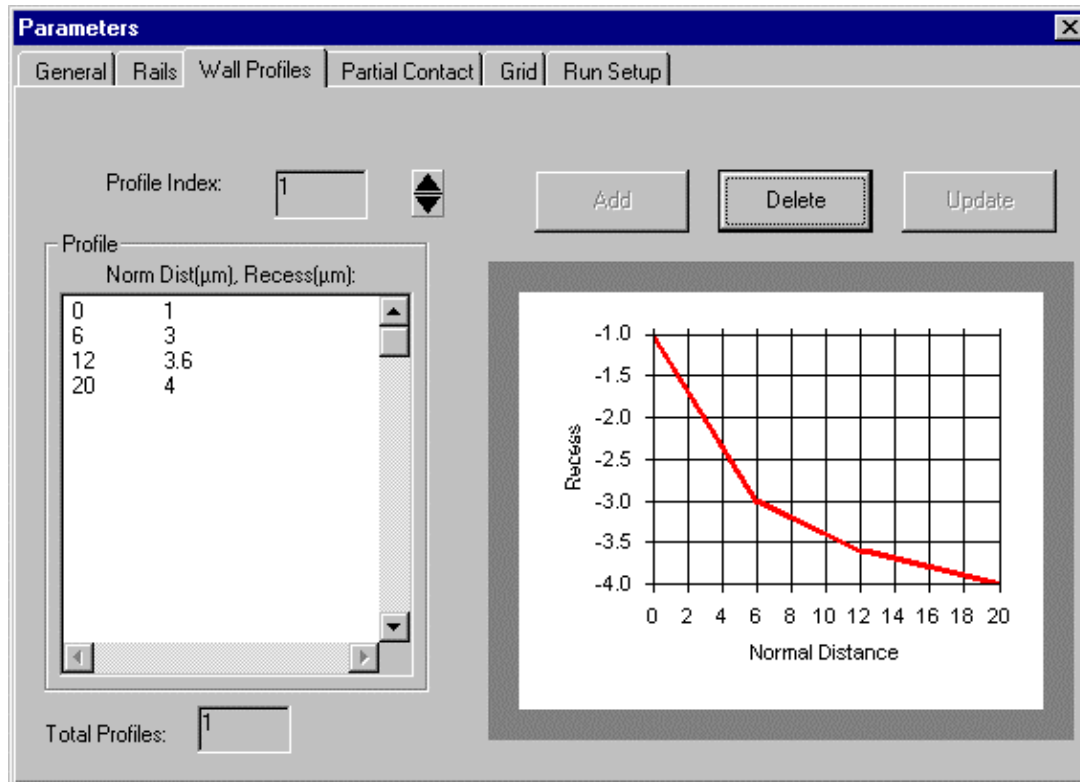


Fig. 3

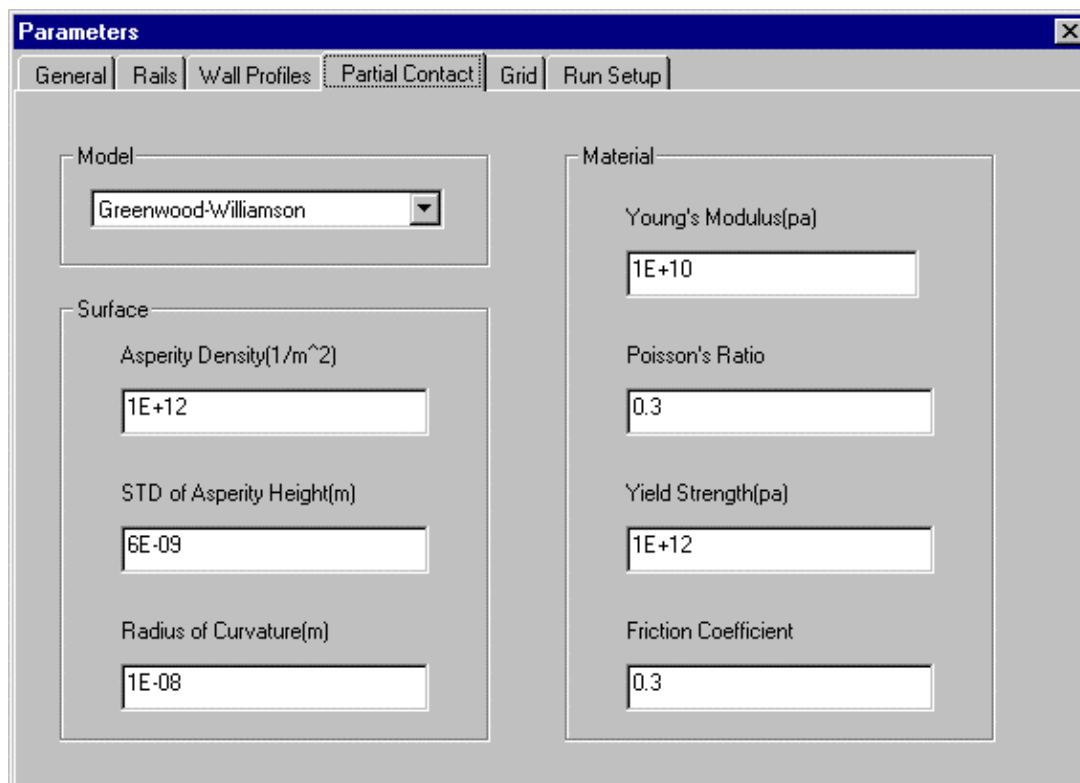


Fig. 4

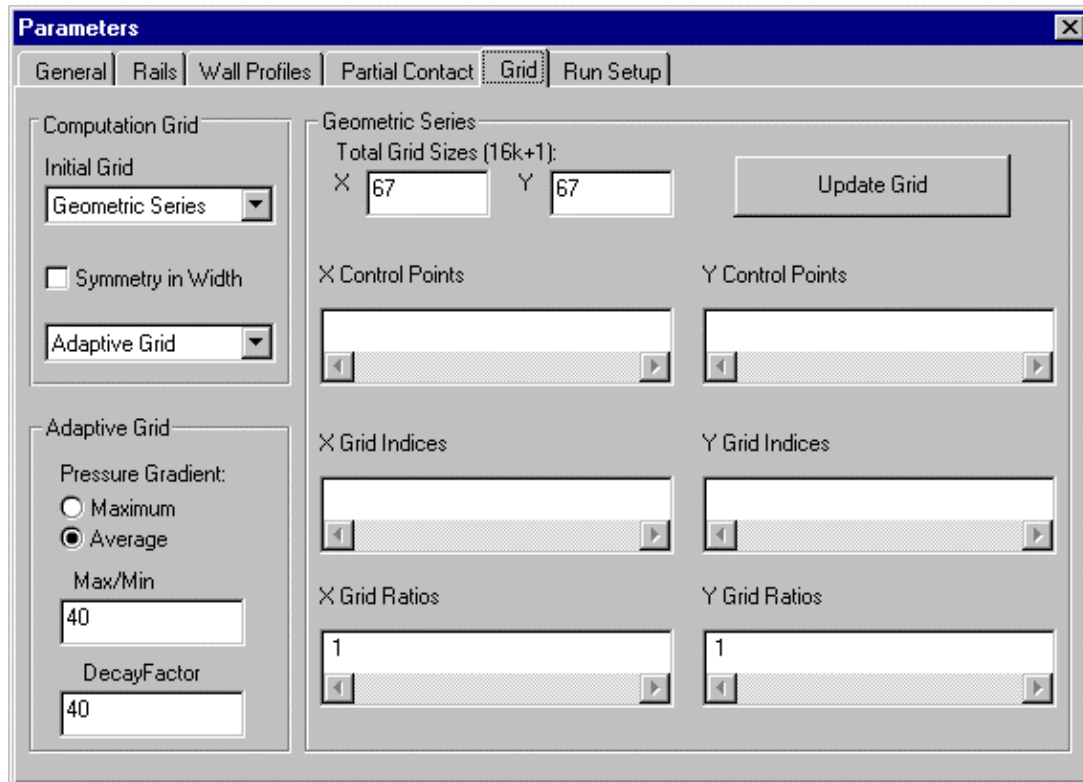


Fig. 5

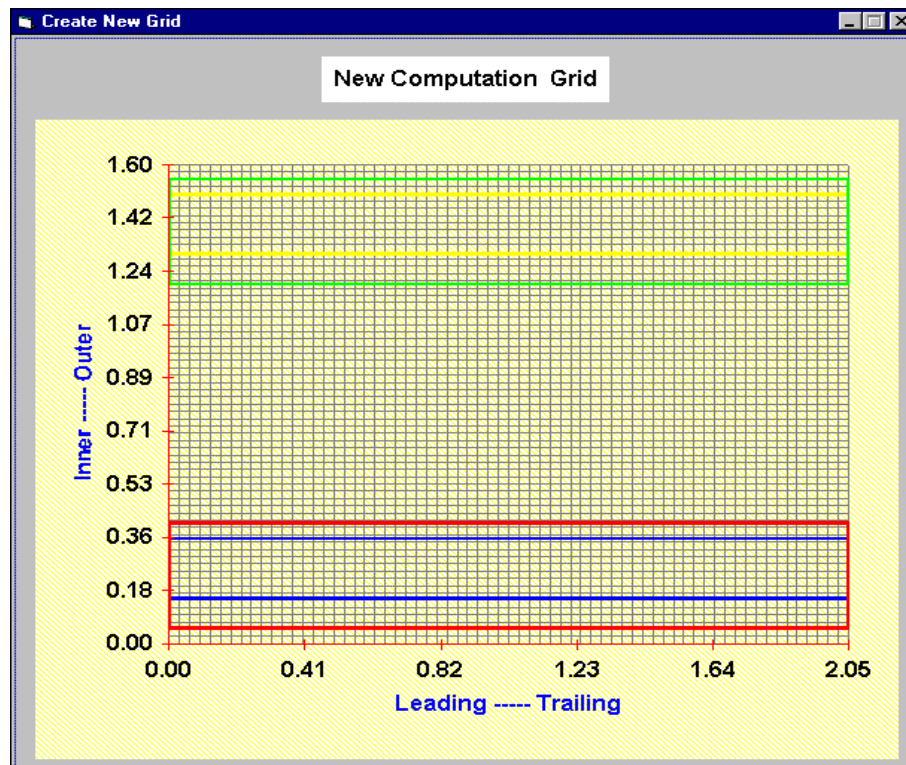


Fig. 6

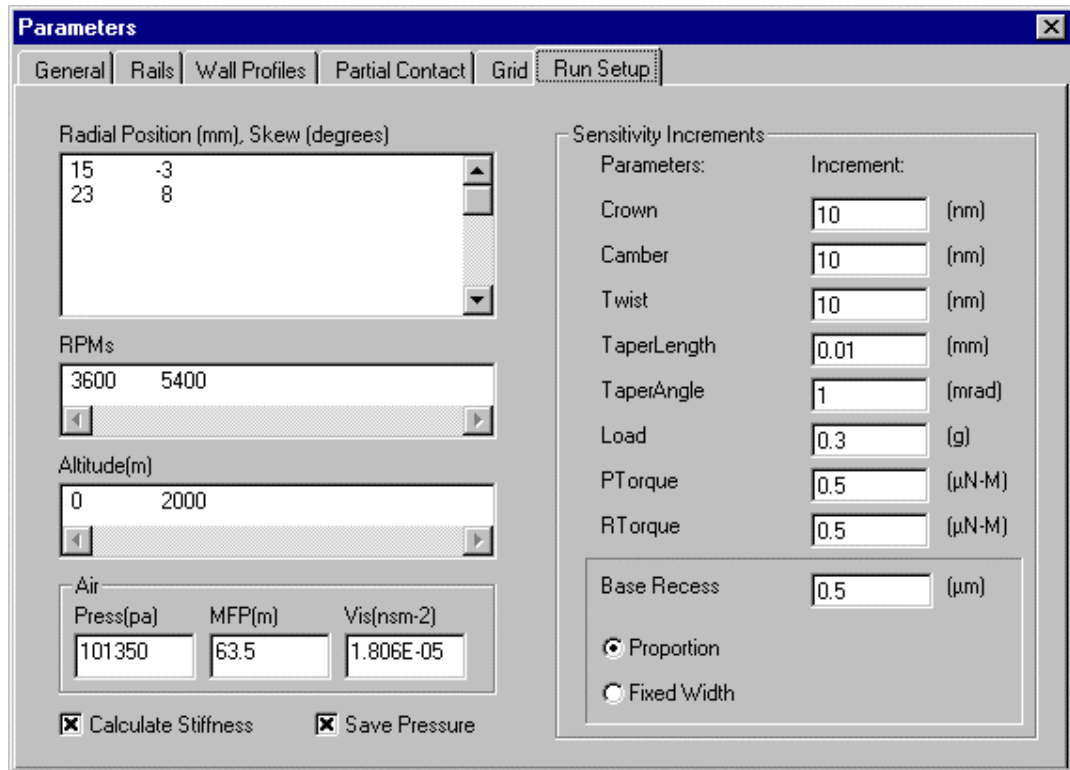


Fig. 7

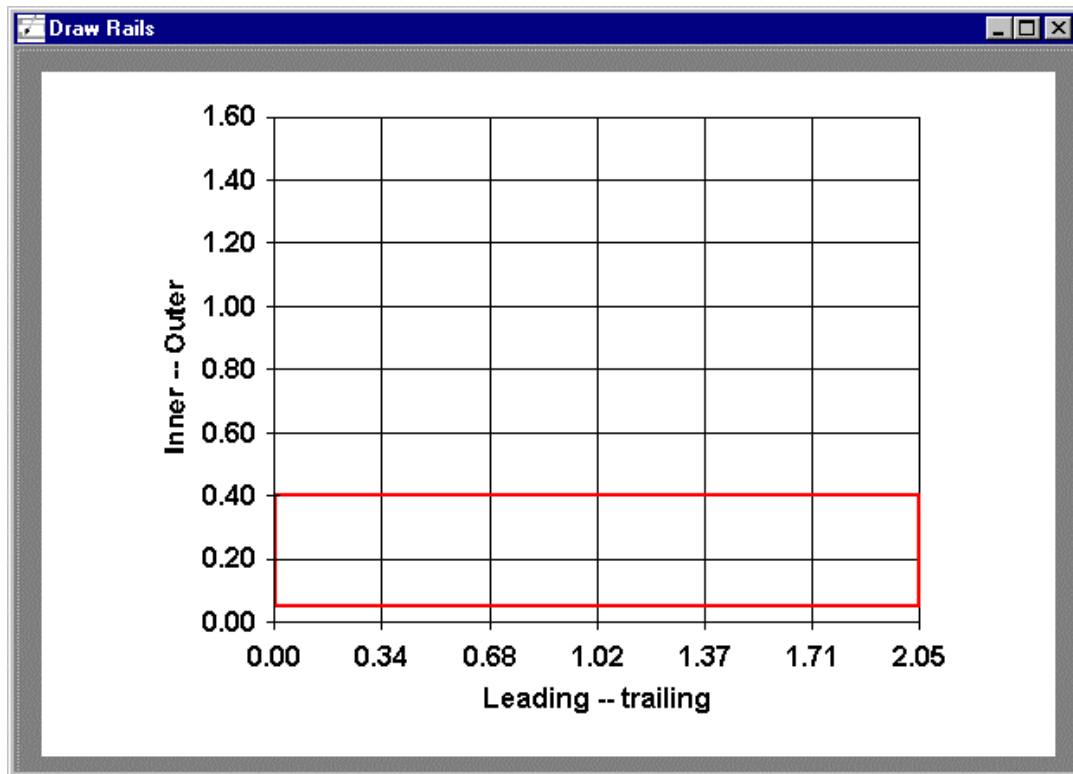


Fig. 8

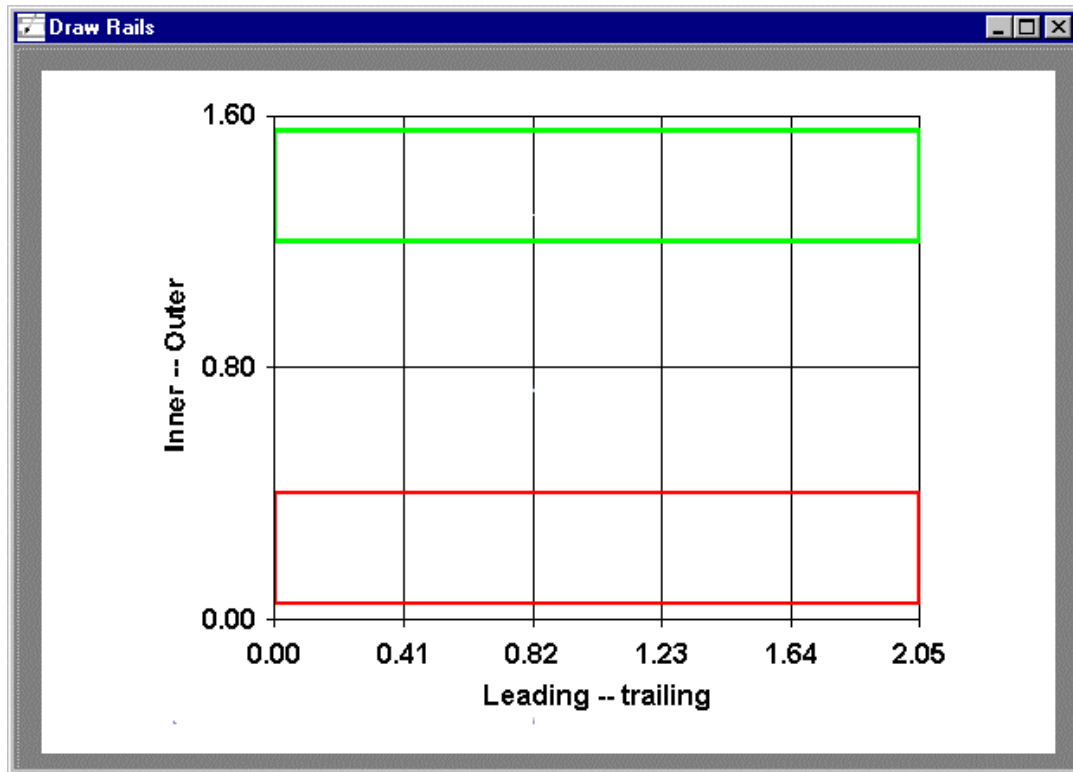


Fig. 9

The 'Parameters' window shows the configuration for drawing rails. The 'Rail Points' table is as follows:

X (mm)	Y (mm)	Profile
0	.15	2
2.05	.15	2
2.05	.35	2
0	.35	2

Other parameters include: Rail Index: 3; Rail Type: Step (selected); Recess Height (µm): 0.000; Base Recess (µm): 4; Total Rails: 3.

Fig. 10

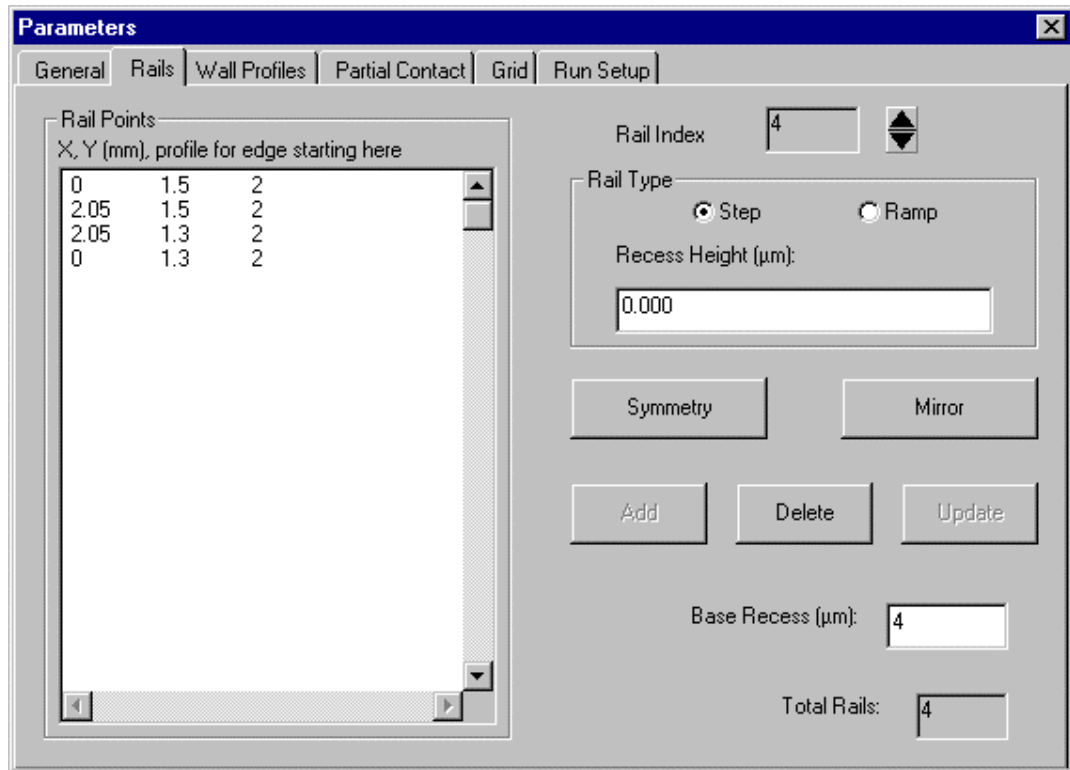


Fig. 11

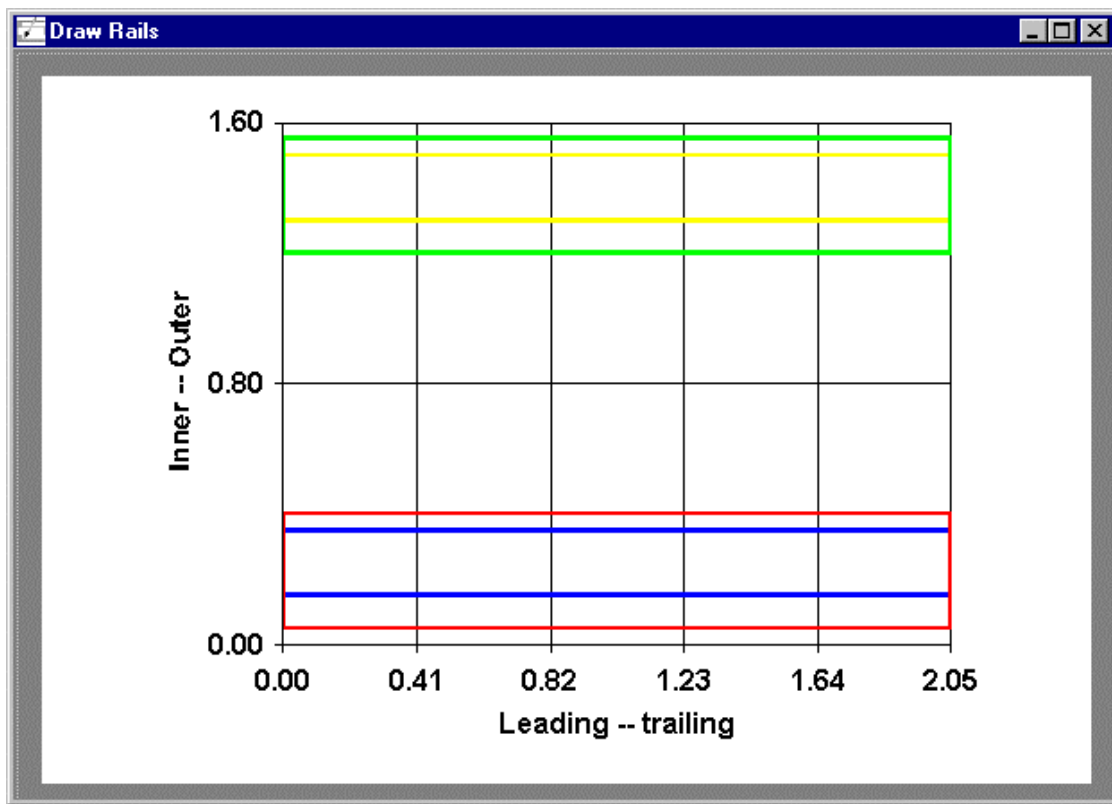


Fig. 12

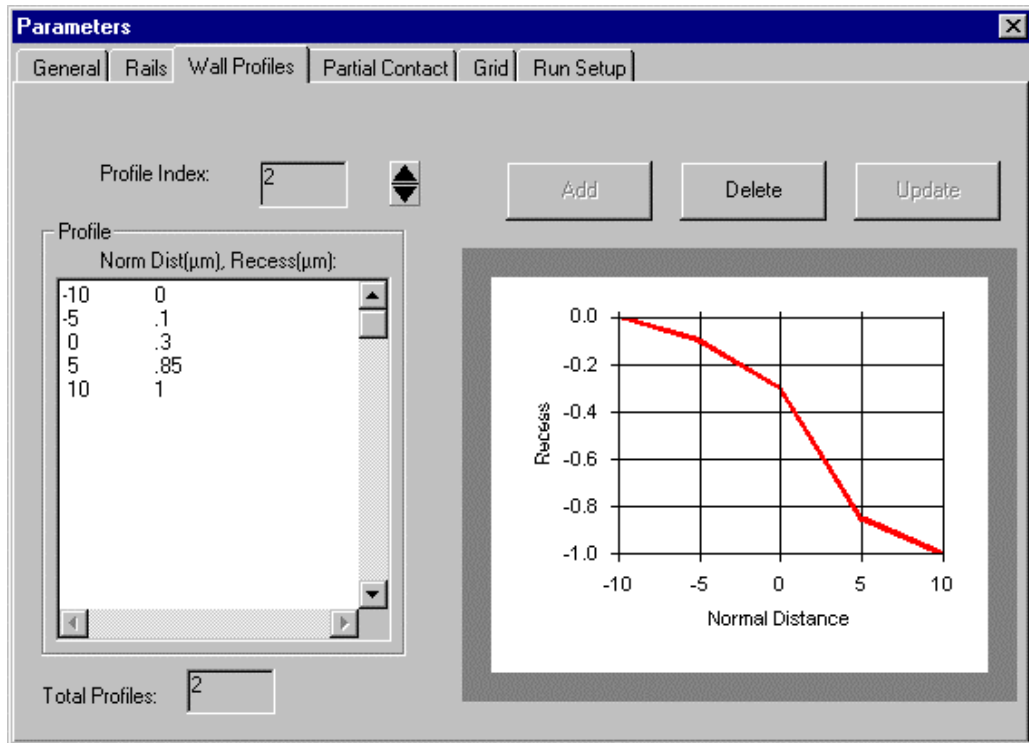


Fig. 13